מכון ויצמן למדע

WEIZMANN INSTITUTE OF SCIENCE

עבודת גמר (תזה) לתואר

דוקטור לפילוסופיה

מוגשת למועצה המדעית של
מכון ויצמן למדע
רחובות, ישראל

מאת

גיל יוסף

Thesis for the degree

Doctor of Philosophy

Submitted to the Scientific Council of the
Weizmann Institute of Science
Rehovot, Israel

By

Gil Yosef

השפעת ייעור באזורים סמי ארידים על האקלים

The climate effect of large-scale afforestation in semi-arid regions

מנחה:פרופ׳ דן יקיר

בשיתוף פרופ׳ רוני אבישר
(אוני׳ מיאמי, ארה״ב)

Advisor: Prof. Dan Yakir

Co-mentored by Prof.
Roni Avissar (Miami Uni)

טבת תשע״ו

December 2015

This work has been conducted under the supervision of

Prof. Dan Yakir

Department of Earth and Planetary Sciences
Weizmann Institute of Science
Rehovot, Israel

And

Prof. Roni Avissar

Rosenstiel School of Marine & Atmospheric Science
University of Miami
Miami, USA

Acknowledgments

I would like to thank my research advisers Prof. Dan Yakir and Prof, Roni Avissar for giving me the opportunity and full supports to work on this unique research. Thanks to their help, guidance and support I was enabled to explore investigate and find many interesting and new paths. Thank you.

I wish to thanks Dr. Robert L. Walko for his interest in the work, long and deep conversation, and advising me with scientific knowledge for improvements of my work and for extensively supporting me with technical issues.

I would also like to thank Dr. David Medvigy with whom I had the benefit to learn from and collaborate and for hosting me in his lab during the initial step of this study. The members of Dan's group with whom I have worked: Dr. Eyal Rotenberg, Yakir Preisler, Shani rohatyn, Efrat Ramati ; Fulin Yang, Rafat Qabaga, Dr Uri Dicken, Dr. David Asaf, and Dr. Tamir klein which have been research collaborators and good friends. Special thanks go to Dr. Fyodor Tatarinov, with whom I had many fruitful discussions and help on technical issues.

A warm appreciation is given to my whole family, especially to my wife Irit who was always a comfort zone for me in hard times during the PhD and always had time to hear about my work and its progress, and our little baby May, my parents, my late father Moshe and my mom Yudit who were continuously encouraging and supporting along the way.

Declaration

This Thesis summarizes my own research.

Dr. Robert L. Walko and Dr. David Medvigy have contributed to the setting and operating the global circulation model OLAM and have contributed to the discussion of the results.

Dr. Eyal Rotenberg, a research associate in our group, has contributed to set the parametrization of the new vegetation type based on Yatir forest.

Dr. Fyodor Tatarinov, a research associate in the group, has contributed in technical issues related to evaluate model simulation with observations.

All simulations using the OLAM model, model evaluation and analysis of the data, were perform by me.

All other work presented in this Thesis is also my own

Gil Yosef
Rehovot, December 2015.

Table of Contents

1. List of abbreviation

Abbreviation	Definition
AEJ	African Easterly Jet
AFFO	Afforested scenario
AUSEJ	Australian Easterly Jet
AWJ	Monsoon Westerlies – (MW), which called also Africa Westerly Jet
CERES	Cloud and the Earth Radiation Energy System
CLS	Characteristic Length Scale
CON	Control scenario
CRU	Climatic Research Unit
ENSO	El Nino-Southern Oscillation
ET	Evapotranspiration
EC	Expansion Coefficient
IAS	Indonesian- Australian Sea
I-ASM	Indonesian- Australian Summer Monsoon
ITCZ	Inter Tropical Convergence Zones
JAS	Jul-Sep
JFM	Jan-Mar
JJAS	Jun-Sep
MCA	Maximum Covariance Analysis
MFC	Moisture Flux Convergence
MSE	Moist Static Energy
N-Aust	North Australia
OLAM	Ocean-Land-Atmosphere-Model
Omega	Vertical motion
PCA	Principal Component analysis
PFT	Plant Function Type
RAMS	Regional Atmospheric Modeling System
RRTMG	Rapid Radiative Transfer Model Global version
S	Sahel
SAM	Semi-Arid Monsoon
SCF	Square Covariance Fraction
SHL	Sahara Heat Low
SST	Sea-Surface-Temperature
STJ	Sub Tropical Jet
SVD	Singular Value Decomposition

TEJ	Tropical Easterly Jet
TRMM	Tropical Rainfall Measuring Mission Project
Var	Fraction of the variance
WAM	West Africa Monsoon
WR	Water Recycle

2. Abstract

Semi arid regions are transition areas between the desert and temperate climates, and are sensitive to climate change. Several semi-arid regions, such as the Sahel and North Australia, are under the influence of monsoon regimes, low-level jets, and mesoscale convective activity, which influence on the amount of annual precipitation. In these regions the summer solar heating leads to migration of the equatorial trough and the tropical convergence zones (ITCZ), leading to monsoon rains in some parts of the regions and to a meridional surface temperature gradient that generates low-level easterly jet. This jet acts as a barrier to the penetration of moisture into other parts of semi arid areas. These processes are strongly influenced by the surface energy budget, which, in turn, is highly sensitive to land cover and vegetation type. This study, tested the hypothesis that large-scale afforestation in these semi-arid regions can result in changes in local and regional atmospheric circulation and, in turn, in the amount of precipitation. We tested our hypothesis using the Ocean-Land-Atmosphere Model (OLAM), General Circulation Model (GCM) by simulating the effects of the afforestation in the Sahel and North Australia. We carried out 17 years simulations (1996-2012) with 200 km horizontal grid scale and 6 years simulations (2000-2006) with 50 km horizontal grid scale of afforestation scenarios. The afforested areas parameterization (Sahel 2.6 E6 km^2 and North Australia 2.1 E6 km^2) was based on the extensive data from a 15 years study of the semi-arid Yatir forest in Israel. The regional effect of the afforestation focused on the summer rainy season (Sahel: Jul-Sep., and N-Aust: Jan-Mar). The results showed that changing land cover from shrubland to forest increases root depth, soil water content and ET that leads to lower surface temperature over the forest and decrease in the meridional temperature gradient. Changes in temperature gradient leads to increased precipitation due to weakening and displacement of the low level thermal wind, responsible for the generation the easterly jet. Ocean contribution to the precipitation over the Sahel has positive feedback due to higher sea-surface-temperature (SST) of the Northern hemisphere during summertime. This study results demonstrates the significant effect of Monsoon rains and oceans presence nearby large-scale afforestation in semi-arid regions, on the local and regional hydrological cycle. This effect is expressed in an increase of latent heat leading to land surface cooling and to positive feedbacks that evolve in precipitation increase in the afforested areas surroundings.

תקציר

האקלים הצחיח למחצה, מאפיין אזור מעבר בין אזור האקלים הצחיח לבין אזור אקלימי גשום יותר. משטר הגשמים באזור הצחיח למחצה אינו יציב: חלוקת המשקעים בעונת הגשמים אינה אחידה, ויש הבדל גדול בכמות המשקעים לאורך השנים. חוסר יציבות זה מסכן כ 15% מכלל אוכלוסית העולם כתוצאה מפגיעה בחקלאות ועירעור מקורות המזון. באזורים צחיחים למחצה כגון הסאהל וצפון אוסטרליה כמות המשקעים השנתית מושפעת ממשטר גשמי המונסון, זרמי רוח חזקים (זרם סילון) בגובה נמוך, ופעילות קונבקטיבית. באזורים אלו חימום השמש בקיץ גורם להצפנה של אזורי התכנסות הלחות באיזורים הטרופיים שמוביל להזזת גשמי המונסון לאיזורים הצחיחים. כמו כן חימום השמש יוצר גרדיינט תרמלי אורכי בין האזורים הארידים החמים לאזורים הטרופים הקרירים. כתוצאה מכך, מתפתח בגובה נמוך זרם סילון המהווה מחסום לחדירה של לחות לחלקים הפנימיים ביבשת. תהליכים אלו מושפעים מאוד ממאזן האנרגיה בקרקע, אשר רגיש מאוד לסוג כיסוי קרקע וצמחייה. מחקר זה בדק את ההשערה כי ייעור בקנה מידה גדול באזורים צחיחים למחצה עלול לגרום לשינויים מקומיים בסיקרקולציה האטמוספרית והשפעה ישירה על זרם הסילון בשכבות הנמוכות של האטמוספרה ובכך לעליה בכמות המשקעים. באמצעות מודל גלובלי אקלימי (OLAM), נבדקה ההשפעה של ייעור בקנה מידה גדול באזור הסאהל וצפון אוסטרליה, לצורך כך בוצעו סימולציות לאורך 17 שנים 2012-1996 ברזולוצית גריד גלובלי של 200 ק״מ וסימולציות לאורך 6 שנים 2006-2000 ברזולוציה גריד של 50 ק״מ מעל אזור הייעור. לצורך פרמטריזציה של היער, נעשה שימוש במדידות ארוכות טווח שנערכות ביער יתיר - יער נטוע הממוקם באזור ספר המדבר בארץ ישראל עם כמות משקעים שנתית מתחת ל 300 מ״מ, יער שהתאים עצמו לסביבה ומתקיים מעל 50 שנה. השפעה האזורית של הייעור התמקדה בעונת גשמי המונסון (סאהל: יולי-ספטמבר, צפון אוסטרליה: ינואר-מרץ). תוצאות המחקר הראו כי שינוי בכיסוי הקרקע מכיסוי צמחייה דליל (שיחים) ליער, גרם להגדלת חספוס פני השטח ובכך להגדלת המוליכות האוירודינמית, ובנוסף גרם להעמקת השורשים, אשר הגדילה את יכולת הוצאת המים מהקרקע. שינויים אלו יצרו התחזקות בתהליך האוופוטרנספירציה שהוביל לקירור פני השטח. ירידת הטמפרטורה הפחיתה את גרדיינט התרמלי האורכי, שינוי אשר הוביל להגדלת המשקעים עקב היחלשותו של זרם הסילון. בדיקה של תרומת אגני האוקינוסים השונים לשינוי המשקעים באזור הסאהל בעקבות הייעור, הראתה כי התחממות אגני האוקיינוס האטלנטי והפסיפי גרמו להפחתה קטנה במשקעים בהשוואה להעצמת המשקעים באופן קבוע בחודשי הקיץ, כתוצאה מהתחממות בטמפרטורת הים בחצי הכדור הצפוני. תוצאות מחקר זה מראות כי לגשמי המונסון ונוכחות אוקיינוסים בסמוך לייעור נרחב באיזורים צחיחים למחצה קיימת השפעה משמעותית על מחזור המים. השפעה זו מתבטאת בעליה בשטף החום הכמוס מהקרקע שיוביל להתקררות פני השטח ולהיזון חיובי אשר יוביל לעליית משקעים באיזור הייעור ובסביבתו המורחבת.

3. Introduction

3.1. Ecosystem effects on climate

The Earth's climate is a complex system determined by physical (climate system and land surface), chemical (greenhouse gases, chemically reactive atmospheric gases, and aerosols) and biological (evapo-transpiration, carbon cycle) processes occurring in the ocean and on land. The terrestrial ecosystems are an integral component of the Earth's global climate system, with significant influence on the global water, energy and carbon cycle *(Foley et al., 2000; Cowling et al., 2009).* They provide both positive and negative climate feedbacks, due to biogeophysical and biogeochemical process *(Claussen et al., 2001).*

The biogeochemical effects relate to processes influencing atmospheric CO2 concentration due to changes in biomass, or in the rate of physiological processes (e.g. photosynthesis, respiration). It is well established that the level of atmospheric CO2, which directly influences the Earth's temperature, depends critically on the rates of carbon uptake by ocean and land, which are, in turn, sensitive to climate *(IPCC, 2007).*

Geophysical effects refer to processes that directly influence the Earth surface radiation budget (not through greenhouse gases). A major factor in this respect is land cover in general (including snow, bare land) and vegetation type in particular through their effect on albedo *(Claussen et al., 2001).* Studies, which focus over larger spatial scales and using GCMs models, take into account geophysical feedbacks of vegetation to surface boundary layer. It is done primarily through four mechanisms: First, the reflectivity of the Earth's surface (albedo). Second is the amount of moisture returned to atmosphere via evapotranspiration form the vegetation and soil. Third is roughness element- the extent to which vegetation initiates convection by exchanging momentum with the atmosphere, and fourth is the partitioning of incoming solar radiation into latent heat and sensible heat fluxes *(Cowling et al., 2009).*

Linking all the components: The terrestrial change can modify the global climate through both geophysical and biogeochemical process, which influence each other through vegetation *(Bonan, 2008).* Fig. 1 (based on *Field et al., 2007*) schematically illustrates the link between all the components, describing how terrestrial ecosystem feedbacks, the climate

under certain scenarios.

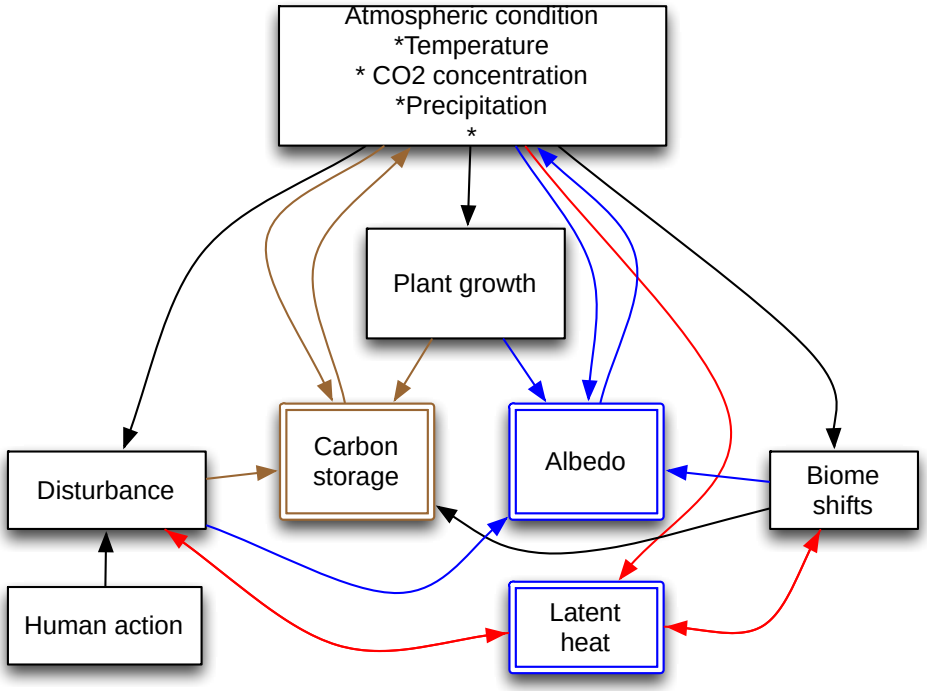

Figure 1. Schematic diagram of the terrestrial atmospheric mechanisms influenced by biogeochemical (carbon storage -green arrows) and geophysical effects (albedo -blue arrows; in addition to latent heat flux -red arrows), and a set of driving processes (plant growth, biome shifts, and disturbance -black arrows), which are mostly the same for CO2 and the physical process.

Processes based on these links can be found for example in clouds and vegetation, which influence radiative feedbacks *(Koster et al., 2006).* The latter can affect or be effected by the net exchange of carbon between the land and atmosphere through plant grow and disturbance *(Houghton, 2003; DeFries et al., 2002).* Also changes over land that modify the evaporative cooling can cause large changes in the surface temperature, both locally and regionally. These changes function as a feedback to the precipitation regime. *Li and Fu (2004)* showed that the rainy season is strongly dependent on transpiration by vegetation during the dry season, thus suggesting that deforestation over the Amazon leads to a longer dry season.
In context to land-cover change, geophysical and biogeochemical feedbacks can offset each other, regionally or locally. This can be as a result of large-scale dynamical feedbacks, which are influenced by small-scale processes over time and area *(IPCC, 2007).*

3.2. The importance of the Semi Arid region

Semi-arid zones cover 15.2% of the land surface, and habitable by 14.4% of world population. They are characterized by low erratic rainfall of up to 700 mm per annum, periodic droughts and different associations of vegetative cover and soils. The interannual rainfall varies from 20-50% around the long-term mean of up to 700 mm (*Goodin and Northington, 1985).* These climatic zones face ecological constraints, which set limits to nomadic pastoralism and settled agriculture. Such constraints include irregular rainfall regime, heavy showers rainfall that is lost to run-off, high rate of potential evapotranspiration influencing the soil moisture that reflects on the crop yields *(Salih and Ahmed, 1993).* Native people of these areas have lived within these constraints for centuries, but according to the Climate Model Intercomparison Project (CMIP), future predictions of the semi-arid environment, predict a higher heat stress (3-5^{0}C in the Sahel, 0-1^{0}C in N-Aust at 2050) and reduction in precipitation (25%), which could reduce vegetation cover and further enhance the surface warming *(IPCC RC8.5; Chadwick et al., 2013, 2015).* Reduction in vegetation cover will enhance soil degradation through salinization waterlogging and wind erosion. This in turn will result in desertification process and can alert future food security.

3.3. The impact of land-cover changes on climate in the semi-arid regions

Afforestation is a process whose influence on arid areas has been studied amply. The chronology that brought about the thought of afforestation as a climate-engineering approach began with the proposal of ideas to boost the humidity volume so that it will promote the precipitation at desert border areas. Already at the early twentieth century, it was proposed to transfer water from the Congo River into the Chad Basin that was supposed to supply irrigation to part of the Sahara area (*Flohn et al, 1974*). The river shifting would cause an increase of humidity in the air and as a result of the evaporation process the precipitation would grow. This proposal was not accepted, as this process was expected to raise precipitation volume only by 10%. Similar schemes, suggesting developing large inland bodies of water in and around Sahara, were also questioned because the deficiency of rain during the sub-Saharan summer is caused mainly by a dynamical factor that is large-scale

subsidence in the region. Other scheme was suggested to use forest in West Africa to prevent the sand from wandering southwards and reducing the dry northeast winds (*Stebbing, 1938*).

Local studies, on changing land use to vegetation and its potential influence on local climate found that, humidity accumulation capability increase and albedo decreases. This in turn, changes the soil surface energy balance that can influence the planetary boundary layer (PBL) formation process and the development of convective streams and clouds (*Anthes, 1984; Avissar and Pielke, 1989; De Ridder and Galle, 1998; Otterman et al., 1990; Segal et al., 1995; Xie and Shukla, 1994*). Increase in cloudiness leads to an increase in rainfall and soil moisture, and in semi-arid regions this change, from dry to moist soils leads to self maintains and also can increase the vegetation (*Otterman et al., 1990; Zeng et al., 1999, 2003*). *Rotenberg and Yakir (2010)* presents study on radiation budget of plant forest in a semi-arid area, shows that lack of available water, cause higher sensible and lower latent heat flux, which in results decreasing the surface temperature.

In this study we focused on the effects of large scale afforestation in the monsoon rain season over the Sahel and N-Aust regions on the local to regional precipitation and surface temperature, using more realistic sustainable simulation using Yatir PFT's than the previous studies of planting Evergreen Broadleaf tree (tropical trees) over the desert.

3.4. Climatological features of Sahel summer monsoon

The Sahel region is a semi-arid expanse of grassland, shrubs, and small trees lying south of the Sahara desert to the humidity savanna at roughly 10^0 North. Mean annual rainfall in the Sahel is between 100 to 200 mm in the north close to the desert, and 500 to 600 mm at its southern limit. Throughout the region rainfall is generally limited to the boreal summer months, with maximum rainfall occurring in August. Within the region there is a strong east-west uniformity of climate and vegetation conditions, due to the strong north south gradient of precipitation (Fig. 2). Contrasts appear across the region, in year-to-year variability, especially in the eastern area of the Sudan and Ethiopia, were complex topography overrides the large pattern. The Sahel's climate condition is tied with the West Africa monsoon, a large-scale circulation characterized by reversal in direction of winds in the lower levels of the atmosphere from the Atlantic Ocean transporting moisture into land.

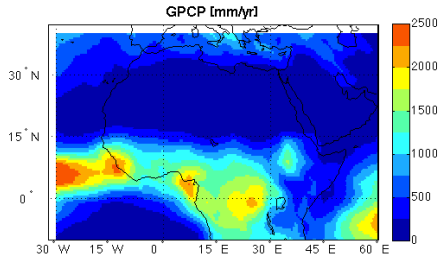

Figure 2. Average annual rainfall between the years 2003 – 2005, based on GPCP dataset.

This rainfall is associated with the ITCZ, which is marked by convergence of the warm northeasterly Harmattan winds that originate in the Sahara and the humidity southwesterly monsoon winds from the Atlantic Ocean. ITCZ's seasonal migration of north and south with respect to the sun represents the seasonal migration of the tropical rains. Because of the Coriolis force due to earth's rotation, air in the monsoon currents moves in curved paths, and causes winds to change its direction as they cross the equator. At the boreal summer when ITCZ move northern, the southeasterly winds change direction and penetrate deeper to inland, bring more cold humidity air (Fig. 3).

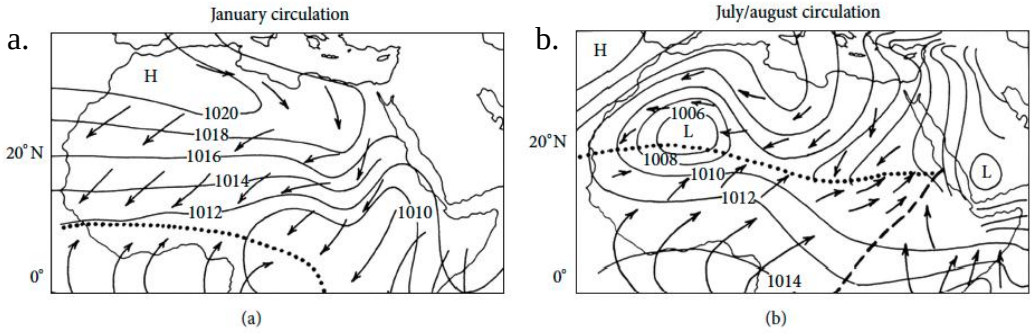

Figure 3. Schematic diagram of surface wind (arrows) and pressure (mb) over Africa at the peak of dry season a. and wet season b. *(Nicholson, 2012).*

Wind features associated with the monsoon: within the atmospheric circulation pattern, the main features associated with the West Africa monsoon (Fig .4) are the upper-level TEJ, the mid-level AEJ, and the low-level equatorial MW, which called also Africa Westerly Jet (AWJ) associated with the southwest monsoon flow.

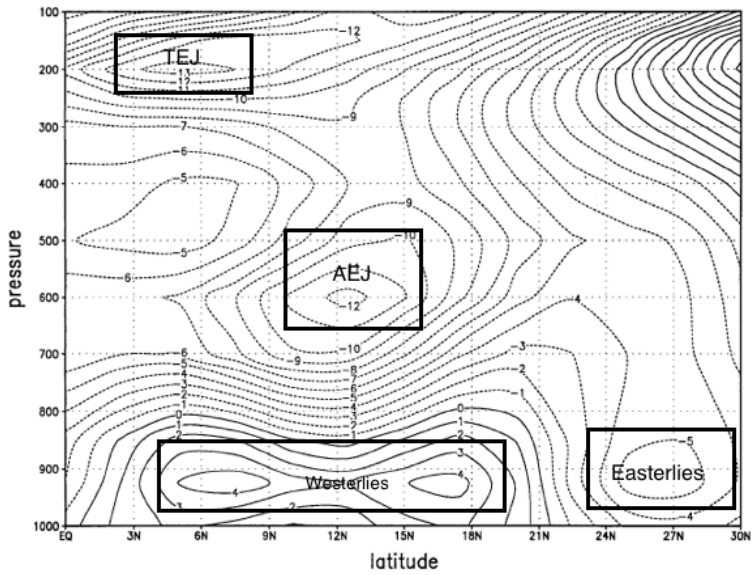

Figure 4. Latitude-height cross-section of the zonal wind at 0^0 longitude from NCEP July climatology. Contour interval is 1 m s^{-1} *(Cook, 1999).*

- AEJ - a mid-tropospheric (600-700 mb) core of strong zonal winds, travel from east to West Africa. The jet forms as a result of positive meridional surface temperature gradient over West Africa, with higher surface temperature over the Sahara and cooler, moisture air near the coast.
- Near the surface, warmer temperature over the Sahara create the SHL and dry convective circulation near the surface, at mid troposphere the descending branch flow of Hadley cell creates the Saharan high, which deflected to the right due to Coriolis force, creating the AEJ, which is thermally induced by the contrast between the hot Sahara and the cool air from the Atlantic Ocean *(Thorncorft and Blackburn, 1999).* With maximum strong shear in August due to maximum meridional surface temperature gradient.
- TEJ - During the peak monsoon boundary layer process become the dominant control. The TEJ is developed at about 200 mb level. At the monsoon season West Africa, the meridional component get curved, this creates a region of strong divergence around 200 mb, which appears to play a role in the development of the rain belt over West Africa *(Nicholson, 2009).*
- AWJ - is a low level westerly jet over the Atlantic at the level 850 mb. It appears as a near surface wind around 10^0 N and lies in the region where the trade winds convergence.

West AWJ get to its maximum values at the summer, were the maximum pressure gradient is appear, with lower pressure over Sahara and higher pressure over the ocean at the surface level. The importance of the west AWJ is by transporting moisture from the ocean to inland to 8^0 N – 11^0 N, although the transport does not extend into the Sahel there is strong correlation between the speed of this jet and western Sahel rainfall *(Cook, 1999).*

3.5. Climatological features of Australian summer monsoon

The Australian summer monsoon referred as the wet season in N-Aust. The literature relates the Australian's monsoon developments, to the thermal forcing between land-sea contrasts during the highest sun insolation, starting from late December until April. In the traditional view, the landmass heat up, leading to a reversal of the lower tropospheric temperature gradient between the land and ocean. A thermally gradient develops a meridional circulation *(Hung and Yanai, 2004),* leading to low-level north-westerlies (Fig. 5a, from Hung and Yanai, 2004), which transports moisture into North Australia's inland (refer as I-ASM) and expand the monsoon poleward over arid northern Australia (Fig. 5b).

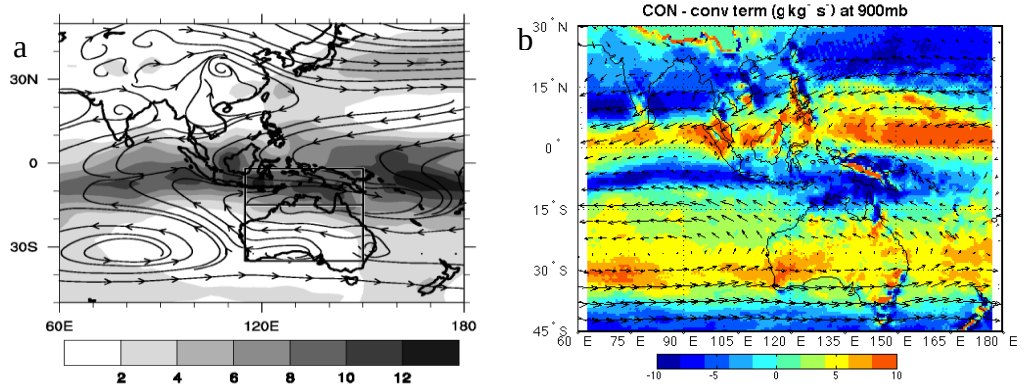

Figure 5. a. European Center for Medium-Range Weather Forecast reanalysis 850 hPa streamlines and precipitation rate (mm day^{-1}) from the Climate Prediction Center Merged Analysis of Precipitation, average over December-February 1979-93. The northern and southern rectangular boxes show the northern Australia Sea and Australian continent regions, respectively. b. CON-0.5d, Average of Moisture Flux Convergence (MFC), over Australia in JFM (2003-2005), convergence/divergence terms represent as positive/negative, were calculated for the 900 mb, arrows represents wind, Units in [10^{-3} g kg^{-1} s^{-1}].

The transported moisture developed into widespread rainfall replace the dry easterlies (AUSEJ) that predominate during the winter. During the monsoon, westerly winds increase in the low level layer with strong upper-level easterlies, yielding a tropical circulation with a deep Baroclinic structure. Along about 10-15^0 S a line of strong cyclonic shear separates lower latitude westerlies from higher latitude easterlies *(McBride and Nicholls, 1982).*

Monsoon mechanism: Monsoon typically last 1-3 weeks *(Wheeler and Hendon 2004).* Burst, break and Interaseasonal variability of the monsoon, typically affected by the following factors: (1) Barotropic instability, (2) Local thermodynamic involves a gradual built up of low-level moist static energy and convective available potential energy results primarily from an increase in surface temperature *(McBride and Frank, 1999),* (3) Arrival of the eastward winds of Madden-Julian oscillation (MJO), which in it's active phase creates a favorable environment for tropical cyclones *(Wheeler and Hendon, 2004; Hung and Yanai, 2004)* and (4) large-scale westward propagating disturbances, leading to the intrusion of multitude troughs, suggestive of an influence on the monsoon by equatorial Rossby waves *(McBride 1983; Hendon et al. 2007).* The influence of Interannual variability and ENSO (anomalies from June-Nov) is exerts considerable influence on Australian rainfall, were at El Niño period the monsoon trough is shifted to the east along with the rainfall and tropical cyclone activity. It's observed a negative correlation trough the transitional season of the monsoon rain (Sep-Nov), when northern Australia is still in a trade wind regime. Once the monsoon is active, the correlation of wet season rainfall and ENSO is near zero. *(Nicholls et al. 1982)* The onset of the monsoon suggests to be related to the strength of the Indian monsoon, which capable of driving SST variation, warm in the western Indian Ocean and cold to the north of Australia, effect the onset of Australian monsoon *(Hung et al. 2004).*

4. **Methods**

4.1. The model system

4.1.1. The Ocean-Land-Atmosphere-Model general circulation model

The model used is Ocean-Land-Atmosphere-Model (OLAM) *(Walko and Avissar, a.2008, b.2008; Walko et al., 2000)*, which is a relatively new global General Circulation Model (GCM) that allows "nesting down" to any desired resolution using a flexible mesh refinement technique that works on either triangular or hexagonal grid structure. The physical climate components of OLAM are based on a global version of the well know Regional Atmospheric Modeling System (RAMS) (see details in Table 1).

Table 1. Model components for the simulations carried out during this research

Model aspects	Chosen scheme
Dynamics	Non-hydrostatic, sigma-vertical coordinate
Grid structure	Arkawa-C grid stagge, Hexagon grid cells, cut cell method over terrain
Radiative transfer	RRTMg and Harrington scheme for the simulation with 200 km and 50 km grid resolution respectively
Turbulence	Smagrorinsky (1963) deformation-K closure scheme with stability modifications made by Lilly (1962) and Hill (1974)
Cumulus convection	Modified KF_eta
Cloud microphysics	Single-moment bulk scheme - Walko et al (1995), with look -up table bin-micro for autoconversion and sedimentation (Feingold et al, 1998) and non-hydrometeor thermo (Walko et al, 2000)
Land Surface	Soil/vegetation/snow parameterization - LEAF 4
Ocean Surface	Monthly sea surface temperature, Sea Ice cover (NCEP)

RAMS developed as a mesoscale model *(Pielke et al., 1992)* that has been used extensively around the world by many research groups. OLAM is capable of simulating one or more regions of interest at very high spatial resolution while keeping the rest of the world at a

coarser spatial resolution, and it carries out a consistent, two-way communication between events in the mesoscale and global portions of the domain. The variable-resolution dynamical simulations are far more computationally tractable than the simulations of the entire world at mesoscale resolution of typical GCMs. Because OLAM is a global model, there are no lateral boundaries, as is the case with most dynamical downscaling methods, and thus most of the issues associated with lateral boundaries are not present in OLAM *(Medvigy et al. 2011).* OLAM grids contain regions of gradual transition from higher resolution to coarser resolution (i.e., no abrupt lateral boundaries) *(Walko and Avissar, 2008a).* OLAM can be used in applications with time scales that range from short-term weather forecasting to long-term climate change predictions *(Medvigy et al. 2010).* OLAM uses an unstructured grid with a choice of hexagonal cells that easily conforms to the globe without a coordinate transformation. The current state-of-the-art grid configuration in OLAM allows local mesh refinement to any degree without the need for special grid nesting algorithms. All communications between regions of different resolution is by conservative advective and diffusive transport *(Medvigy et al. 2010).* The consistent regional-to-global scale communication makes OLAM an ideal tool for investigating the possible impact of large-scale afforestation in semi-arid regions on regional and global scale (section 5 - 8), at the same time to analysis the possible effects of different areas of the ocean on the land cover change (section 8.2.3).

4.1.2. The Land-Ecosystem-Atmosphere Feedback Land-surface model

The Land-Ecosystem-Atmosphere Feedback (LEAF) is the land model employed in OLAM. LEAF is a standard soil/vegetation model (*Lee, 1992*; *Walko et al. 2000*), simulates interactions between the biosphere at the land surface and the free atmosphere and the exchanges of water and energy fluxes. LEAF is a second generation of land model (bio-physical model) that determine the exchanges of radiative, momentum, and sensible and latent heat fluxes between the land surface and the lower atmosphere. In determining these exchanges within each model grid cell, the models take into account atmospheric forcing (solar radiation, temperature, humidity, wind and precipitation) and in particular, the role of vegetation and other land surface properties. LEAF includes prognostic equations for soil

temperature and moisture for multiple layers, vegetation temperature, and surface water including dew and intercepted rainfall, snow cover mass, and thermal energy for multiple layers, and temperature and water vapor mixing ratio of canopy air. Exchange terms in these prognostic equations include turbulent exchange, heat conduction, and water diffusion and percolation in the snow cover and soil, longwave and shortwave radiative transfer, transpiration, and precipitation *(Walko et al. 2000)*. The model required land surface characteristics such as albedo, surface roughness, root depth, stomatal conductance, all of which control the surface fluxes. These parametrization are collected into several vegetation classification, which used when the model upload the database of global vegetation distribution, to calculate the mosaic of the land cover. The scaling up of these data within the grid cell done by weighted averaging approach. For dynamic of albedo through the season the model use NDVI index database, based on satellite measurements.

4.1.3. Experimental setup

For the following experiments we used OLAM coupled to the Harrington radiative scheme in the higher grid resolution and the Rapid Radiative Transfer Model Global version (RRTMG) for the lower grid resolution *(Price, E. et al., 2014).* The model assigned with a land cover classification and monthly NDVI for the year 2003, based on MODIS products with a spatial resolution of 5-km and 1-km respectively (*Land Processes Distributed Active Archive Center, 2012).* The vegetation classification remained constant through the simulation. Sea Surface Temperature (SSTs) and Sea Ice were prescribed from the monthly mean of NCEP/NCAR Reanalysis v2 *(Kanamitsu et al., 2002).* The simulation was initialized by National Centers for Environmental Prediction (NCEP) reanalysis *(Kalnay et al., 1996),* covering the 17-yr period 1996 - 2013.

We setup two types of simulation: The control (CON) and the afforestation (AFFO). The first with the current state of plant function type (PFT) over the area of interest, and the afforested scenario with a single land cover classification representing a new PFT of semi-arid planted forest like Yatir. The new PFT assigned over the Sahel [16^0E-40^0W, 10^0-15^0N], and N-Aust [122^0-146^0 E, 17^0-22^0 S], close to total size area of 2.6 E6 km^2 and 2.1 E6 km^2 respectively. The parameterized parameters of Yatir forest were based on an inventory of

field base laboratory starting from 2000 (see details in Table 2) (*Rotenberg & Yakir 2010*).

The main experiments were based on 17 years simulations (1996-2012), with the first two years as a spin-up. The simulations were done with unified CLS of 200-km (~2 degree), with control (CON-2d) and afforestation over the Sahel (AFFO-2d-S) and over North-Australia (AFFO-2d-NA) (see details in Table 3).

As the resolution used in the simulation can affect the results *(Medvigy et al., 2008, Medvigy et al., 2011)* we also carried out simulations with model grid structure with globally 200-km characteristic length scale (CLS) and 50-km CLS over whole Africa and the Indo-Australian Ocean domains (Fig. 6; see Table 3 for list of simulations). The simulated period was 1/2000 – 12/2005, with three years of spin-up, and the flowing three years after, were used for analysis.

All simulations done with grid's vertical structure consisted from 50 layers, ranging in thickness from 50m near the surface to 2000m near the model top at 45km. The time step of the model was set for 45 sec simulation time and 1800 sec for updating radiation calculation. Analysis of the large-scale afforestation response is estimated by the mean difference between the experiments that exclude that forcing. Seasonal values for summer time in Africa: Jun-Aug, JAS and in Australia: Jan-Mar, JFM, are produced by averaging the corresponding monthly mean values. SSTs and Sea-Ice were prescribed with NCEP reanalysis *(Kalnay et al., 1996)* for each month of the period. To test the sensitive of afforestation on generating the initial condition for changing the climate over the Sahel, sensitivity test were carried out; simulations with different Yatir PFT, on a scale from bare soil to dense tree forest (for simulations list, and more details see section 5.2.3.2.).

Table 2. Biophysical parameters for various vegetation classes, and the new suggested vegetation class of Yatir.

Parameterization	Bare soil/desert	Short grass	Yatir	Evergreen needleleaf	Evergreen broadleaf
Albedo veg green	0	0.21	0.12	0.14	0.14
Albedo veg brown	0	0.43	0.24	0.24	0.24
Emissivity	0	0.96	0.97	0.97	0.97
Simple ratio NDVI	0	5.1	5	5.4	4.1
Total area index	0	4	3 max	8	7
Steam area	0	1	0.1	1	1
Veg clump	0	0	1	1	1
Veg frac cover	0	0.75	0.56	0.8	0.9
Veg height [m]	0	0.3	10	20	32
Root depth	0	0.7	1.5	5	5
Dead frac	0	0.7	0	0	0
Min canopy resistance	0	100	286	500	500

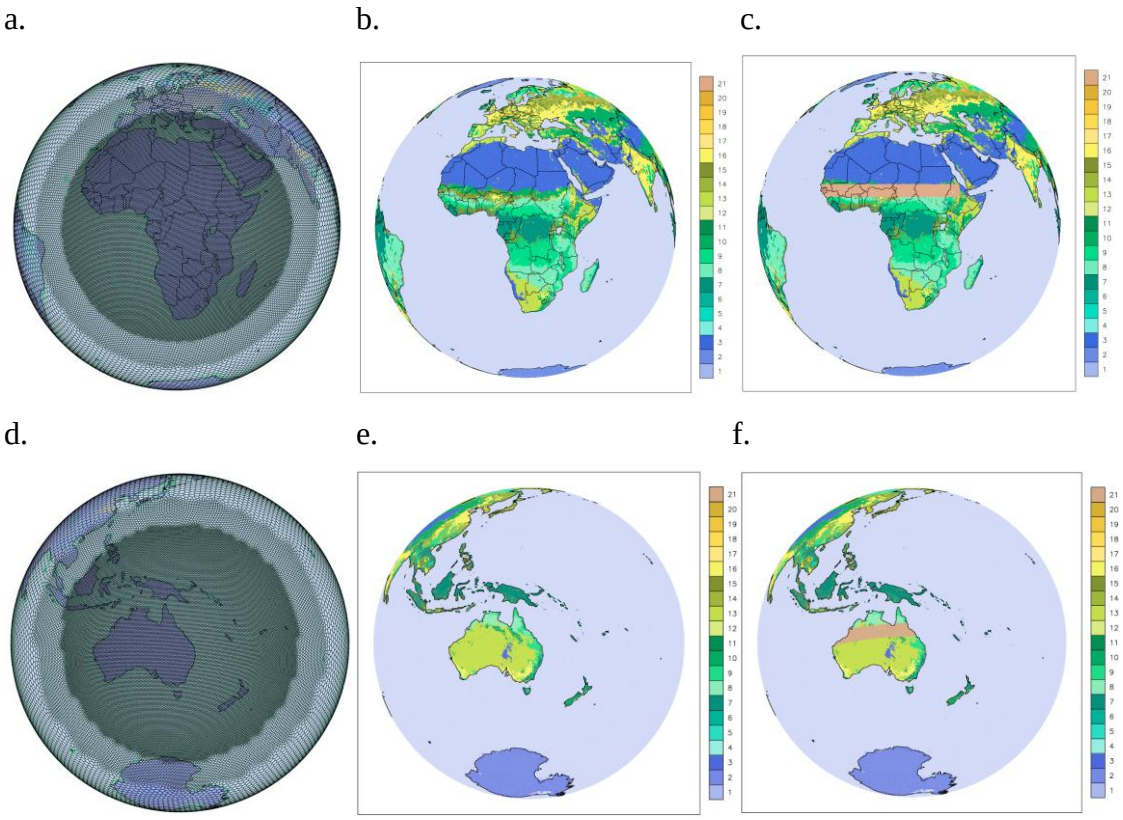

Figure 6. (a) OLAM's grids structure: variable resolution, globally 200 km grid size and gradually increase to 50 km. (b) LEAF land cover class's type for the CON simulation and (c) AFFO simulation with Yatir vegetation type (number 21) over the Sahel. The same grid structure and land cover for North Australia (d) to (f).

Table 3. Summary of numerical experiments
Abbreviations: Control simulation (CON), Afforestation scenario (AFFO), Sahel (S), North Australia (NA), Two and Half degree gird horizontal resolution (2d and 0.5d), Characteristic Length Scale (CLS), Sea Surface Temperature (SST), Plant Function Type (PFT)

Experiments	Boundary condition	Period
CON-2d	Atmospheric grid structure of CLS 200 km unified globally. Monthly climatological SST and sea ice averaged over the period 4/1996 to 12/2012, using NCEP/NCAR reanalysis.	17 years
AFFO-2d-S	Atmospheric grid structure of CLS 200 km unified globally. Forced by Yatir PFT over the Sahel [16^0E-40^0W, 10^0-15^0N], monthly climatological SST and sea ice averaged over the period 4/1996 to 12/2012, using NCEP/NCAR reanalysis.	17 years
AFFO-2d-NA	Atmospheric grid structure of CLS 200 km unified globally. Forced by Yatir PFT over Australia [115^0-150^0 E, 17^0-22^0 S], monthly climatological SST and sea ice averaged over the period 4/1996 to 12/2012, using NCEP/NCAR reanalysis.	17 years
CON-0.5d-S	Atmospheric grid structure of CLS 200 km unified globally and gradually increases to CLS 50-km over Africa. Monthly climatological SST and sea ice averaged over the period 1/2000 to 12/2005, using NCEP/NCAR reanalysis.	3 years
CON-0.5d-NA	Atmospheric grid structure of CLS 200 km unified globally and gradually increases to CLS 50-km over Australia. Monthly climatological SST and sea ice averaged over the period 1/2000 to 12/2005, using NCEP/NCAR reanalysis.	3 years
AFFO-0.5d-S	Atmospheric grid structure of CLS 200 km unified globally and gradually increases to CLS 50-km over Africa. Forced by Yatir PFT over the Sahel [16^0E-40^0W, 10^0-15^0N], monthly climatological SST and sea ice averaged over the period 1/2000 to 12/2005, using NCEP/NCAR reanalysis.	3 years
AFFO-0.5d-NA	Atmospheric grid structure of CLS 200 km unified globally and gradually increases to CLS 50-km over Australia. Forced by Yatir PFT over North-Australia [115^0-150^0 E, 17^0-22^0 S], monthly climatological SST and sea ice averaged over the period 1/2000 to 12/2005, using NCEP/NCAR reanalysis.	3 years

4.2. Model Evaluation

We evaluated the model performance by comparing simulated climatology to the data available from reanalysis and observation databases. In particular, the spatial patterns of the climatology (precipitation, surface air temperature, atmospheric circulation, and energy budget) in observation and in the model experiment CON-2d were analyzed. We note, however, that comparison of data re-analysis and observation, does not necessarily provide

an absolute reference, as re-analysis data and observations, are also associated with uncertainties, which at time can be significant *(Medvigy et al., 2010; Sylla et al., 2009, 2010).* The evaluation was therefore not meant as calibration but as validation of the model capability in reproducing the main patterns and characteristics of the relevant climate parameters in the main relevant areas. Overall, the model evaluation indicated that it did capture the main climatological features in the research areas, and it was expected that remaining differences are either within the range of acceptable uncertainty, or will have little effect on the comparative experiments carried out in this study.

4.2.1. Model validation in Sahel region

The main features of the large-scale circulation (see details section 3.4; Fig. 7) and precipitation (Appendix A.1) are reproduced by the model, in comparison with available observations from Global Precipitation Climatology Project (GPCP) v2.2 *(Adler et al., 2003)* on a $2.5^{\circ} \times 2.5^{\circ}$ grid, Climatic Research Unit (CRU) TS3.21 *(Harris et al., 2014)* on a $0.5^{\circ} \times 0.5^{\circ}$ grid and Tropical Rainfall Measuring Mission Project (TRMM), Product 3B43, v7 *(Huffman and Bolvin, 2014)* on a $0.25^{\circ} \times 0.25^{\circ}$ grid, and re-analysis data from NCEP *(Kalnay et al., 1996)* 2.5-degree. In JAS, the ITCZ is at its northernmost position and the West African monsoon rainfall is at its maximum. CRU and GPCP locate precipitation in a zonal band between the equator and 15^{0} N, in which rainfall decreases northwards. The monthly average results (Fig. 12b) show some bias between observations and model simulation, mainly at the monsoon rainy season (JAS), of less then ~1 mm d^{-1}. Previous studies have shown that simulation of African precipitation by models is sensitive to the physical parameterization and grid resolutions *(Emanuel and Rothman., 1999; Steiner et al. 2009; Pal et al. 2007).* Fig. 13a-b, Appendix A.2, show SAT monthly average, from CRU, NCEP, in comparison to model simulations CON-2d. This comparison with observation and re-analysis indicates an opposite annual trend of the SAT compared to precipitation at JAS, were the model vs. data bias is lowest around summertime, as a result of dominant clouds cover at this time of the year. Such bias can be associated with cloudiness, temperature advection, surface water, albedo and energy fluxes, but remain within the range of 2^{0}C, indicating the model performance is comparable to other regional models *(e.g. McGregor et al. 1998; Sylla et al.,*

2010). The position of the key features of CON-2d [NCEP] in the region compared well with observation (Fig. 7), including the core of the Tropical Easterly Jet (TEJ) at the 200 mb with speed higher than -15 [-15] m s^{-1}, the African Easterly Jet (AEJ) core at 600 mb with speed -10 [-12] m s^{-1}, the Monsoon Westerlies (MW) around 900-850 mb with speed 5 [2] m s^{-1} and the position of the Sahara Heat Low (SHL) (Fig. 8). Underestimation of the AEJ's strength is consistence with previous modeling studies, with range of ± 3 m s^{-1} *(Cook., 1999, Thorncorft and Blackburn., 1999, Cornforth et al., 2009 and Sylla et al., 2010).* The CON simulations compared with the available data indicated a deeper pressure system of the SHL. Associated with the SHL are strong south WM winds around ~10^0 N, to the south of the heat low, and northeasterly winds to the north (Fig. 8). The model simulates the northeasterly winds to the north of the heat low well, but underestimates the south WM to the south (Fig. 7). As the result, the model-simulated precipitation does not extend as northwards as the data indicate, with mean Sahel rainfall being underestimated (Fig. 12a-b, Appendix A.1), which could be associated with the bias in SAT noted above and relatively weaker meridional temperature gradient compare to NCEP. Weaker meridional temperature gradient over North Africa in the model simulation is also linked to weakening of the vertical shear of zonal wind, AEJ, and surface westerly winds over the Sahel (Appendix A.3).

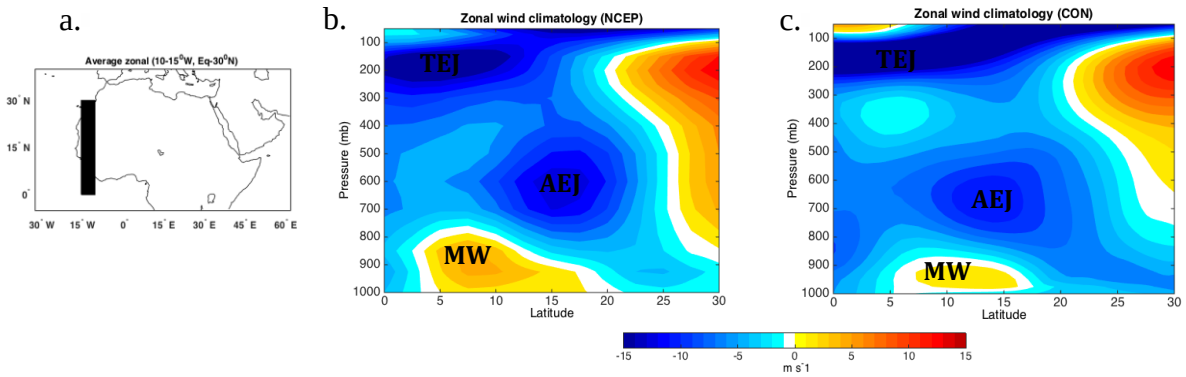

Figure 7. Observed and model simulated seasonal mean (JAS) over Africa, of zonally (10^0W- 15^0W) of zonal wind (m s^{-1}) for the period 1998-2012. (a) Zonal wind average area, (b) NCEP and (c) CON-2d

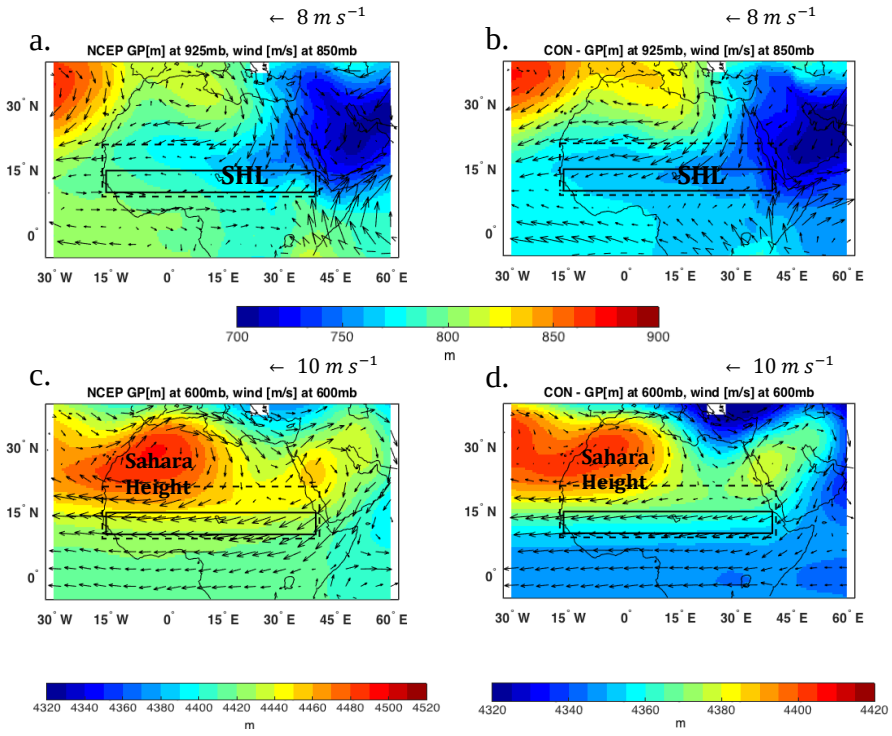

Figure 8. Geopotential height (GP) and total wind vectors (m s^{-1}) of NCEP and CON-2d in JAS for the period 1998-2012. (a) – (b) : GP 925 mb and wind at 850 mb, (c) – (d) : GP and wind at 600 mb. Contour interval is 10[m].

The surface energy budget component of the CON-2d simulation compared with Cloud and the Earth Radiation Energy System (CERES) observation database from NOAA on a $1^{\circ} \times 1^{\circ}$ grid indicated a relative bias of Rnet between CON to CERES of about -15%. This was associated with less clouds cover in the simulation, and was consistent with the effects on Surface Air Temperature (SAT) noted above. Similar model-data difference in the surface energy where not considered to be problematic in similar studies using the same model *(Medvigy et al., 2010).*

4.2.2. Model evaluation in North Australia

The spatial patterns of the climatology in observation and in the model experiment CON-2d were compared. The model simulated the main regional circulation patterns (see details in section 3.5; Fig. 10). In the CON-2d simulation, high pressure system is developing at the 30^0 S, 120-135^0 E and the jet's maximum is located around 17^0 S. Strong positive

geopotential gradients support the development of strong geostrophic easterly flow, which developing into the AUSEJ (Fig. 9). Simulation results showed lower pressure system, located easterly-north to the N-Aust coast at 13^0 S, 105-115^0 E, compared to the reanalysis (NCEP) data that covers the N-Aust coast at 13^0S, 120-165^0 E.

The position of the key features of CON-2d [NCEP] at the region are shown in Fig. 10, with the Australian Easterly Jet (AUSEJ) core at 850mb with wind speed around -10 [-14] m s^{-1}, Indonesian- Australian Summer Monsoon (I-ASM) core at 900mb with wind speed around 2 [5] m s^{-1} and the westerly winds Sub Tropical Jet (STJ) located at the 200mb with wind speed around 30 [30] m s^{-1}. I-ASM is moderate in CON-2d compared to NCEP data, it can be explained due to the location of the lower pressure system (Fig. 10) over the Indonesian- Australian Sea (IAS), its located further east in CON-2d than in NCEP that stretched from the middle up to the west part of the sea. This is not significance to the average bias of precipitation (~1mm d^{-}). The long-term variability and spatial features such as precipitation (Fig. 23a-b; Appendix A.4) and SAT (Fig. 24a-b; Appendix A.5) are reproduced reasonably well in comparison with observations and reanalysis. Minimum bias of SAT and precipitation is observed in JAS and JFM respectively, which is the range of uncertainty of modeling simulation in the region (*McGregor et al. 1998)*.

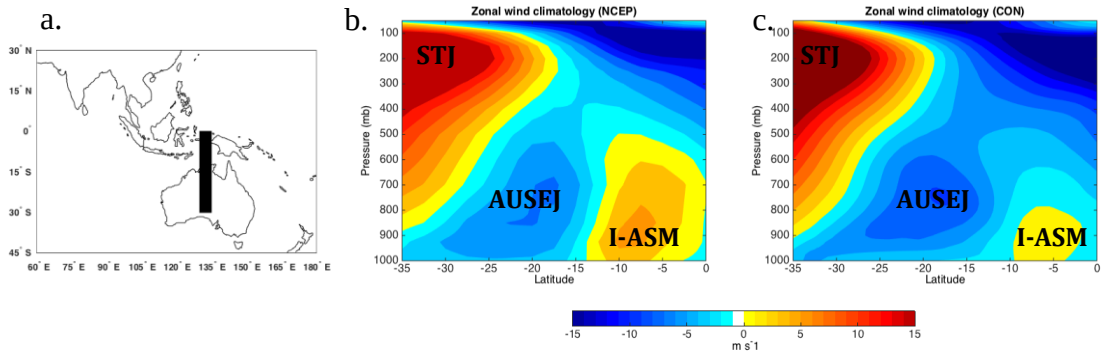

Figure 9. Observed and model simulated seasonal mean (JFM) over Australia, zonally average (10^0-15^0W) of zonal wind (m s^{-1}) for the period 1998-2012. (a) Zonal wind average area, (b) NCEP and (c) CON-2d.

The surface energy budget component of the CON-2d simulation was compared with CERES, indicating Rnet bias between CON-2d to CERES of about -24%. This was associated with less clouds cover in the simulation, which led to less downward longwave radiation flux, and the cloud cover effects on albedo and precipitation upward shortwave

radiation. Although the energy budget bias is not negligible, the simulation results found not to be a significant factor on precipitation, wind patterns and SAT.

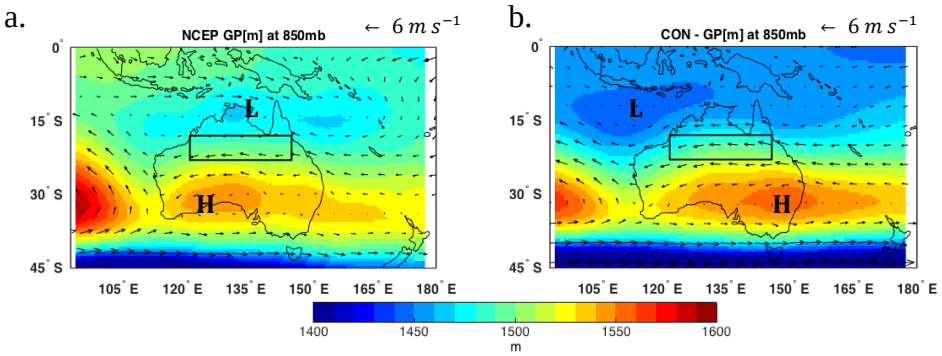

Figure 10. Geopotential height (GP) and total wind vectors (m s^{-1}) at 850 mb of (a) NCEP and (b) CON-2d in JFM for the period 1998-2012, Contour interval is 10[m].

4.3. The Yatir forest site and long-term measurements

Yatir forest spreads over 28,000 ha, located in Israel, on the southern slopes of Mount Hebron and the edge of the Negev Desert $(31° 20'N; 35° 3'E)$, at an elevation of 600m to 800m above sea level. Most of the area was planted between 1965-69. The forest is distinct from its surroundings, which are characterized as shrub lands. Yatir site is a semi-arid forest, unique among the forest flux measurements sites in the global FluxNet system and the southernmost site among the CarbonEurope system sites. It has an annual mean global radiation of about 7.5 GJ $m^{-2}y^{-1}$, annual rainfall of 285 mm and an annual mean temperature of 18.2 ^{0}C. The flux of latent heat is limited, and is supplemented by a massive sensible heat flux. The forest consists mainly of Pinus-halepensis (coniferous) trees$(> 90\%)$, with a density of $\sim 300\ trees/ha$ and a tree height of 10 m. The Yatir forest project initiated in 2000, as a field laboratory to investigate the trade-offs among water use (precipitation vs. evapotranspiration), carbon sequestration potential and surface temperature (energy budget) in the semi-arid region. Understanding these aspects that are often neglected, especially in the semi-arid region can help to better understand biosphere-atmosphere interactions.

5. Effects of Large-Scale Forestation in the Sahel Region

5.1. Introduction

Previous studies were done on the climate impact of land-cover changes over North Africa and particular the Sahel area, suggesting a tight coupling between the atmosphere and land surface *(Koster et al, 2004). Xue and Shulka (1994)* demonstrate that land surface and atmosphere interaction significantly influence the intensification of the West African summer monsoon and the AEJ. When vegetation north of 9^0 N is prescribed as a desert in a GCM, the results show that precipitation decreases up to 2 mm day^{-1} between 5 to 20^0 N, with wetter condition along the Guinean Coast (0-5^0 N), accompanied by a strengthening of AEJ. When broadleaf trees replace desert, 20^0 N up to 35^0 N, precipitation increases over much of the Sahel and Sahara and decreases over Guinean Coast, with a weakening of the AEJ. Similar results were obtain in Patricola and *Cook (2007)* study, were they investigate a mechanism of rapid climate change related to the African Humid period, between 14,800 and 5500 years ago *(deMenocal et al., 2000).* It was suggested by simulation with prescribed vegetation that positive precipitation anomalies in the Sahel occur when the desert border is located above 18^0 N (Fig. 11). The strength and position of the jet is highly dependent on the soil moisture distribution that relate to vegetation distribution, which influence the surface temperature gradient vegetation distribution *(Cook, 1999).*

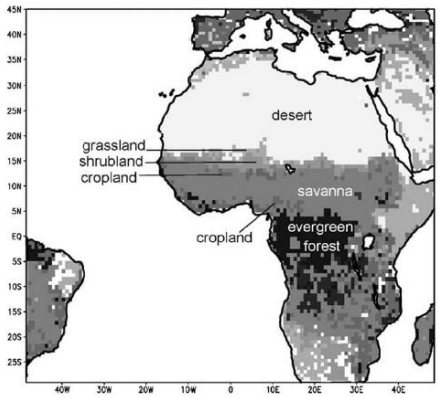

Figure 11. Land use for the present day according to the 24 category USGS (*Patricola and Cook, 2007)*

In this context the following section is examined the influence of afforestation over the Sahel on the regional climate, through surface temperature and precipitation, following the changes in the large-scale circulation.

5.2. Results

5.2.1. Changes in precipitation and surface air temperature in Sahel region

The model simulates a positive anomaly of precipitation over the Sahelian and Sahara. The results show a coherent anomaly changes that stretching zonally across the afforested area, and its maximum displaced northward up to 20^0 N as can be seen in the 95% confidence map of precipitation (Fig. 12e). The zonally pattern breaks over the high topography of Ethiopian heights in East Africa, which is consistent with previous studies *(Hagos and Cook, 2007).* Monthly average results of precipitation over the Sahel region show that rain formed around April and ending around November (Fig. 12b). The maximum effect of afforestation in increased precipitation appears in the summertime (JAS), with positive bias of 0.8 mm d^{-1}. Other significant results are shown in the analysis of the Interannual variability in JAS months, which showed positive anomalies almost over the whole period time of the simulation (Fig. 12a). More results that support the condition of increases cloud formation though cooling the atmosphere profile and increasing moisture are presented in Appendix B.

The afforestation effects on the regional surface temperature, resulted in a cooler SAT in summer time, with the same zonally pattern as in the precipitation results, with in the 95% confidence level (Fig. 13e). In addition to the forest as a cooling factor, the shape of the area with cooler SAT anomalies, determined as a results of change in cloud cover, which extending into the south Sahara desert. The monthly SAT average, show local minimum values at summer time, and as a result of afforestation, cooler effect is seen all around the year, with maximum effect at summer time with the decreases of -1.3℃ on average (Fig. 13a). The Interannual variability of JAS show consistency of lower SAT almost for all the simulated period, were most of the time the anomalies rang between 0℃ to -2℃(Fig. 13b).

Both the SAT and precipitation anomalies results of the JAS Interannual variability and 95% confidence level of monthly average precipitation and SAT maps, indicates the high robustness of the afforestation results on cooling and increasing amount of precipitation over the afforested region and beyond it in to the desert area.

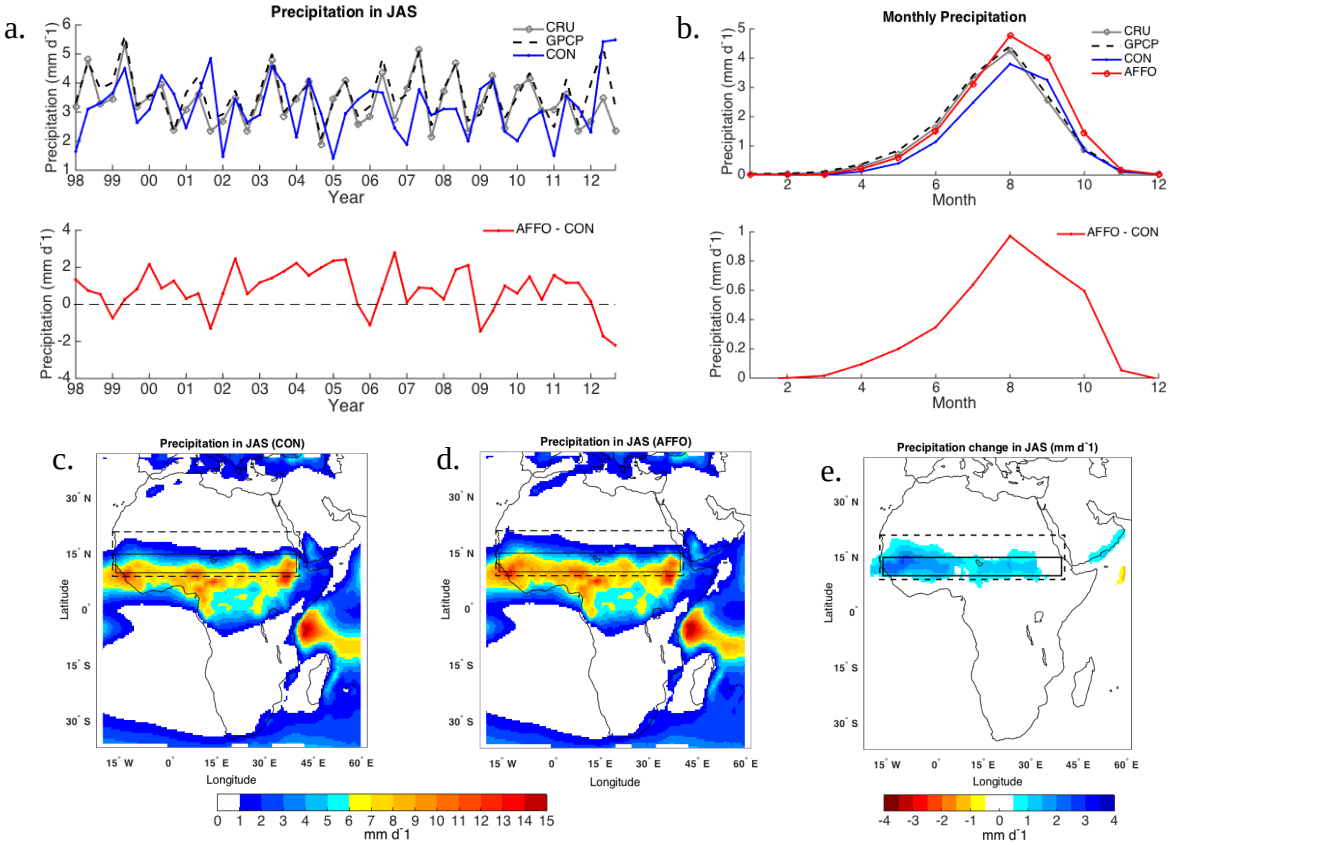

Figure 12. Observation and model simulated of Precipitation over Africa between the years 1998-2012: (a) Time series of Sahel rainfall for July-September (JAS) mean and (b) Seasonal evolution of precipitation, over the area 10^0-20^0 N, 16^0 W-40^0 E (solid line). (c)-(e), Spatial patterns of observed seasonal mean (JAS): (c) CON-2d, (d) AFFO-2d-S and (e) bias between AFFO-2d-S – CON-2d with 95% confidence level. The dash lines cover the footprint area [10^0-20^0 N, 16^0 W-40^0 E].

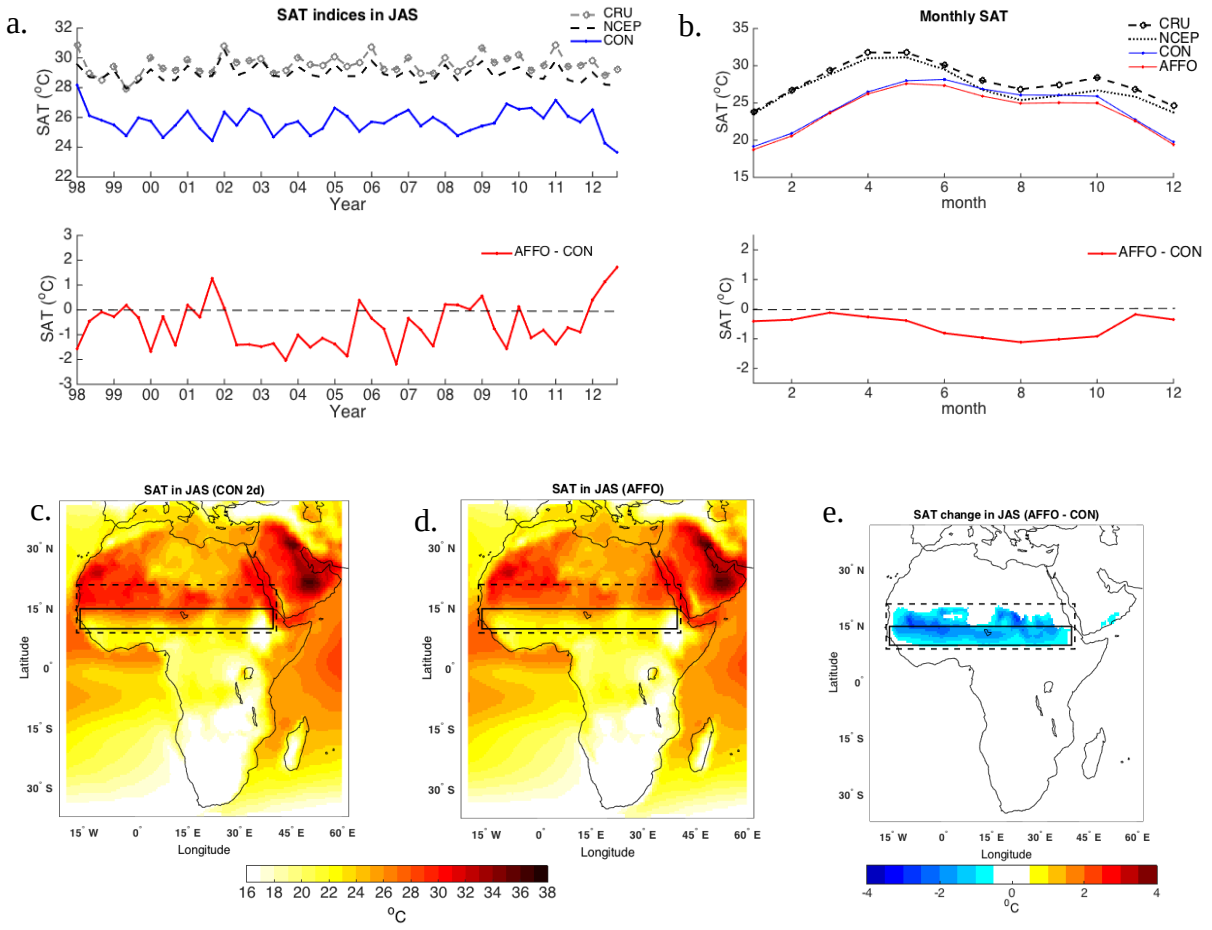

Figure 13. Observation and model simulated of the surface air temperature (SAT) over Africa between the years 1998-2012: (a) Time series of SAT for July-September (JAS) mean and (b) Seasonal evolution of SAT, over the area 10^0-15^0 N, 16^0 W-40^0 E (solid line). (c)-(e), Spatial patterns of observed seasonal mean (JAS): (c) CON-2d, (d) AFFO-2d-S and (e) bias between AFFO-2d-S – CON-2d with 95% confidence level. The dash lines cover the footprint area [10^0-20^0 N, 16^0 W-40^0 E].

5.2.2. Key process underlying changes in precipitation and surface-air-temperature in Sahel region

5.2.2.1. Changes in large-scale circulation – Sahel

As mentioned above, as a result of afforestation, the amount of precipitation increase and its maximum displaces northward up to 20^0 N (Fig. 12e) and SAT over the region become cooler (Fig. 13e). Addressing these phenomena is carried out by investigation of the change in the main circulations of this region. The main circulations of the region are shown in Fig. 14: at 600 mb the level of the jet maximum is shown at the 15^0-20^0 N, the

development of high over the land surface, centered at the 30^0 N around Greenwich meridian, strong positive geopotential gradients between the north and south of the high support strong geostrophic easterly flow (AEJ). At low-level 925mb, low pressure covers northern Africa and is associated with the heat low over the Sahara (SHL). As a result of afforestation the following changes are seen: a. Negligible change of SHL, were it has become higher over the Sahel area (Fig. 14c).

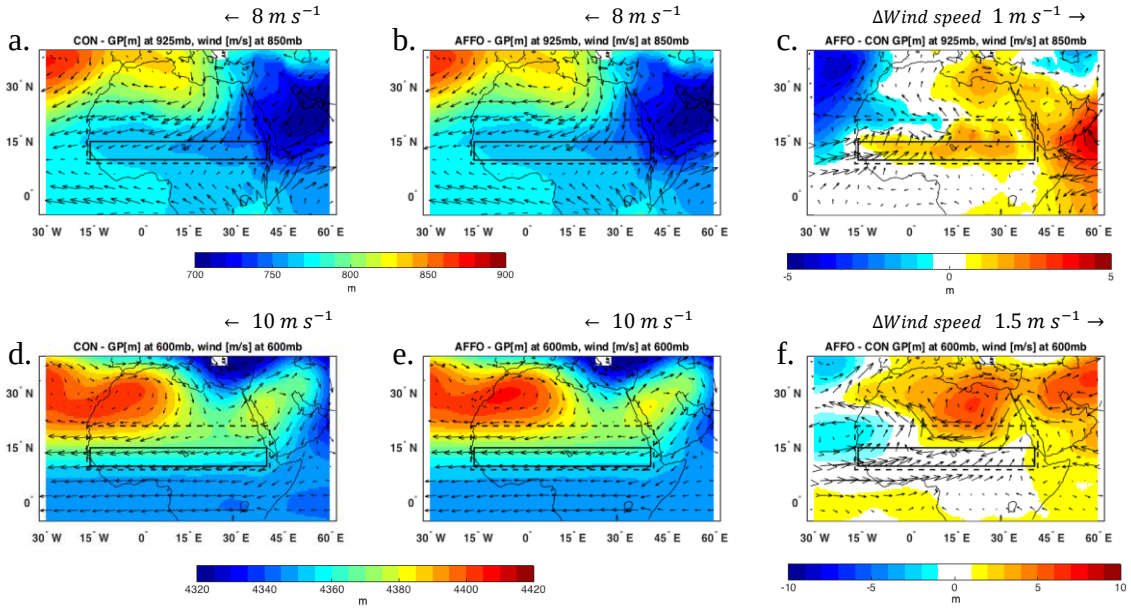

Figure 14. Geopotential height (GP) and total wind vectors (m s^{-1}) of CON-2d and AFFO-2d-S in JAS for the period 1998-2012. (a) – (c) : GP 925 mb and wind at 850 mb, and (d)- (f) : GP and wind at 600 mb. Contour interval is 10[m], Solid lines represent the afforested area [10^0-15^0 N, 16^0 W-40^0 E].

b. Weaker and northward-displaced AEJ, with a weaker core at 700 mb, extend between 5-15^0 N, were it located above the area of decreasing gradient air temperature and c. Weaker MW at the low levels over the forested area 10-15^0 N (Fig. 15c). Studies suggest that the latitudinal position and intensity of the AEJ depends upon the location of the strongest surface temperature gradient via the thermal wind balance (*e.g., Cook 1999; Thorncorft and Blackburn 1999; Thorncorft et al. 2003*). Therefore development of a weaker AEJ (Fig. 15c) is due to the consist cooler SAT that developed over the afforested area (Fig. 13a,e). Although MW is weaker, the AEJ's weakness enables MW to penetrate, and enhancement the moisture flux convergence *(Cook, 1999).*

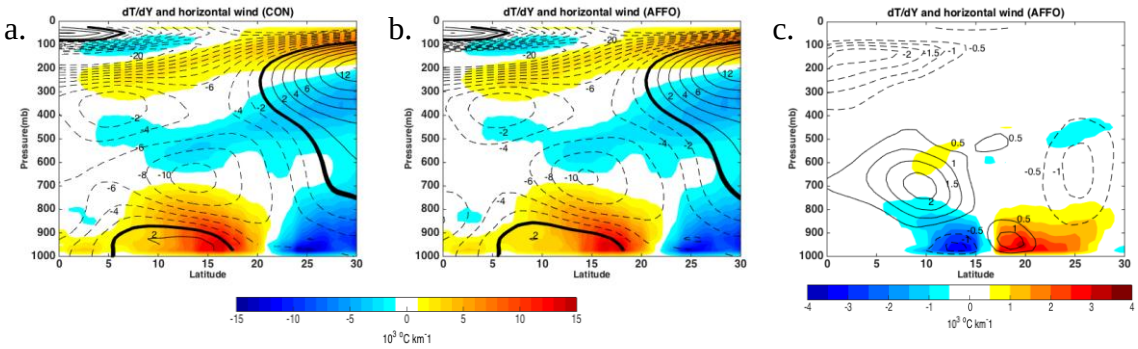

Figure 15. Observed and model simulated seasonal mean (JAS) over Africa, of zonally (10^0W- 15^0W) averaged meridional temperature gradient dT/dy (^{0}C per 1000 km) and zonal wind (m s^{-1}) for the period 1998-2012. (a) CON-2d-S, (b) AFFO-2d-S and (c) AFFO-2d-S – CON-2d.

5.2.2.2. Changes in Moisture flux convergence – Sahel

Addressing the connections between the AEJ and precipitation in the context of large circulation, the climatology column moisture in the model was examined. To do so we used the convective Moisture Flux Convergence (MFC) terms to identify the regional controls of the moisture supply for the West African monsoon.

MCF expression - arises from the conservation of water vapor in pressure coordinates:

(1) $\frac{dq}{dt} = S,$

(2) $\frac{dq}{dt} = \frac{\partial q}{\partial t} + u\frac{\partial q}{\partial x} + v\frac{\partial q}{\partial y} + w\frac{\partial q}{\partial p},$

u, v and w represent the three dimensional wind components, and q is the specific humidity; *S* represents the storage of water vapor, which is the difference between the sources and sinks of water vapor following an air parcel. Scale analysis of water budget equation for the atmosphere, for time intervals longer than a month the difference between precipitation and evaporation becomes very close to the convergence of the atmospheric water vapour flux.

(3) $S = E - C = E - P$

Were *E* is the evaporation rate into the air parcel and C is the condensation rate into the air parcel. Using the assumption that all the condensed water immediately precipitates (P) out (*Palmen and Holopainean, 1962*).

Using the continuity equation:

(4) $\frac{\partial u}{\partial x} + \frac{\partial v}{\partial y} + \frac{\partial w}{\partial p} = 0,$

the equation can be rewritten in flux form, which conserves the total mass of moisture:

(5) $\frac{\partial q}{\partial t} + u\frac{\partial q}{\partial x} + v\frac{\partial q}{\partial y} + w\frac{\partial q}{\partial p} + q\left(\frac{\partial u}{\partial x} + \frac{\partial v}{\partial y} + \frac{\partial w}{\partial p}\right) = E - P$

(6) $\frac{\partial q}{\partial t} + \nabla \cdot (qv_h) + \frac{\partial}{\partial p}(qw) = E - P$

Were $\frac{\partial q}{\partial t}$ is the local rate of change of q, $\nabla \cdot (qv_h)$ is the horizontal MFC term (wind components u and v, east-west, north-south respectively), $\frac{\partial}{\partial p}(qw)$ is the vertical MFC term and *E-P* is the sources and sinks. By vector identity, horizontal MFC can be written as:

(7) $MFC = -\nabla \cdot (qv_h) = -v_h \cdot \nabla q - q\nabla \cdot v_h$

(8) $MFC = -u\frac{\partial q}{\partial x} - v\frac{\partial q}{\partial y} - q\left(\frac{\partial u}{\partial x} + \frac{\partial v}{\partial y}\right)$

Were the horizontal advection term is:

(9) $-u\frac{\partial q}{\partial x} - v\frac{\partial q}{\partial y}$

and the convergence term is:

(10) $-q\left(\frac{\partial u}{\partial x} + \frac{\partial v}{\partial y}\right)$

(*Benjamin et al, 2004; Banacos and David, 2005*).

In order to acquire an understanding of the various mechanisms responsible for the transport of water vapour by the general circulation of the atmosphere, it is convenient to expand the mean quantities from Eq. 7. The mean quantities of the *MFC* equation, may be expanded according to the scheme: $\overline{q\bar{v}_h} = \bar{q}\bar{v}_h + \bar{\hat{q}}\bar{\hat{v}}_h + \overline{\acute{q}\acute{v}_h}$, where the total moisture flux $\overline{q\bar{v}_h}$ partitioned into the component achieved by the mean circulation $\bar{q}\bar{v}_h$, the stationary eddies $\bar{\hat{q}}\bar{\hat{v}}_h$ and the transient eddies components $\overline{\acute{q}\acute{v}_h}$ (Eq. 11) (*Peixoto and Oort, 1983*).

(11) $MFC = -\nabla \cdot (\overline{q\bar{v}_h}) = -\nabla \cdot \left(\bar{q}\bar{v}_h + \bar{\hat{q}}\bar{\hat{v}}_h + \overline{\acute{q}\acute{v}_h}\right)$

The stationary eddies anchored to features such as mountain rages on the Earth's surface and so appear in time-averaged (e.g., monthly mean) maps, whereas the transient eddies are smeared out to invisibility is sufficiently long time average. Since this study done on the afforestation effect, within an area with pretty homogenic topographic, and the analysis is based on the long-term monthly average, the transient and stationary eddies components are considerably smaller compared to the mean circulation and therefore not presented.

As was mention in the previous section, the effect of afforestation on the wind features, led to a weakening and northward-displacement of the AEJ, enable deeper

penetration of westerly winds inland, carry moisture further into the African inland, leads to the increasing of convergence at the southern border of the Sahel and at the a northern border of the footprint area, about 10^0N and 20^0N respectively. Moisture convergence decreased over the Guinean coast and the afforested area about 5^0N and 12.5^0N-15^0N respectively (Fig. 16c,f). According to these experiments, then a weaker jet will be associated with increasing precipitation in the Sahel and south Sahara, and decreasing of precipitation over north of Guinean coast (Fig. 12e). Moisture convergence occurs all over the atmospheric profile up to 600 mb with peaks up to 700 mb. The shape of the MFC area defined according the position and intensity of the AEJ, were in both CON and AFFO simulation, the maximum MFC flowing the south border of the AEJ profile, were its act as barrier to the penetration of the MW or moderating convergence development from a Sahelian local source of moisture (Fig. 16d,e). Therefore increasing of convergence at 10^0 N up to 600mb and 20^0 N up to 800mb is associated with the decreasing AEJ intensity, and at 20^0 N it also related to the decreasing of the southward wind direction (see Fig 14f). The decreasing convergence at 15^0 N related to the displacement of the convergence pattern.

The advection component of the MFC equation has lower contribution, around 10% of the total moisture flux. In general, during the monsoon rainy season, the area of south of Sahara desert is influenced by the moisture advection flux, flowing from the south as a results of WM increases (Fig. 17a,d). The results show that the shift of the convergence area northward, leads to penetration of the maximum advection flux to latitude 20^0-25^0 N and its decreasing in latitude 15^0-20^0 N, where the convergence flux increases (Fig. 17c,f).

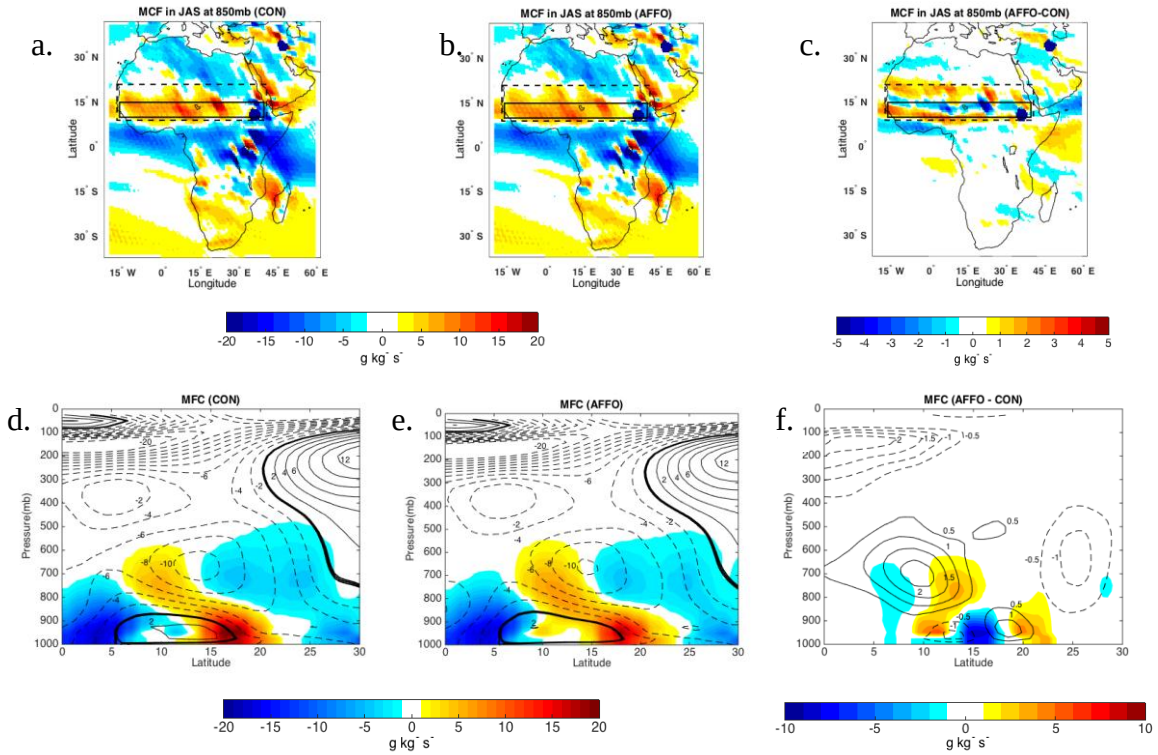

Figure 16. Model simulated seasonal mean (JAS) for the period 1998 -2012, of Moist Flux Convergence (MFC) convergence/divergence (positive/negative) over Africa, for the 850 mb, (a) CON-2d, (b) AFFO-2d-S and (c) AFFO-2d-S – CON-2d, Solid lines represent the afforested area [10^0-15^0 N, 16^0 W-40^0 E], and the dash lines cover the footprint area [10^0-20^0 N, 16^0 W-40^0 E]. Zonal cross section (10^0-15^0W) averaged meridional MFC, (d) to (f) the same as a-b. Units in [10^3 g kg^{-1} s^{-1}]

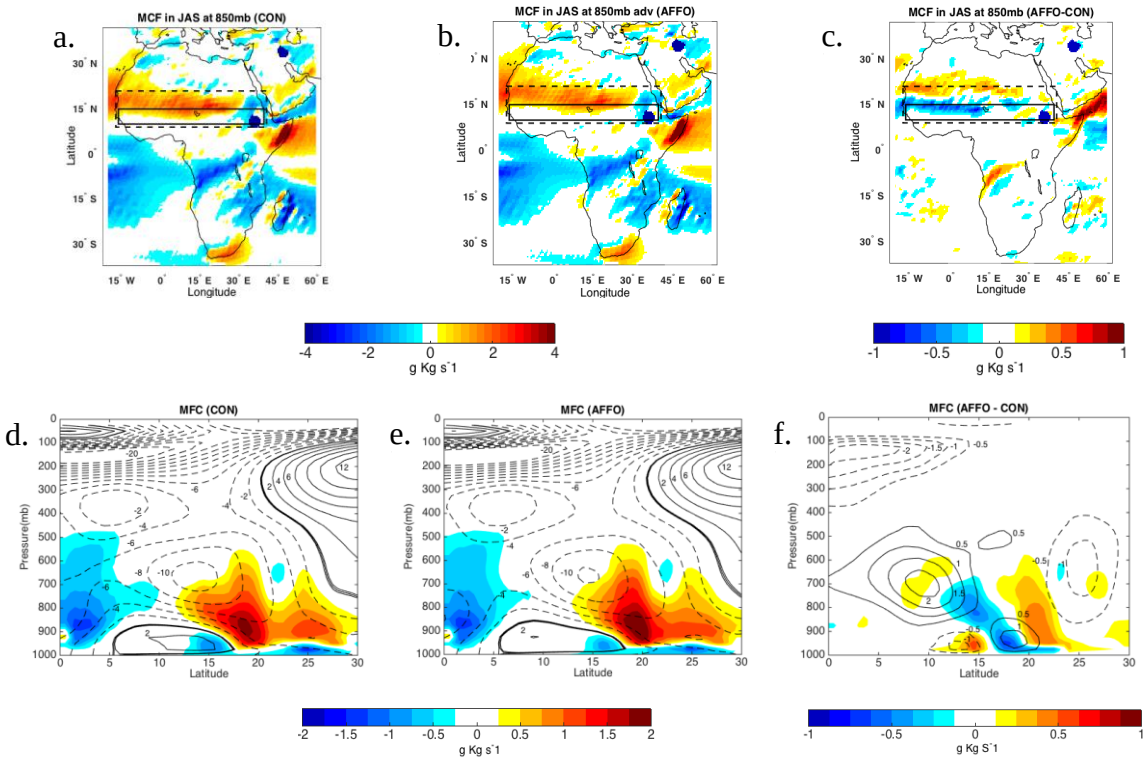

Figure 17. Model simulated seasonal mean (JAS) for the period 1998 -2012, of Moist Flux Convergence (MFC) advection in to/out of the region (positive/negative) over Africa, for the 850 mb, (a) CON-2d, (b) AFFO-2d-S and (c) AFFO-2d-S – CON-2d, Solid lines represent the afforested area [10^0-15^0 N, 16^0 W-40^0 E], and the dash lines cover the footprint area [10^0-20^0 N, 16^0 W-40^0 E]. Zonal cross section (10^0-15^0W) averaged meridional MFC, (d) to (f) the same as a-b. Units in [10^3 g kg^{-1} s^{-1}]

5.2.3. Sensitivity analyses - Sahel

5.2.3.1. High-resolution simulation

Comparison between the lower and higher grid resolution of 200 km (2d) and 50 km (0.5d), show consistency, when in both 0.5d and 2d the simulation results with positive anomalies of precipitation over the afforested area. The higher resolution simulation, generates larger influenced area with much higher anomalies values than the lower resolution; In the Sahel the positive precipitation anomaly is up to 5 mm d^{-1}, which covers the afforested area and much of the area up to 20^0 N. Negative anomalies covers the Guinea coast and the Inland area between 5^0 -10^0 N, ~2.5 mm d^{-1} (Fig. 18c,d).

The result of the SAT's anomalies between 0.5d to 2d, show almost the same spatial coverage area, with lower 1.5 ^{0}C at 0.5d then 2d simulation (Fig. 19c,d). As a result, the

temperature gradient is changed, and leads to lower AEJ's intensity (~ 3 m s^{-1} and northward displacement (~3^0 N) compare to 2d (Fig. 20b,d). The displacement and decreasing of intensity of the AEJ in the 0.5d resolution was much prominent, therefore leads to higher positive anomalies in the precipitation.

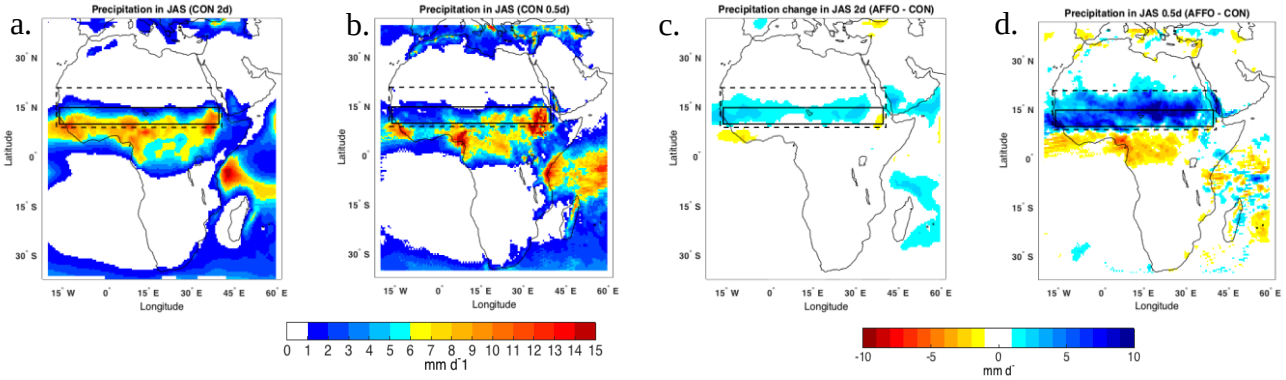

Figure 18. Model simulation of precipitation in JAS for the years 2003-2005: (a) CON-2d, (b) CON-0.5d-S, (c) AFFO-2d-S – CON-2d and (d) AFFO-0.5d-S – CON-0.5d-S. The afforested area indicated in the solid line [10^0-20^0 N, 16^0 W-40^0 E], dash lines cover the footprint area [10^0-20^0 N, 16^0 W-40^0 E].

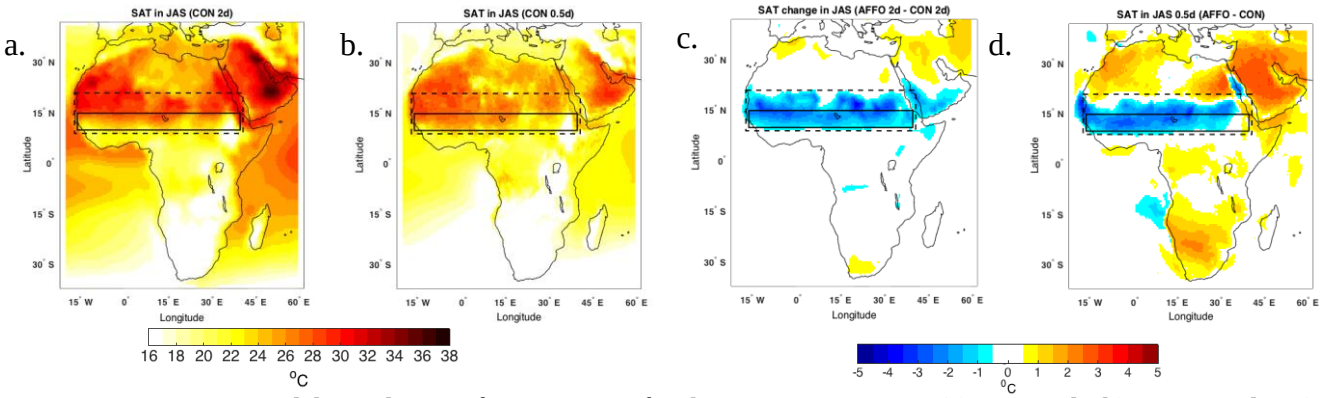

Figure 19. Model simulation of SAT in JAS for the years 2003-2005: (a) CON-2d, (b) CON-0.5d-S, (c) AFFO-2d-S – CON-2d and (d) AFFO-0.5d-S – CON-0.5d-S. The afforested area indicated in the solid line [10^0-20^0 N, 16^0 W-40^0 E], dash lines cover the footprint area [10^0-20^0 N, 16^0 W-40^0 E].

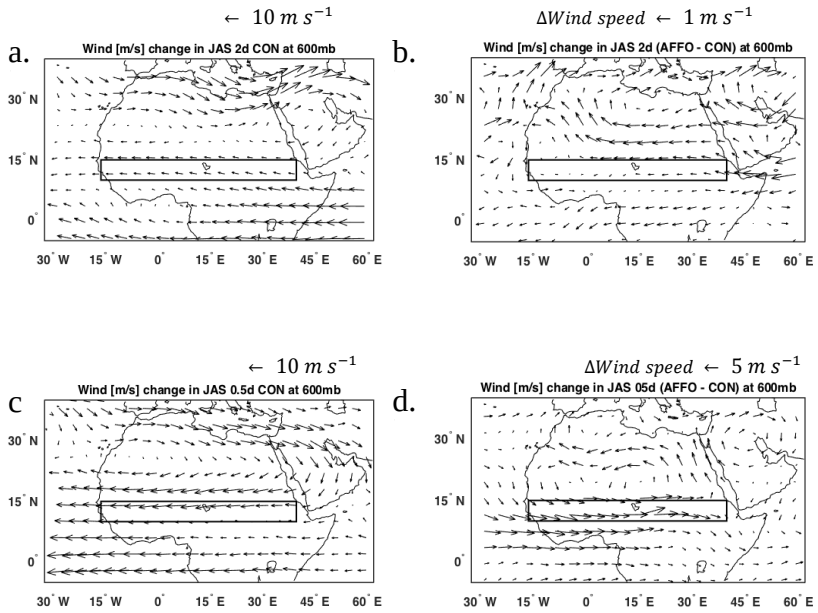

Figure 20. Total wind vectors (m s^{-1}) in JAS for the years 2003-2005: (a) CON-2d, (b) AFFO-2d-S – CON-2d, (c) CON-0.5S and (d) AFFO-0.5d-S – CON-0.5d. Solid lines represent the afforested area [10^0-15^0 N, 16^0 W-40^0 E].

5.2.3.2. Biosphere-atmosphere feedback

Multiple simulations were done, using the OLAM GCM, coupling with the land-ecosystem-atmosphere-feedback (LEAF) model. To address the question of vegetation cover influence on triggering positive mechanism, eight simulations were carried out: (1) as the control simulation SIM1 $_{(CON)}$, which represents the state condition of the Sahel, with mixed vegetation of semi-desert, short grass and tall grass, (2) simulation with afforestation scenario SIM2 $_{(AFFO)}$ over the Sahel region. Forest parameters were taken from semi-arid Aleppo pine forest parametrization (Yatir forest, Northern Negev, Israel) (Table. 2). Other simulations (SIM3 to SIM8) had the same vegetation parametrization as the SIM2 $_{(AFFO)}$ with one parameter in each simulation replaced by the corresponding value from short-grass (sh) or evergreen broadleaf (ev) parameterizations, which represent the two end-members of the vegetation spectrum. The changed parameters were: a) vegetation albedo (albv), b) vegetation height (h) and c) root depth (rd) (Table. 4). The simulation period was 2 years 2000-2002, using the first year as spin-up. Horizontal grid resolution was two degrees (~400 km) and 50 vertical atmospheric levels. SST and sea-ice were prescribed by the NCEP

reanalysis data for the relevant years. The biases between the results of each simulation (SIM2 to SIM8) and CON were calculated. Then the biases values for SIM3 to SIM8 were compared to the biases for SIM2 $_{(AFFO)}$-SIM1 $_{(CON)}$ bias. The following output variables were analyzed: surface and top of atmosphere energy budget, surface temperature and precipitation over the Sahel [16^0 E-40^0 W, 10^0-15^0 N] and for precipitation also the footprint area were calculated [16^0 E-40^0 W, 10^0-20^0 N] (Fig. 21a, b).

The analysis of monthly spatial average for the Sahel region for the rainy season in JAS showed that, when changing separately anyone of parameters under study, from the Yatir type forest (AFFO), to short grass will not affect the results. On the other hand, changing the parametrization to evergreen broadleaf trees (Table .5 and Fig. 21a), results in increasing of the net surface radiation by ~2 W m-2 for SIM4 $_{(albv\text{-}ev)}$ and SIM8 $_{(rd\text{-}ev)}$ experiments, whereas in SIM6 $_{(h\text{-}ev)}$ experiment no such effect was observed. Changes in non-radiative fluxes relatively to SIM2 $_{(AFFO)}$ - CON are much more prominent. In particular, latent heat (LE) bias increased by 13.4, 14.8 and 17.8 W m-2 in SIM4 $_{(albv\text{-}ev)}$-CON, SIM6 $_{(h\text{-}ev)}$-CON and SIM8 $_{(rd\text{-}ev)}$-CON, respectively. At the same time sensible heat (H) bias decreased by -6.6, -10.5 and 12.4 W m-2 at the SIM4 $_{(albv\text{-}ev)}$-CON, SIM6 $_{(h\text{-}ev)}$-CON and SIM8 $_{(rd\text{-}ev)}$-CON, respectively. The maximum precipitation over Sahel was observed in the SIM8 $_{(rd\text{-}ev),}$ while over the entire footprint, it observed in SIM4 $_{(albv\text{-}ev)}$, due to the distribution of the precipitation inside the footprint area. The minimum temperatures were observed at the SIM8 $_{(rd)}$, which could be explained as a result of increased water uptake capability, which in turn increases dramatically the LE and decreases the H due to evaporation process. Spatial distribution of LE, H, SAT and precipitation can be seen in Appendix C.

The simulation results showed that the root depth is a key feature in the vegetation effects in the afforestation simulation, which can influence surface temperature, and as shown in the next sections, this in turn leads to the drift of the AEJ further north, enabling the monsoon westerlies to develop convective clouds over the Sahel. The roughness (canopy height) also plays important role for the cooling of the surface, by increasing surface friction, which generates more vertical motions that: a. increases the conductivity between the canopy and the lower atmosphere layer, which is expressed into higher LE and H, b. increase clouds formation and precipitation over the forest through convergence process. Comparing different PFT hierarchy show that as land cover change from shorter vegetation, lower

rootdepth and less dense vegetation cover to a higher vegetation, deeper rootdepth and denser vegetation cover, there is not much change in the SUR-Rnet, but a more prominent changes in the LE and H on an absolute values. Non-radiative fluxes changes, cools the surface temperature as result of higher aerodynamic conductivity and the ability to extract more soil moister from the ground. The fraction of change between the bias of the experiments, show that surface temperature and precipitation also gone through big changes (Fig. 21b).

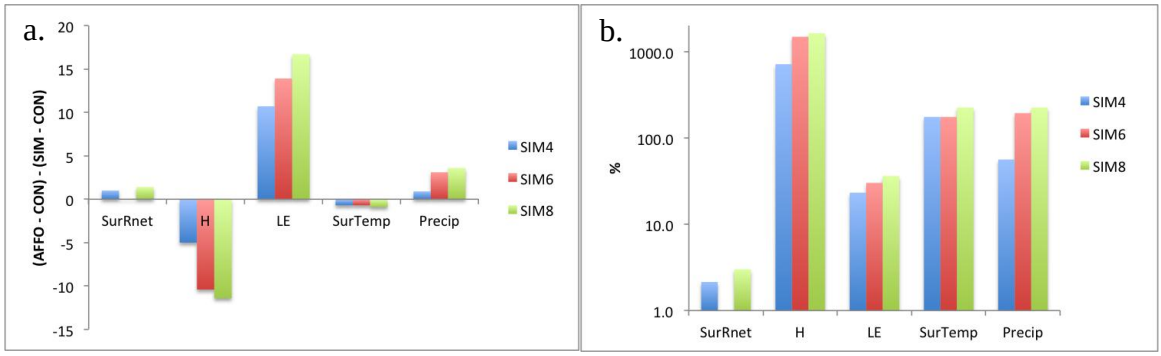

Figure. 21. a. Chart bar represents the differences with SIM2 (AFFO) - CON to SIM4 (albv) – CON, SIM6 (h) - CON and SIM8 (rd) - CON (numbers in brackets in Table 5) in Net Radiation at the surface (SurRnet) [W m^{-2}], Sensible heat flux (H) [W m^{-2}], Latent heat flux (LE) [W m^{-2}], Surface Temperature (SurTemp) [^{0}C] and Precipitation (Precip) [mm day^{-1}]. b. Differences as calculate for a. in a logarithmic scale of percentage.

Table .4 Simulations of the biophysical parameters for Yatir type forest and the adjustment values (h – canopy height, rd-root depth and albv –albedo vegetation) for the Short grass (sh) and Evergreen Broadleaf (ev) vegetation simulations.

Simulations	Parameterization	Short Grass	Evergreen Broadleaf
Triggering positive mechanism			
SIM3 (albv-sh)	Albedo veg green	0.21	-
	Albedo veg brown	0.43	-
SIM4 (albv-ev)	Albedo veg green	-	0.17
	Albedo veg brown	-	0.21
SIM5 (h-sh)	Veg height [m]	0.3	-
SIM6 (h-ev)	Veg height [m]	-	32
SIM7 (rd-sh)	Root depth [m]	0.7	-
SIM8 (rd-ev)	Root depth [m]	-	5
Impact of regional-scale land cover change			
SIM9 (d)	PFT Bare-soil/desert (albedo 0.41)		
SIM10 (sh)	PFT Short grass		
SIM11 (br)	PFT Evergreen Broadleaf		

Table. 5 Energy budgets results of the sensitivity test over the Sahel.
Surface (SUR) and Top of Atmosphere (TOA) energy budget components over the Sahel [16^0 E-40^0 W, 10^0-15^0 N] in JAS of SIM1(CON) and the differences of SIM2(AFFO), SIM4(albv-ev), SIM8(rd-ev) and SIM6(h-ev) to the SIM1(CON) with the following parameters: radiative components: Up (u) and Down (d), Short and Long wave (SW and LW), net short (dSW) and nwt long (dLW) waves and total net radiation (Rnet), Surface non-radiative components: sensible (H) and latent (LE) heat flux. Units radiation [W m-2], precipitation (mm day^{-1}) and temperature (SurTemp, ^oC). Numbers in brackets are the differences with SIM2 (AFFO) - CON.

JAS Avg	SIM1 (CON)	SIM2 (AFFO) - CON	SIM4 (albv) - CON	SIM6 (h) - CON	SIM8 (rd) - CON
SUR-SWd	317.6	-8.8	-11.5	-10	-16.1
SUR-SWu	80.8	-37.2	-37.5	-37.7	-39.2
SUR-LWd	323.4	10.2	13.2	10.2	15.4
SUR-LWu	429.9	-4.2	-7	-7.2	-8
SUR-Rnet	132.8	46.6	47.6 [1]	46.6 [0]	48 [1.4]
H	40.3	-0.7	-5.7 [-5]	-11.1 [-10.4]	-12.1 [-12.4]
LE	92.3	46.1	56.8 [10.7]	60 [13.9]	62.8[16.7]
TOA-SWd	430.6	0	0	0	0
TOA-SWu	110	-27.9	-27.1	-29.5	-24.3
TOA-LWu	282.4	-13.2	-26.8	-18.6	-27.8
TOA-Rnet	44.5	49.2	57.5	50.8	58.5
Precip Sahel	7.3	1.6	2.5 [0.9]	4.7 [3.1]	5.2 [3.6]
Precip Footprint	4.3	6.2	7.3 [1.1]	6.3 [0.1]	6.8 [0.4]
SurTemp	23.6	-0.4	-1.1 [-0.7]	-1.1[-0.7]	-1.3[-0.9]

5.3. Summary

The results of afforestation in Sahel for July-August-September, showed a lower surface temperature (1.3 ± 0.14 ℃), which led to a sequence of changes in the local atmospheric dynamics: Decreasing in meridional surface temperature gradient over the forested area, and increasing it over the drier area north of the forestation band; weakening the local low-level jet core ($1\ m\ s^{-1}$), and its displacement toward the drier edge of the forested band; deeper penetration and increasing convergence of westerlies winds inland; displacement of the maximum summer precipitation over the forested area and its drier edge ($0.8 \pm 0.2\ mm\ d^{-2} \sim 75\ mm \pm 18mm$). The higher resolution 6-years simulations were consistent with the above results, generally showing enhancement of some of the effects, with lower surface temperature over the afforested area core, compared with the lower resolution simulations

(1.5 ℃) that led to further decrease in easterly low level jet intensity ($3\ m\ s^{-1}$) and its displacement 3^0N, and further increase in precipitation ($5\ mm\ d^{-2}$). Sensitivity tests of the different vegetation parameters (e.g., albedo, roughness, root-depth) showed that the dominant parameter was the increase in root-depth, allowing the increased net radiation to enhanced evaporation and surface cooling. Roughness also enhanced surface cooling by increasing surface-atmosphere aerodynamic conductivity.

6. Effects of Large-Scale Forestation in North Australia

6.1 Introduction

Sensitivity study of the Australian Monsoon to vegetation based on geological history record show that modern humans colonized Australia burn landscapes for many reasons, such as clearing passages and hunting along the fire front, and developed agriculture *(Roberts et al, 1994).* Systematic landscape burning by early humans may have altered vegetation, particularly across vast semiarid zone, converting shrub, grass ecosystem to desert and in so doing alerting feedbacks between the biosphere and atmosphere. *Charney (1975), Cook (1999), Miller G. H (2005)* and other showed that vegetation and soil could influence the penetration of moisture into tropical regions through the recycling of water and the modification in regional atmosphere circulation. Previous modeling experiments were done to evaluate the sensitivity of monsoon moisture reaching the Australian interior as a result of change in vegetation properties *(Miller G. H et al, 2005; Ornstein, 2009).* The results of difference in monsoon precipitation for prescribed forest compare with desert, reveals that significant changes in precipitation are restricted to a well-defined region over the northern Australia and the adjacent ocean (Fig. 22)

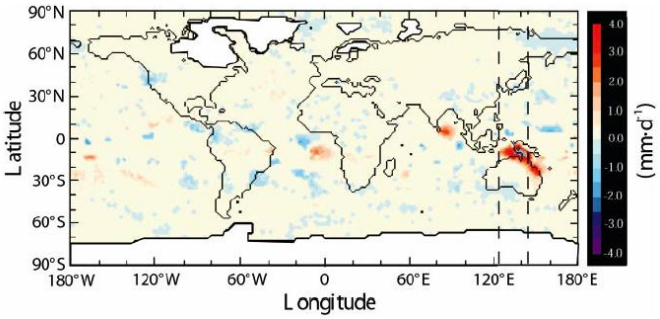

Figure 22. Difference in December-January-February (DJF) precipitation for 10 ka prescribed forest minus 10 ka prescribed desert simulation (*Miller G. H, at el. 2005)*

More detailed study on the effect of afforestation scenario over N-Aust on the regional wind, was found that the changes associated with large-scale afforestation over North Australia could influence the Australian Easterly Jet (AUSEJ), during the Indonesian-Australian Summer Monsoon (I-ASM) that controls the precipitation regime especially over

North Australia (*Drosdowsky, 1996*). Increasing precipitation following cooler surface and displacing and decreasing of the easterly Jet *(Ornstein, 2009)*.

In this context the following section is examined the influence of afforestation over the N-Aust on the regional climate, through surface temperature and precipitation, following the changes in the large-scale circulation.

6.2. Results

6.2.1. Changes in precipitation and surface air temperature in North Australia.

The model simulates maximum rainfall migrating southward, which generate a positive anomaly of precipitation over the N-Aust and Indo-Australian Sea (IAS) (Fig. 23e). The result (95% of confidence level) show a coherent positive anomaly change form, starting from the middle of the afforested area, stretching from northwest to southeast, while negative anomalies appear south to the afforested area over west Australia (Fig. 23e). Monthly average result of precipitation over the N-Aust region, show that rain starts to form around mid September until end of May (Fig. 23b). The maximum effect of afforestation in increasing precipitation appears in the south hemisphere from July to April (summertime), with mean positive bias of 0.4 mm d^{-1} over the entire afforested area. When examining the Interannual variability of JFM months indicate zero to positive anomalies almost over the whole simulation period (Fig. 23a). The non-consistency of the positive anomalies in N-Aust experiment is explained through the influence of ocean basins teleconnection (see details section 3.5).

The afforestation effects on the regional surface temperature, leading to a cooler SAT in summer time, with zonally pattern over the forest, unlike the precipitation effect (Fig. 24e). The monthly SAT average, show maximum values at the southern hemispheric summer time, and as a result of afforestation, a cooling effect is seen all around the year, with the decrease of 1℃ on average (Fig. 24a). The Interannual variability of JAS shows consistency of lower SAT almost for all the simulated period, were most of the time the anomalies range between 0℃ to -2℃ (Fig. 24b).

Both the SAT and precipitation anomalies results of the JAS Interannual variability and of monthly average precipitation and SAT maps (in 95% confidence level), indicates on the high robustness of the afforestation results on cooling and increasing amount of precipitation over the afforested region and beyond it in to the coastal area.

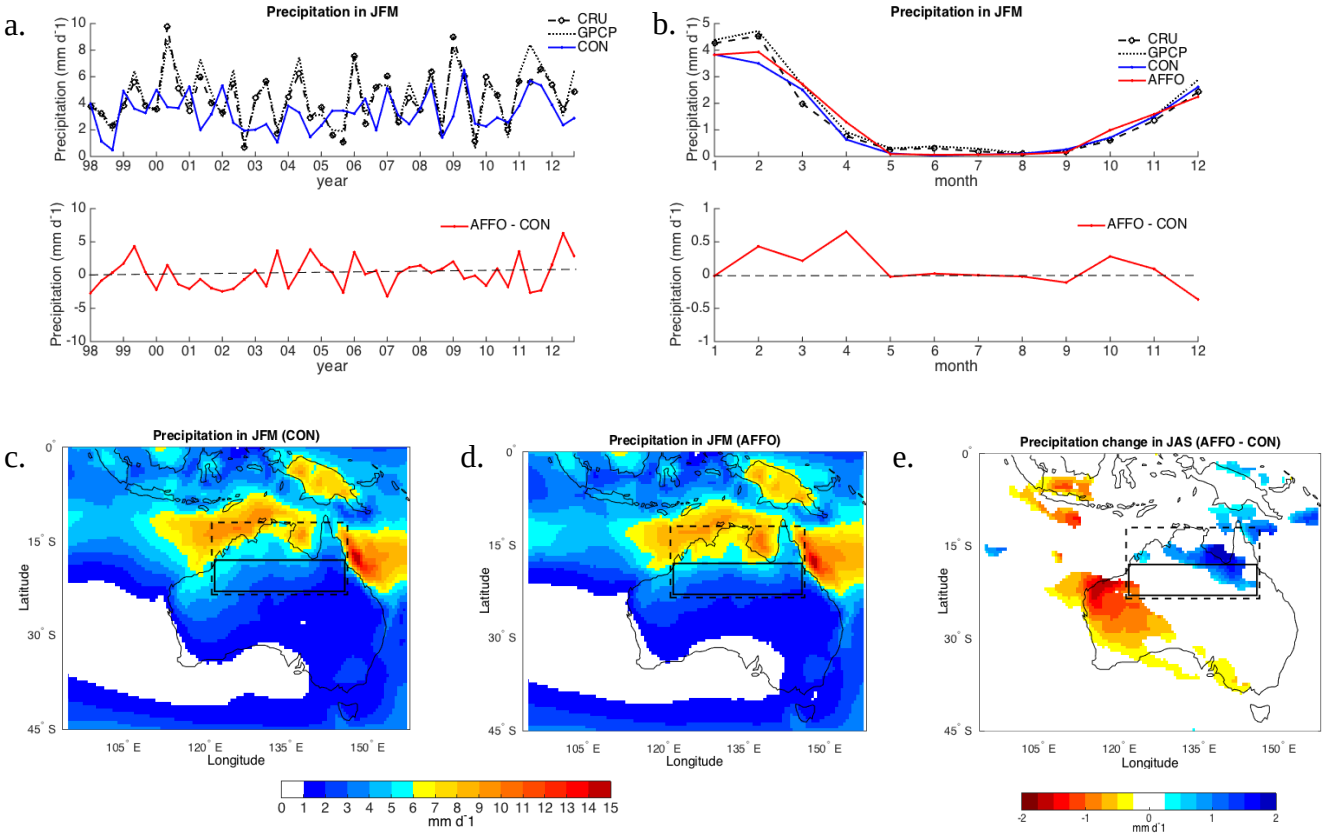

Figure 23. Observation and model simulated of Precipitation over Australia between the years 1998-2012: (a) Time series of North Australia rainfall for January-March (JFM) mean and (b) Seasonal evolution of precipitation, over the area 17^0-22^0 S, 122^0 -146^0 E (solid line). (c)-(e), Spatial patterns of observed seasonal mean (JFM): (c) CON-2d, (d) AFFO-2d-NA and (e) AFFO-2d-NA – CON-2d with 95% confidence level. The dash lines cover the footprint area [12^0-22^0 S, 122^0 -146^0 E].

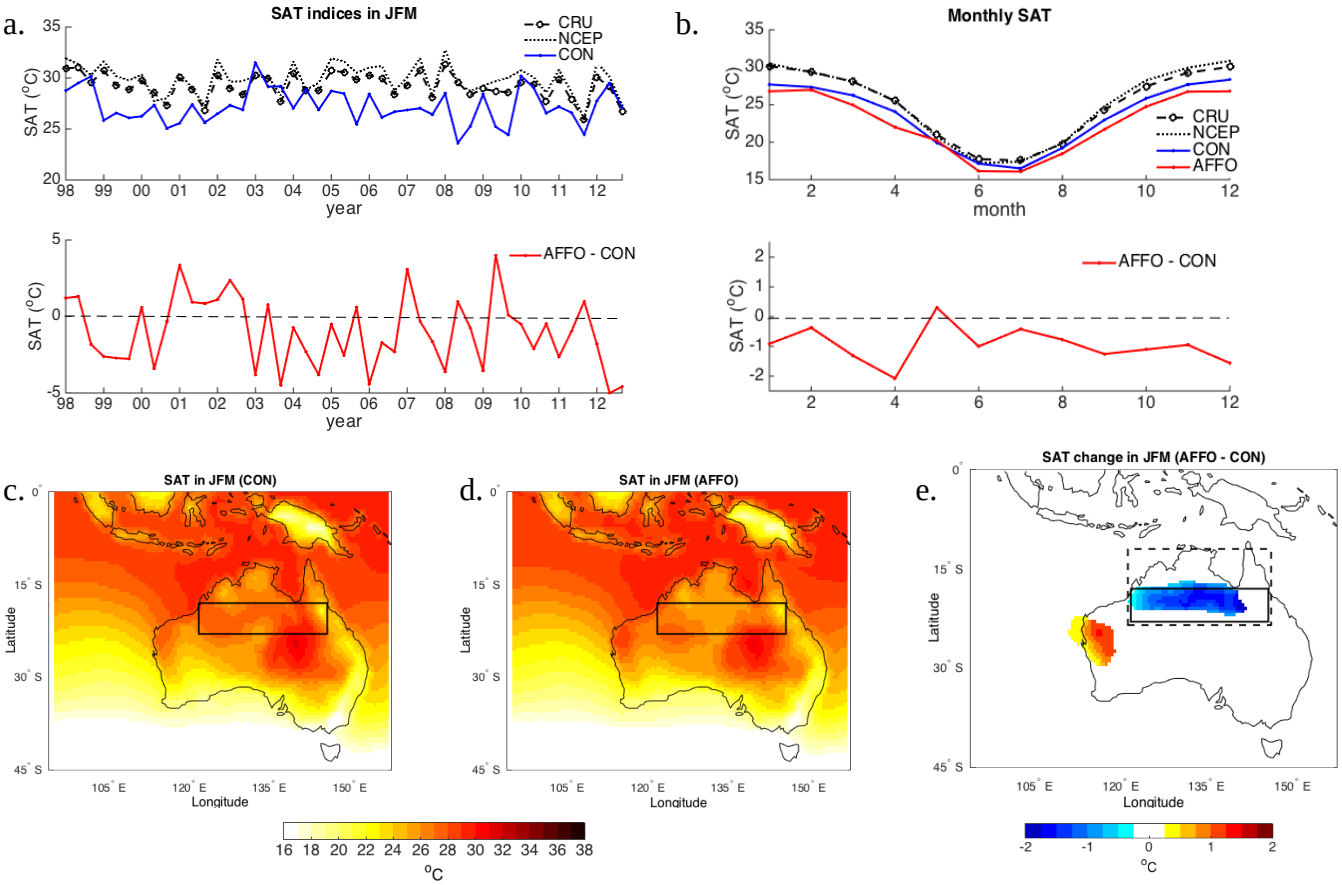

Figure 24. Observation and model simulated of SAT over Australia between the years 1998-2012: (a) Time series of North Australia SAT for January-March (JFM) mean and (b) Seasonal evolution of precipitation, over the area 17^0-22^0 S, 122^0 -146^0 E (solid line). (c)-(e), Spatial patterns of observed seasonal mean (JFM): (c) CON-2d, (d) AFFO-2d-NA and (e) AFFO-2d-NA and (e) AFFO-2d-NA – CON-2d with 95% confidence level. The dash lines cover the footprint area [12^0-22^0 S, 122^0 -146^0 E].

6.2.2. Key process underlying changes in precipitation and surface air temperature in North Australia region

6.2.2.1. Changes in large-scale circulation – North Australia

As mentioned above, as a result of afforestation, the amount of precipitation increases (Fig. 23e) and the SAT over the region becomes cooler (Fig. 24e). Addressing these phenomena is carried out by investigation of the change in the main circulations of this region. The main circulations of the region are shown in Fig. 25; a) at 850 mb the level of the AUSEJ maximum is at 15^0-25^0 S, b) the development of high pressure system over the land surface, centered at the 30^0 S and lower pressure system over the IAS at 13^0 S and c) a strong positive geopotential gradients between the north and south of the high support strong

geostrophic easterly flow (AUSEJ). As a result of afforestation, high system is increasing all over the south part of Australia were the pressure system at the north become moderate. The bias between AFFO and CON (Fig. 25c) leading to a lower pressure at the east of IAS, 10^0 S, 155^0 E, compare to the west, accompanied with an increase of the active environment of the monsoon through wind pattern (Fig. 25.c). This in turn, increases the precipitation over the footprint area [12^0-22^0 S, 122^0 -146^0 E], mainly at the northeast part area (Fig. 23e). The active environments occur relative to the monsoon trough, as shown in Fig. 26, dry air advection of the southeasterly stream poleward of the monsoon trough, converge with the equatorward of the monsoon trough, and moist maritime air is lifted in the convergent region and produces a deep moist profile (*McBride and Frank 1999)*.

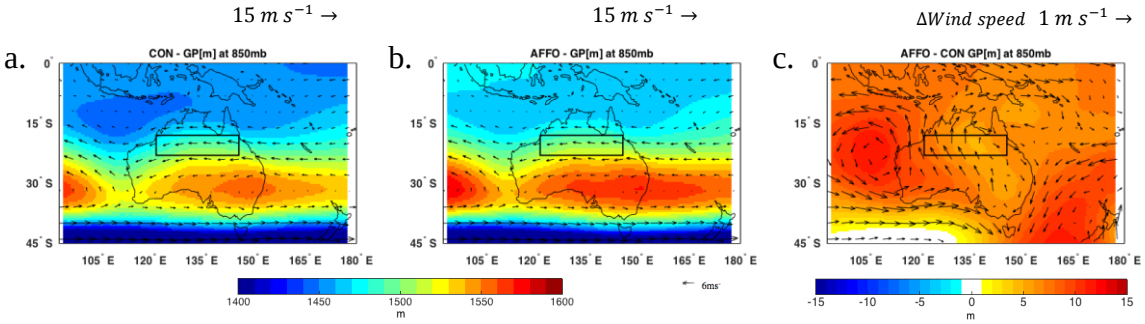

Figure 25. Geopotential height (GP) and total wind vectors (m s^{-1}) of (a) CON-2d, (b) AFFO-2d-NA and (c) AFFO-2d-NA - CON-2d, in JFM for the period 1998-2012. Solid lines represent the afforested area [17^0-22^0 S, 122^0 -146^0 E].

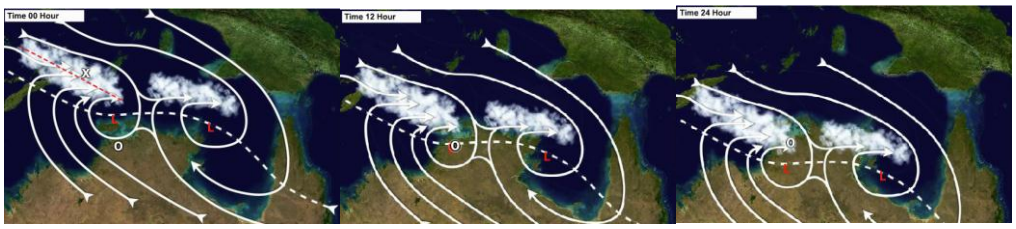

Figure 26. Schematic progress of the active and break environments relative to the monsoon trough during 24hr *(adapted form McBride and Frank 1999, presented by COMET).*

A change in the surface and atmosphere profile temperature due to afforestation show a decreasing SAT (Fig. 24e), and a weaker temperature gradient profile (Fig. 27c), over the entire forested area 15^0-20^0 S. This change leads to a weaker wind intensity (core at 800 mb) and to a southward-displacement of the AUSEJ, extended between 15^0-20^0 S, right above the area of decreasing gradient air temperature (Fig. 27c). This outcome enables the formation of

maximum southward rainfall migration over the forest (Fig. 23e), in consistency with former studies outcomes *(Ornstein, 2009),* and to our previous results from the Sahel experiment. The robustness of the results is expressed by increasing precipitation and cooler surface over the simulation time period (Fig. 23a & 24a).

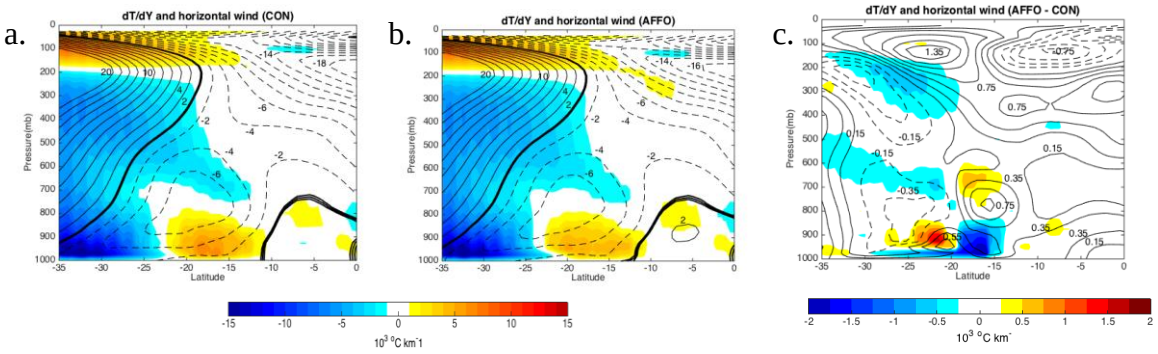

Figure 27. Observed and model simulated seasonal mean (JFM) over Australia, of zonally (130^0-135^0E) averaged meridional temperature gradient dT/dy (^{0}C per 1000 km) and zonal wind (m s^{-1}) for the period 1998-2012. (a) CON-2d, (b) AFFO-2d-NA and (c) AFFO-2d-NA – CON-2d.

6.2.2.2. Changes in Moisture flux convergence – North Australia

Moisture Flux Convergence (MFC) (for mathematical descriptions see section 6.1.1.2.) and precipitation were used to identify the regional controls of the moisture supply for the N-Aust monsoon. In general, the convergence area is seen over the (IAS) sea, when the north part of Australia is influenced by limited penetration of the rain belt (Fig. 28a,b). Results show a positive anomaly of deeper moisture penetration over the N-Aust (Fig. 28c). Profile analysis along the meridian, show that both moisture of ocean and afforestation affect the increase of the moisture convergence from the coastline around 7^0 S up to 30^0 S (Fig. 28e). Maximum convergence peak occur north of the forest border 10^0-15^0 S, and at the south border 20^0-25^0 S, both of them can be related to the weakening of AUSEJ. According to these experiments, a weaker jet will be associated with increasing precipitation in the Australian footprint (Fig. 23c). The shape of the spatial MCF at 850mb looks like two stripes of higher convergence area, over the west footprint area, around 120^0-130^0E, and over the east part 140^0-150^0E (Fig. 28c). These results consist with the wind flow regime at the monsoon as explained above.

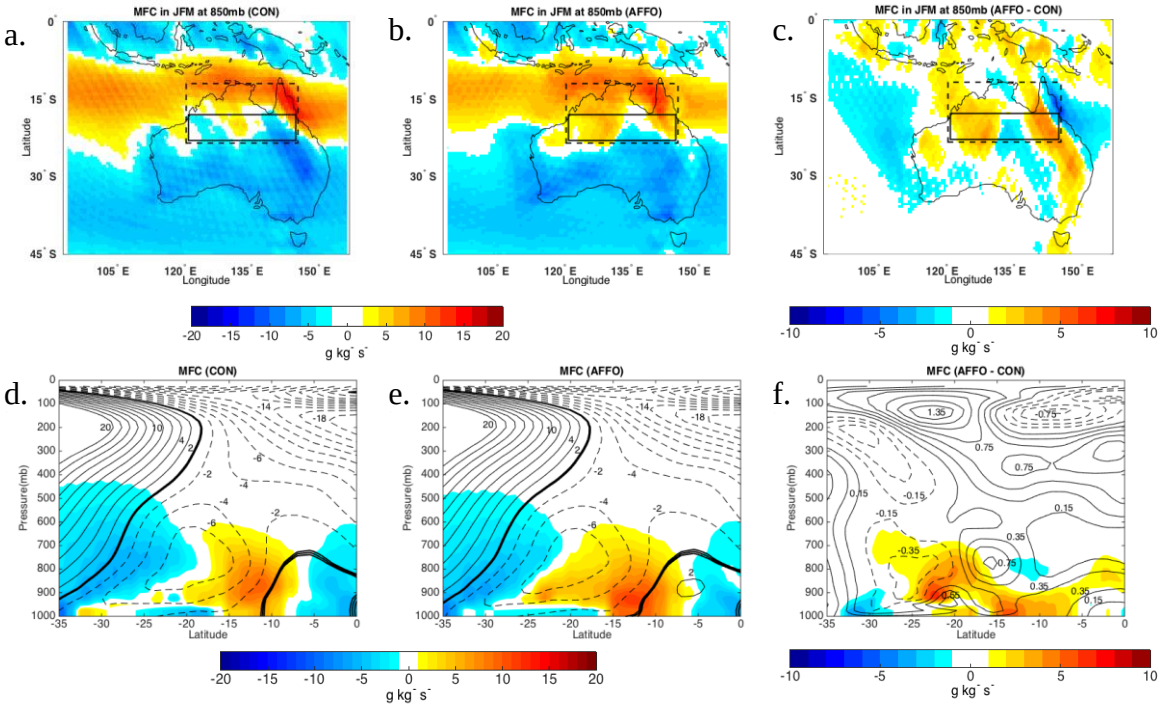

Figure 28. Model simulated seasonal mean (JFM) for the period 1998 -2012, of Moist Flux Convergence (MFC) convergence/divergence (positive/negative) over Australia, for the 850 mb, (a) CON-2d, (b) AFFO-2d-NA and (c) AFFO-2d-NA – CON-2d, Solid lines represent the afforested area [17^0-22^0 S, 122^0 -146^0 E], and the dash lines cover the footprint area [12^0-22^0 S, 122^0 -146^0 E]. Zonal cross section (130^0- 135^0E) averaged meridional MFC, (d) to (f) the same as a-b. Units in [10^3 g kg^{-1} s^{-1}]

As a results of afforestation the advection moisture flux cover bigger area over the IAS, but at the same time decreases along the coastline (Fig 29), due to increasing moisture convergence (Fig 28.c,f). Intensifying the wind pattern in the form of active environment of the monsoon, as mentioned above, leads to deeper penetrating of the advection moisture flux over the afforested area (Fig. 29.c). In general, the regions affected by the increases in the moisture convergence experience the decreasing of the advection flux, as in the Sahel experiment.

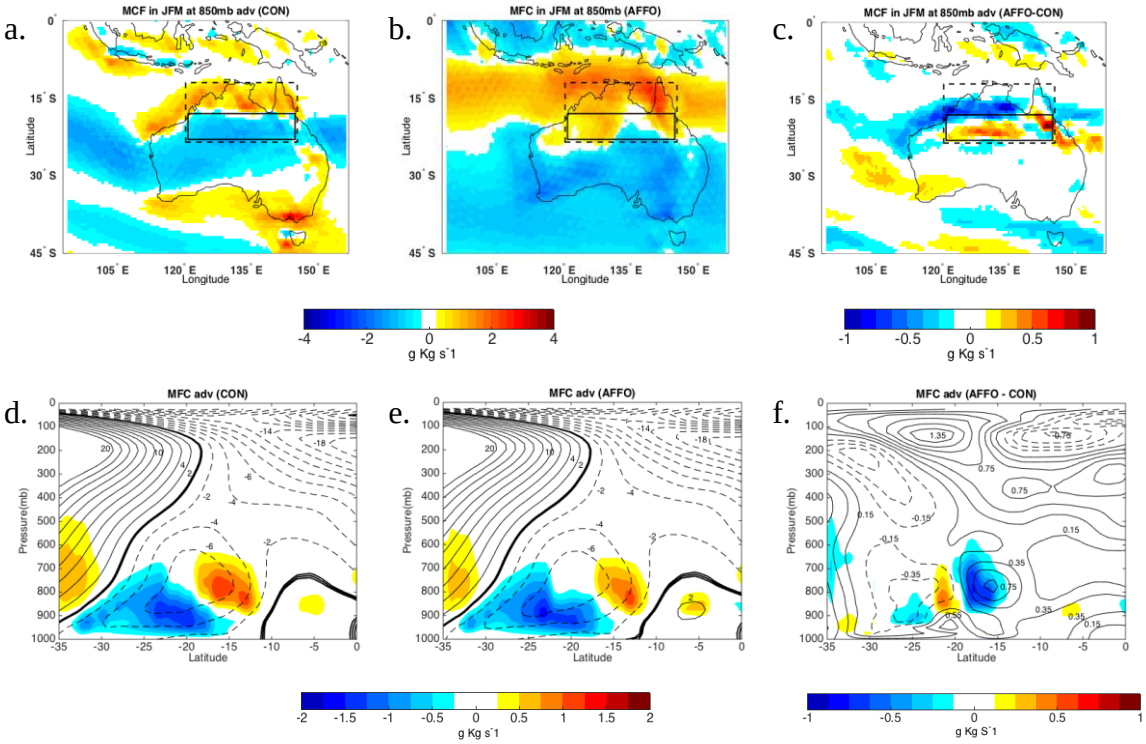

Figure 29. Model simulated seasonal mean (JFM) for the period 1998 -2012, of Moist Flux Convergence (MFC) advection in to/out of the region (positive/negative) over Australia, for the 850 mb, (a) CON-2d, (b) AFFO-2d-NA and (c) AFFO-2d-NA – CON-2d, Solid lines represent the afforested area [17^0-22^0 S, 122^0 -146^0 E], and the dash lines cover the footprint area [12^0-22^0 S, 122^0 -146^0 E]. Zonal cross section (130^0- 135^0E) averaged meridional MFC, (d) to (f) the same as a-b. Units in [10^3 g kg^{-1} s^{-1}]

6.2.3. Sensitivity analyses – North Australia

6.2.3.1. High-resolution simulation

Comparison between the lower and higher grid resolution of 200 km (2d) and 50 km (0.5d), show consistency, when in both 0.5d and 2d the simulation results with positive anomalies of precipitation over the afforested area. The higher resolution simulation generates larger influenced area with much higher anomalies values than the lower resolution; In the N-Aust the positive anomaly is up to 5 mm d^{-1}, which covers the afforested area and as well beyond the footprint area. Negative anomalies in the high-resolution experiment, covers less area in the IAS (Fig. 30c,d).

The result of the SAT's anomalies between 0.5d to 2d, show consistency; were in 0.5d simulation result in lower SAT (Fig. 31c,d) over larger area to the south of the forest

then the 2d simulation. It can be assume that this is a result of increasing cloud cover over the Australian continent. Cooler surface under the AUSEJ leads to changes in the temperature gradient, which decreases and displace southward the AUSEJ more in 0.5d than the 2d by ~2 m s^{-1} and ~3^0S respectively (Fig. 27c; 32b,d). The AUSEJ displacement and decreasing of intensity in the 0.5d resolution was much higher, therefore led to more developed wind pattern, that favor the formation of the active environment as shown in Fig. 26, which supports the significant increase in the amount of precipitation (up to 5 mm d^{-1}) as a results of afforestation (Fig. 30c,d).

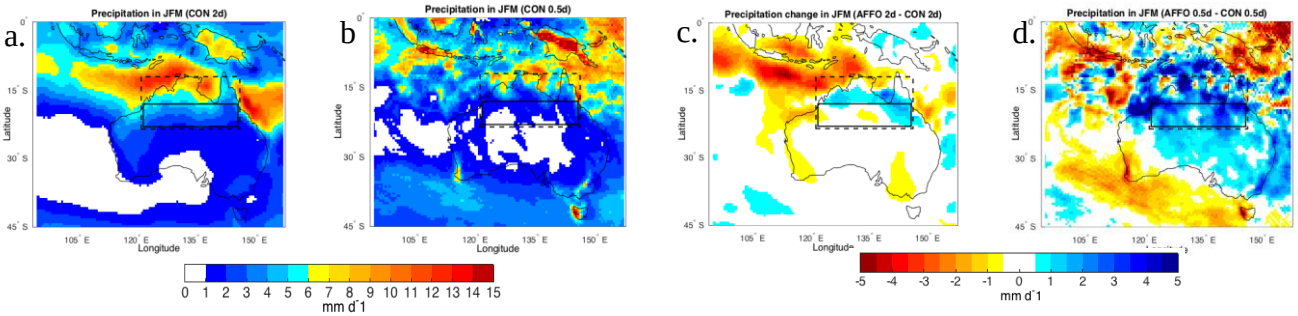

Figure 30. Model simulation of precipitation in JFM for the years 2003-2005: (a) CON-2d, (b) CON-0.5d-NA, (c) AFFO-2d-S – CON-2d and (d) AFFO-0.5d-NA – CON-0.5d-NA. The afforested area indicated in the solid line [17^0-22^0 S, 122^0 -146^0 E], dash lines cover the footprint area [12^0-22^0 S, 122^0 -146^0 E].

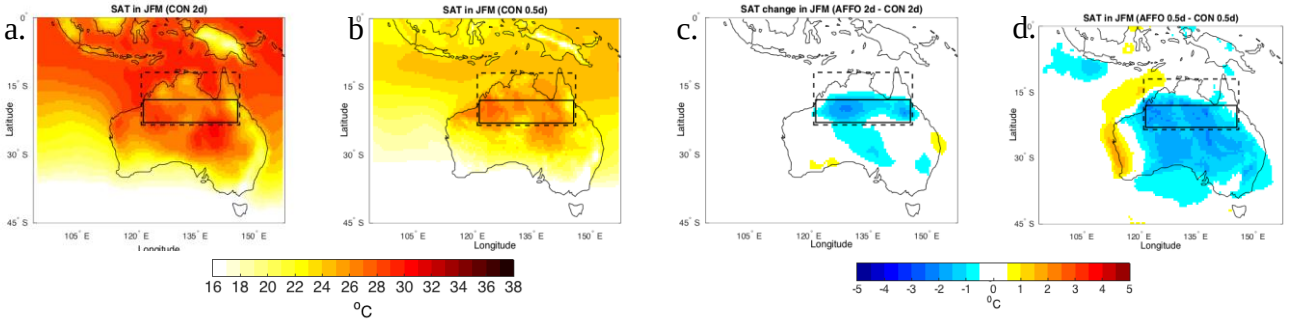

Figure 31. Model simulation of SAT in JFM for the years 2003-2005: (a) CON-2d, (b) CON-0.5d-NA, (c) AFFO-2d-S – CON-2d and (d) AFFO-0.5d-NA – CON-0.5d-NA. The afforested area indicated in the solid line [17^0-22^0 S, 122^0 -146^0 E], dash lines cover the footprint area [12^0-22^0 S, 122^0 -146^0 E].

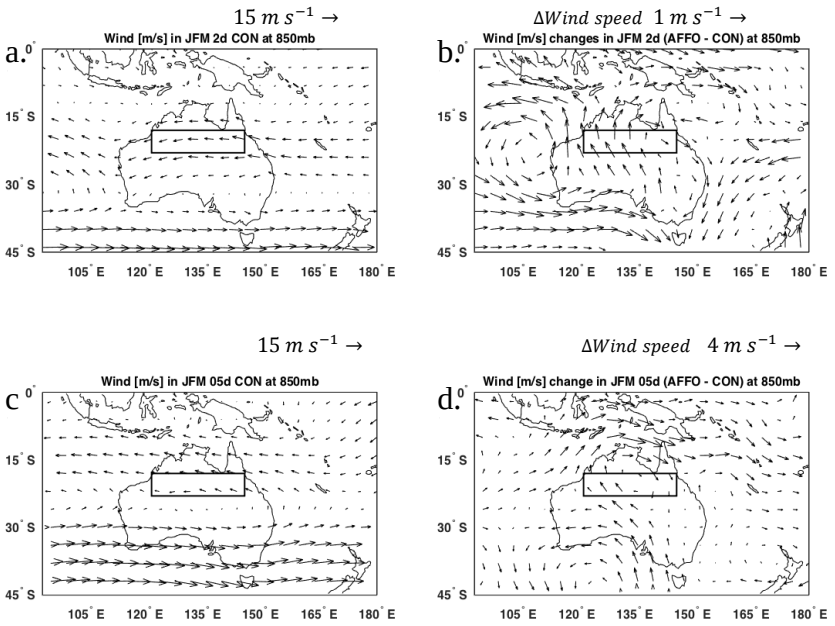

Figure 32. Total wind vectors (m s^{-1}) in JFM for the years 2003-2005: (a) CON-2d, (b) AFFO-2d-NA – CON-2d, (c) CON-0.5-NA and (d) AFFO-0.5d-NA – CON-0.5d-NA. Solid lines represent the afforested area [17^0-22^0 S, 122^0 -146^0 E].

6.3. Summary

The results of afforestation in North Australia for January-February-March, showed the same results as in the Sahel experiment, where lower surface temperature (0.9 ± 0.1 ℃), led to a sequence of changes in the local atmospheric dynamics: Decreasing the meridional surface temperature gradient over the forested area, and increasing it over the drier area north of the forestation band; weakening the local low-level jet core ($2\ m\ s^{-1}$) and its displacement toward the drier edge of the forested band; deeper penetration and increasing convergence of westerlies winds inland; displacement of the maximum monsoon rain over the forested area and its drier edge ($0.4 \pm 0.2\ mm\ d^{-2} \sim 20\ mm \pm 18m$). The higher resolution 6-years simulations were consistent with the above results, generally showing enhancement of some of the effects, lower intensity of the easterly low level jet ($2\ m\ s^{-1}$) and its displacement ($3^0 S$), which generate further increase in precipitation ($5\ mm\ d^{-2}$).

7. The Effect of Afforestation on the Partitioning of the Surface Energy Budget

7.1. Introduction

The direct change of land cover from short grass to trees leads to increasing the leaf area index (LAI), decreasing albedo, increasing roughness length (Z_0), and increasing root depth *(e.g., Sellers, 1992; Jackson et al. 1996; Narisma and Pitman, 2002).* These changes affect the partitioning of available water between runoff and evaporation, thereby affecting soil moisture and possibly rainfall. Further, these changes affect the partitioning of available energy between sensible and latent heat, affecting local air temperature *(Zhao and Pitman, 2002)*. These changes may cause to changes in the lower atmospheric circulation, and in turn to change the wind and rain pattern *(Cook , 1999)*.

To support the argument that land surface condition can influence the low-level atmosphere circulation, one should consider how the land surface temperature distribution is determined over afforested area in summer through the surface energy budget. Table 6 and 7, show results of surface energy partitioning in the Sahel and N-Aust experiments respectively, when the following components were analyzed: Surface (SUR) and top of the atmosphere (TOA) energy budget, Non radiative fluxes: Sensible (H), Latent heat (LE) fluxes, Evapotranspiration (ET), and Surface Air Temperature (SAT).

7.2 Results

7.2.1. Partitioning of the surface energy budget over Sahel

Sahel case (AFFO-2d-S - CON-2d) resulted in large increase of the surface net radiation ($9.9\ W\ m^{-2}$), mainly as a result of decrease in albedo, which reflected through SUR-SWu ($-14.8\ W\ m^{-2}$), decrease of incoming short wave radiation SUR-SWd ($-15.2\ W\ m^{-2}$), which cancel each other when calculating the net short wave radiation. Increase of downward long wave radiation SUR-LWd ($2.4\ W\ m^{-2}$) and decrease in long wave upward radiation SUR-LWu ($8\ W\ m^{-2}$), as a result of the lower surface temperature SAT (-1.3 ℃). Increasing soil moisture as a result of the new forest is expressed into higher ET, in dramatic increase of

the latent heat (LE) flux ($16.9\ W\ m^{-2}$) and a small decrease in the sensible heat (H) flux ($-5.6\ W\ m^{-2}$). Higher LE flux and lower H flux over the forested area decreases the SAT. The contribution of the clouds to SUR-Rnet ($-10.5\ W\ m^{-2}$), is mainly through decreasing of the income solar radiation SUR-SWd by ($-13\ W\ m^{-2}$). Clouds expression can be seen also in the increasing of the TOA-SWu ($11.9\ W\ m^{-2}$) and the decreasing of TOA-LWu ($-4.9\ W\ m^{-2}$). Clouds cover influences all of the afforested footprint area and small average spatial standard deviation (Fig. 33b).

Table. 6 Sahel's energy budget of the CON and AFFO scenarios.
Surface (SUR) and Top of Atmosphere (TOA) energy budget components over Sahel [16^0 E-40^0 W, 10^0-15^0 N], in JAS for the period 1998-2012, of CON-2d and AFFO-2d-S: radiative components: Up (u) and Down (d), Short and Long wave (SW and LW), and total net radiation (Rnet), Surface non-radiative components: sensible (H) and latent (LE) heat flux, Evapotranspiration (ET) and Surface Air Temperature (SAT). Cloud forcing also calculate with subtracting the full sky from the clear sky. Spatial standard deviation (std) was calculated for the given region. Units: Energy components [W m-2], ET [mm day^{-1}] and SAT with [^{0}C].

	CON				AFFO				AFFO-CON				cloud forcing
	full sky	std	clear sky	std	full sky	std	clear sky	std	full sky	std	clear sky	std	
SUR-SWd	289.4	11.6	324.6	2.3	274.2	11.3	322.3	2.2	-15.2	1.9	-2.3	0.2	-13.0
SUR-SWu	78.5	9.9	86.3	9.8	63.7	9.6	71.8	9.6	-14.8	1.1	-14.5	1.2	-0.3
SUR-LWd	358.9	12.4	352.2	10.6	361.3	12.3	352.5	10.4	2.4	0.8	0.3	0.6	2.1
SUR-LWu	454.2	14.7	454.1	14.7	446.3	14.5	446.1	14.5	-8.0	0.9	-8.0	0.9	0.0
SUR-Rnet	115.6	4.5	136.5	9.7	125.5	4.4	156.9	9.1	9.9	1.2	20.5	1.4	-10.5
TOA-SWd	413.9	0.0	413.9	0.0	413.9	0.0	413.9	0.0	0.0	0.0	0.0	0.0	0.0
TOA-SWu	126.5	6.3	100.2	8.7	125.6	6.4	87.4	8.4	-0.9	1.5	-12.8	1.0	11.9
TOA-LWu	272.3	7.6	291.0	8.6	263.6	7.4	287.2	8.3	-8.6	1.0	-3.8	0.4	-4.9
TOA-Rnet	15.1	5.9	22.7	8.5	24.6	5.9	39.3	7.9	9.5	1.4	16.6	1.2	-7.1
H	55.3	5.1			49.7	5.1			-5.6	0.9			
LE	64.7	13.9			81.6	13.7			16.9	2.5			
ET [mm/day]	2.2	0.5			2.8	0.5			0.6	0.1			
SAT [C]	24.7	0.4			23.4	0.4			-1.3	0.14			

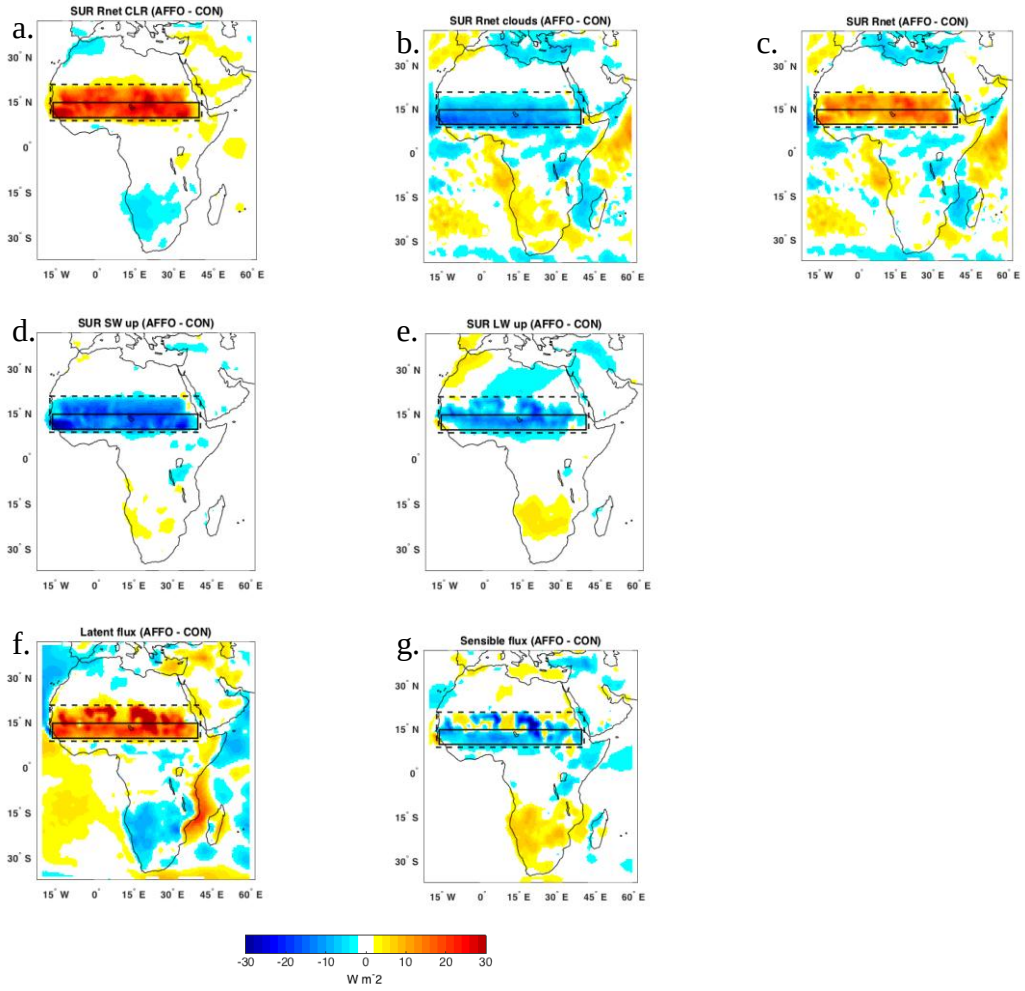

Figure 33. Regions examined in table 6 (CON-2d, AFFO-2d-S), bias of SUR-Rnet budget for (a) clear sky, (b) clouds forcing and (c) full sky. Bias of energy budget components: (d) SUR SWu, (e) SUR LWu, (f) LE and (g) H. Contour in unit of [W m-2]. Solid lines represent the afforested area [10^0-15^0 N, 16^0 W-40^0 E], and the dash lines cover the footprint area [10^0-20^0 N, 16^0 W-40^0 E].

7.2.2. Partitioning of the surface energy budget over North Australia

N-Aust energy budget results are not homogeneous, as results of increasing cloud cover and rain over the west part of the afforested area compare to the decreasing of precipitation over the east part (see Fig. 23c; Fig. 34). Two areas were analyzed: the Eastern (the resolute presents in the brackets) [17^0-22^0 S, 123^0 -128^0 E] and the Western part of the afforested area (the resolute presents in the round brackets) [17^0-22^0 S, 135^0 -140^0 E] (Table. 7a,b). The Western/Eastern part of the forest, resulted in increase/decreasing respectively of

the surface net radiation $(7.3)[-4.0]\ W\ m^{-2}$. This change over the western part it's mainly as a result of decrease of the incoming short wave radiation SUR-SWd ($-4.7\ W\ m^{-2}$) through clouds and decrease in surface albedo, which reflected through SUR-SWu ($-6.6\ W\ m^{-2}$). In the Eastern part increasing of outgoing short wave radiation SUR-SWu ($7.8\ W\ m^{-2}$) (Fig. 34a,d), relates to the declining of the surface wetness as a results in decreasing of precipitation of about -1.5 mm d^{-1} (Fig. 23c). In both areas the decrease in long wave upward radiation SUR-LWu $(-5.6)\ [-6.8]\ W\ m^{-2}$, as a result of the lower surface temperature SAT $(-0.5)\ [0.2]$ ℃. In the Eastern part the decreasing of SAT is a result of increasing the surface albedo, while in the western part its relate to the increasing of soil moisture, as results of the new forest. Increasing in soil moisture is expressed into higher ET, i.e. increase of the latent heat (LE) flux $(13.7)\ [4.9]\ W\ m^{-2}$ and a decrease in the sensible heat (H) flux $(-6.9)\ [-9.2]\ W\ m^{-2}$, which decreases the SAT over the forested area. The contribution of the clouds to SUR-Rnet $(-3.3)\ [-1.1]\ W\ m^{-2}$ is mainly through decreasing of the income solar radiation SUR-SWd by $(-4.0)\ [-2.3]\ W\ m^{-2}$. Increasing in clouds cover changes the atmosphere albedo, which influence on the increasing of TOA-SWu $(3.0)\ [9.0] W\ m^{-2}$ and the decreasing of TOA-LWu $(-3.1)\ [-3.0]\ W\ m^{-2}$. The total area average (Appendix D) is similar to the western part of the forest with moderate values.

Table. 7 N-Aust's energy budget of the CON and AFFO scenarios.
Surface (SUR) and Top of Atmosphere (TOA) energy budget components over a. Eastern part of N-Aust [17^0-22^0 S, 123^0 -128^0 E] and b. Western part of N-Aust [17^0-22^0 S, 135^0 -140^0 E], in JFM for the period 1998-2012, of CON-2d and AFFO-2d-NA: radiative components: Up (u) and Down (d), Short and Long wave (SW and LW), and total net radiation (Rnet), Surface non-radiative components: sensible (H) and latent (LE) heat flux, Evapotranspiration (ET) and Surface Air Temperature (SAT). Cloud forcing also calculate with subtracting the full sky from the clear sky. Spatial standard deviation (std) was calculated for the given region. Units: Energy components [W m-2], ET [mm day^{-1}] and SAT with [^{0}C].

a.

JFM	CON				AFFO				AFFO-CON				cloud forcing
	full sky	std	clear sky	std	full sky	std	clear sky	std	full sky	std	clear sky	std	
SUR-SWd	268.1	12.0	298.4	2.3	265.9	11.3	298.7	2.2	-2.3	2.3	0.3	0.1	-2.5
SUR-SWu	57.8	10.0	63.8	9.9	65.5	10.0	72.5	9.9	7.8	0.5	8.7	0.6	-1.0
SUR-LWd	350.1	12.4	343.6	10.6	349.4	12.4	342.3	10.7	-0.8	0.6	-1.3	0.4	0.5
SUR-LWu	442.8	14.5	442.6	14.5	436.0	14.5	435.9	14.5	-6.8	0.5	-6.8	0.5	0.0
SUR-Rnet	117.7	4.7	135.6	9.8	113.7	4.8	132.6	9.6	-4.0	1.3	-2.9	0.6	-1.1
TOA-SWd	385.0	0.0	385.0	0.0	385.0	0.0	385.0	0.0	0.0	0.0	0.0	0.0	0.0
TOA-SWu	102.9	6.7	79.7	8.7	111.9	6.5	87.4	8.7	9.0	2.0	7.7	0.5	1.3
TOA-LWu	272.4	7.6	285.3	8.4	269.4	7.5	282.9	8.4	-3.0	0.9	-2.4	0.2	-0.6
TOA-Rnet	9.8	5.9	20.0	8.4	3.8	6.2	14.8	8.4	-6.0	1.6	-5.2	0.5	-0.8
H	63.3	5.2			54.1	5.1			-9.2	0.8			
LE	61.4	13.9			66.4	13.7			4.9	1.9			
ET (mm/day)	2.1	0.5			2.3	0.5			0.2	0.1			
SAT [C]	27.5	0.4			27.3	0.4			-0.2	0.14			

b.

JFM	CON				AFFO				AFFO-CON				cloud forcing
	full sky	std	clear sky	std	full sky	std	clear sky	std	full sky	std	clear sky	std	
SUR-SWd	273.3	12.0	297.2	2.3	268.6	11.3	296.5	2.2	-4.7	2.3	-0.7	0.1	-4.0
SUR-SWu	56.7	10.0	61.3	9.9	50.1	10.0	54.6	9.9	-6.6	0.5	-6.7	0.6	0.1
SUR-LWd	355.8	12.4	349.9	10.6	355.5	12.4	348.9	10.7	-0.2	0.6	-1.0	0.4	0.8
SUR-LWu	450.6	14.5	450.5	14.5	445.0	14.5	444.9	14.5	-5.6	0.5	-5.6	0.5	0.8
SUR-Rnet	121.7	4.7	135.3	9.8	129.0	4.8	145.9	9.6	7.3	1.3	10.6	0.6	-3.3
TOA-SWd	385.0	0.0	385.0	0.0	385.0	0.0	385.0	0.0	0.0	0.0	0.0	0.0	0.0
TOA-SWu	96.2	6.7	77.7	8.7	94.1	6.5	71.8	8.7	-2.1	2.0	-5.9	0.5	3.8
TOA-LWu	279.1	7.6	288.3	8.4	275.9	7.5	286.5	8.4	-3.2	0.9	-1.8	0.2	-1.4
TOA-Rnet	9.7	5.9	19.0	8.4	15.0	6.2	26.7	8.4	5.3	1.6	7.7	0.5	-2.4
H	71.7	5.2	0.0	0.0	64.7	5.1	0.0	0.0	-6.9	0.8	0.0	0.0	
LE	55.6	13.9	0.0	0.0	69.3	13.7	0.0	0.0	13.7	1.9	0.0	0.0	
ET (mm/day)	1.9	0.5	0.0	0.0	2.4	0.5	0.0	0.0	0.5	0.1	0.0	0.0	
SAT [C]	28.1	0.4			27.6	0.4			-0.5	0.14			

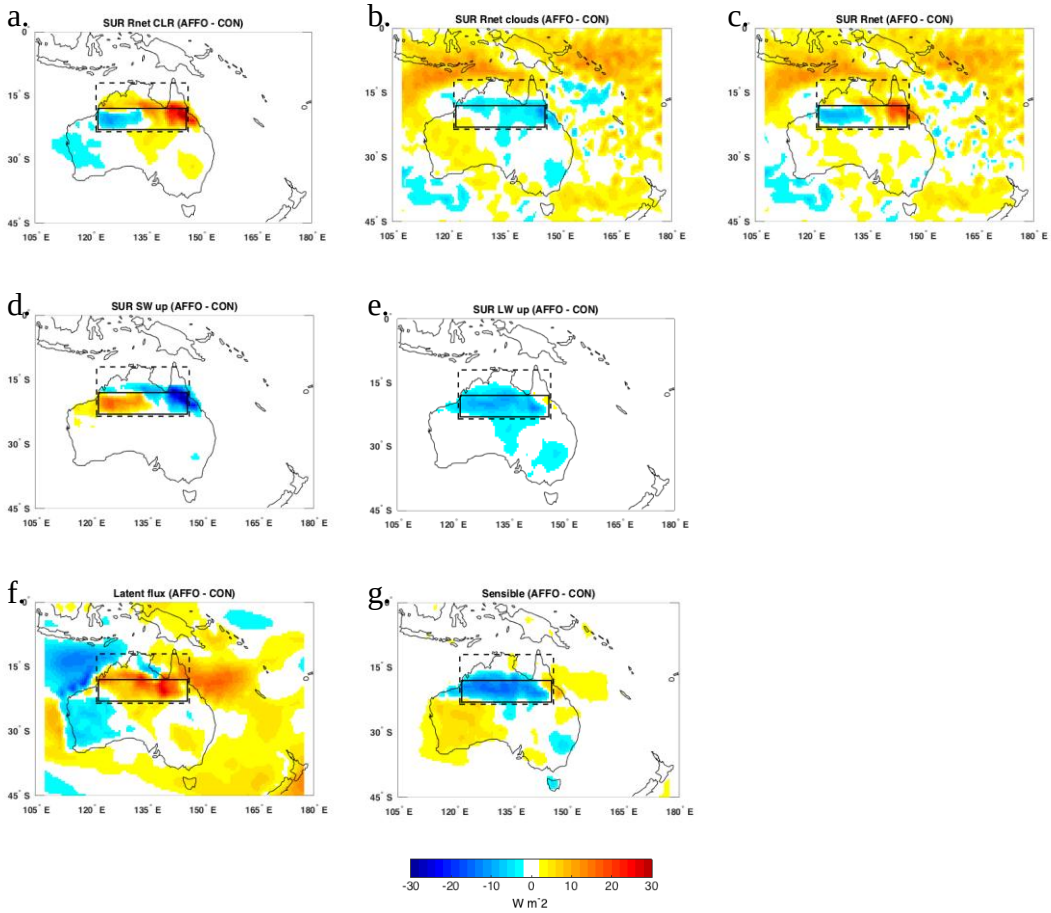

Figure 34. Regions examined in table D.1 (Appendix D) (CON-2d, AFFO-2d-NA), bias of SUR-Rnet budget for (a) clear sky, (b) clouds forcing and (c) full sky. Bias of energy budget components: (d) SUR SWu, (e) SUR LWu, (f) LE and (g) H. Contour in unit of [W m-2]. Solid lines represent the afforested area [17^0-22^0 S, 122^0 -146^0 E], and the dash lines cover the footprint area [12^0-22^0 S, 122^0 -146^0 E].

7.3. Summary

The results of Afforestation in the semi-arid Sahel (a) and North Australia (N-Aust; b) for July-August-September and January-February-March respectively, showed increase of the surface net radiation (a. $9.9 \pm 1.2\ W\ m^{-2}$; b. $2.6 \pm 1.3\ W\ m^{-2}$), due both albedo effect and changes in the long-waver radiation balance: Increase in downward (a. $2.4 \pm 0.8\ W\ m^{-2}$; b. $\sim 0 \pm 0.6\ W\ m^{-2}$) and decrease upward (a. $8 \pm 0.9\ W\ m^{-2}$; b. $4.9 \pm 0.5\ W\ m^{-2}$) long wave radiation fluxes, associated with the lower surface temperature. Changes in short-wave radiation were due to decrease in surface albedo (a. $14.8 \pm 1.1\ W\ m^{-2}$; b. $1.2 \pm 0.5\ W\ m^{-2}$), and

in incoming short wave radiation (a. $15.2 \pm 1.9\ W\ m^{-2}$; b. $3.4 \pm 2.3\ W\ m^{-2}$), which essentially balanced out. Increasing soil moisture was expressed in large increase in latent heat (LE) flux ($16.9 \pm 2.5\ W\ m^{-2}$; b. $8.7 \pm 1.9\ W\ m^{-2}$), and a small decrease in the sensible heat (H) flux (a. $5.6 \pm 0.9\ W\ m^{-2}$; b. $6.1 \pm 0.8\ W\ m^{-2}$), leading to lower surface temperature (a. 1.3 ± 0.14 ℃; b. 0.9 ± 0.1 ℃). The primary changes in surface energy budget were associated with a sequence of changes in the local atmospheric dynamics, which results in increasing summer precipitation over the forested area and over the footprint area. In Sahel the energy components results were distributed horizontally, while in N-Aust changes in the wind pattern, leads into less cloud cover in the east part and more in the west part of the forest, influences the horizontal energy partition of energy.

8. Further Analyses of Processes Associated with Forestation of the Sahel

8.1 Introduction

As described above, land cover change over semi-arid regions as the Sahel and North-Australia leads to changes in surface temperature and precipitation. In addition to the core results of this work, more several effects are observed as a result of afforestation, which will be described hereinafter. The effects are: a. Sources of humidity in the terrestrial water cycle over the afforested Sahel. b. Mechanisms of vertical stability change over Sahel (local scale). c. Ocean influence on precipitation due to Sahel afforestation is examined (global scale). This chapter will introduce these three topics and the dynamic between each phenomenon with precipitation increase due to afforestation.

8.2 Results

8.2.1. Sources of humidity in the terrestrial water cycle over the afforested Sahel

Changing the land cover from low-level shrubs to forest over the Sahel shifts the rain belt farther north, increasing the precipitation over the Sahel and the south part of the Sahara desert (Fig. 12c). The level of the moisture penetration resulting from AEJ's intensity and the existence of the forest, determined by the role of external vs. internal sources of moisture and water cycling in the rainfall regime. At the wet season, external moisture availability and synoptic forcing influence Western Africa, while the inland is influenced by the internal source of ET flux. The index of water recycling was used as a tool to explicitly investigate the sources and pathways of humidity in the terrestrial water cycle over the Sahel between the two simulations CON and AFFO.

Water Recycling (WR): refers to the contribution of local ET fluxes to precipitation. It can be used, as an indication of the degree of controlling the local processes on precipitation dynamics in a region: how much of the precipitation amount falling on a region is actually water originating from the surface in the same region by evapotranspiration (Fig. 35).

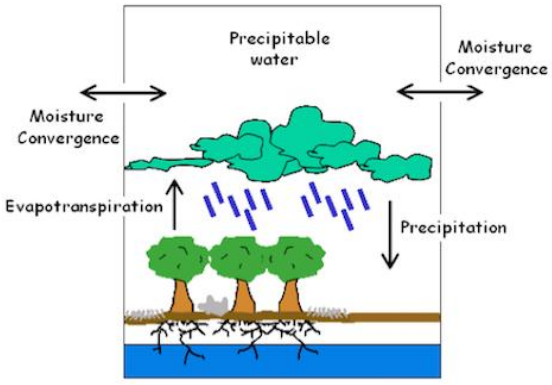

Figure 35. Schematic illustration of the driven component in calculating Water Recycling index

The flowing analytical methods of the recycling ration is used:

(12) $WR = \frac{P_e}{P_e + P_{mc}} = \frac{ET}{ET + MC}$

Were *ET* refer to the evaporation, and *MC* refer to moisture convergence, assume that the ratio between the amount of precipitation originating from *ET* (P_e) and from *MC* (P_{mc}) is the same as the ratio between *ET* and *MC* themselves:

(13) $\frac{P_e}{P_{mc}} = \frac{P_{mc}}{MC}$

(*Schar et al, 1999; Trenberth, 1999*).

MC is calculating as vertical integrated moisture flux divergences

(14) $MC = -\frac{1}{g} \nabla \cdot \int_{P_{sfc}}^{P_0} V_h(P) Q(P) dP$

(15) $q \nabla \cdot V_h = q \left(\frac{\partial u}{\partial x} + \frac{\partial v}{\partial y} \right)$

Were u, v represent the two dimensional wind components, and q or Q is the specific humidity; P_{sfc} is the surface pressure, P_0 is the upper level pressure, g is the gravitational accelerate, $q \nabla \cdot V_h$ is the horizontal MFC. Were MC is the net balance of moisture flux in the grid column.

The results show that in general ET is lower over the desert area (< 15^0 N), but as a result of afforestation it's increased dramatically over the Sahel up to the south Sahara desert (20^0 N) (Fig. 36c). The MC bias between AFFO to CON reveals a pattern of increasing convergence (negative MC) over the south border (~10^0 N) and decreasing divergence at the north border (~20^0 N) of the footprint area. Increasing divergence accurse at the Gulf of Guinean coast (~5^0N) (positive MC) and over the middle of the afforested area (~12.5^0N) the

convergence decreased (positive MC) (Fig. 36f and Fig. 37). Over all WR, have higher values at the Sahel region in CON and AFFO, as results of increasing ET accompanied with higher MC.

This result can be interpreted as self-sustainable system (Fig. 36i), were water is recharge to the atmosphere through ET, supported with convergence process, as can be seen over the West part of the Sahel. As consequence the forest the system is not relaying on external water alone and also uses recycled water coming from its own ET to increase precipitation. Increase in convergence in the south-West of the afforested area and north-West of the foot print (Fig 36i), together with its decreasing in between, suggests a local atmospheric instability which will be explained and discussed in the following section.

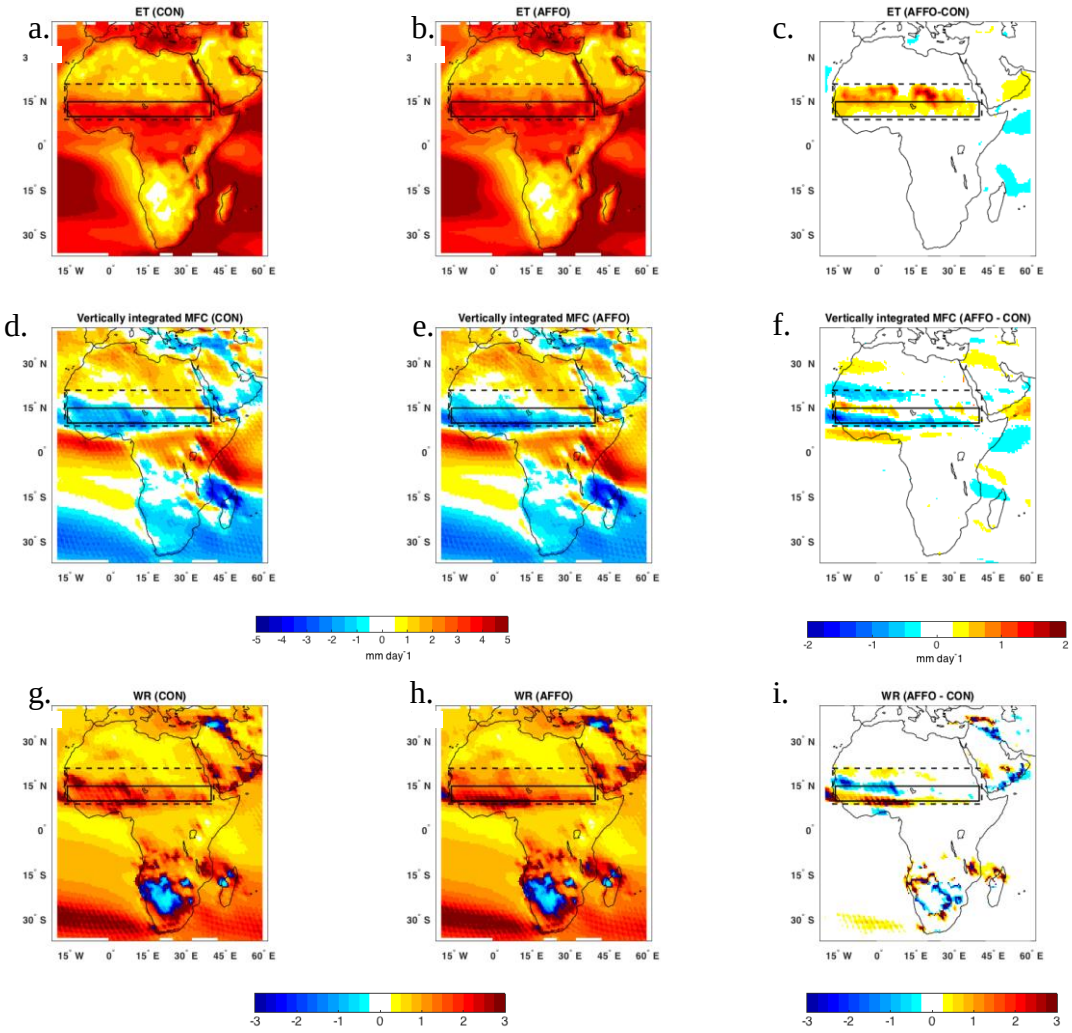

Figure 36. Model simulated seasonal mean (JAS) for the period 1998 -2012, of evapotranspiration (ET), (a) CON-2d, (b) AFFO-2d-S and (c) AFFFO-2d-S – CON-2d. Vertically Moist Flux Convergence (MFC) integrated over the depth of the atmosphere from 1000 mb to 0 mb, convergence and divergence represented as positive and negative values respectively (d) to (f) Units in [mm day^{-1}] and Water Recycle (WR), (g) to (i) unit less, Solid lines represent the afforested area [10^0-15^0 N, 16^0 W-40^0 E], and the dash lines cover the footprint area [10^0-20^0 N, 16^0 W-40^0 E].

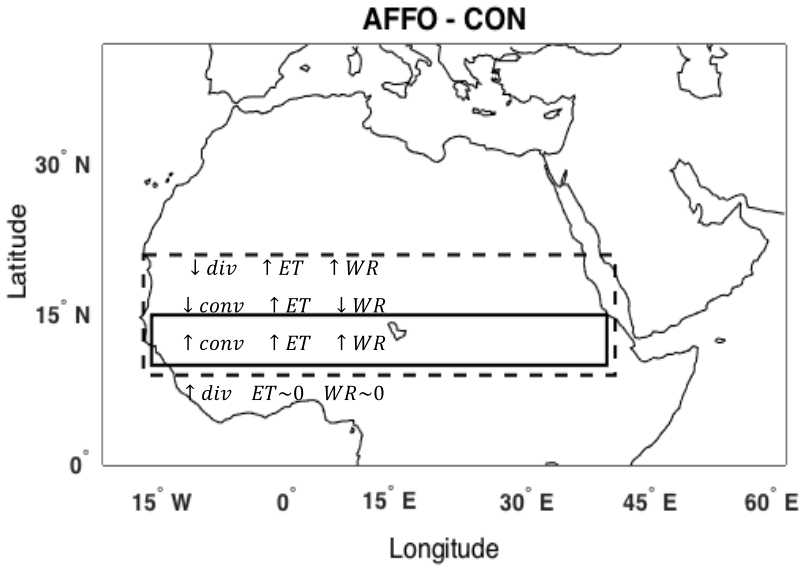

Figure 37. Changes in the atmosphere circulation as a result of afforestation: divergence (div), convergence (conv), evaporation (ET) and water recycling (WR). Signs of upward and downward arrow indicates increasing and decreasing respectively. Solid lines represent the afforested area [10^0-15^0 N, 16^0 W-40^0 E], and the dash lines cover the footprint area [10^0-20^0 N, 16^0 W-40^0 E].

8.2.2. Local mechanisms of vertical stability change over Sahel

In order to better understand the new pattern of monsoon circulation shown above, an analysis of a local mechanism is required. Although precipitation increase is almost unified all over the afforested area (Figure 12.c), analyzing the changes in MFC (Fig. 16c,f) revels a dual model; when increasing, convergence occurs roughly at 10^0 N and 20^0 N while decreasing at 15^0 N and increasing divergence at 5^0 N. As a result, this mode influences the WR (Fig. 36i). Changes in convergence process, can be examined by the moist static energy (MSE) budget, for understanding the contributions of large-scale temperature and moist anomalies to differences in convections. The theory was developed by *Neelin and Held (1987)* and applied to land regions by *Zeng and Neelin (1999), Chou and Neelin (2003), Philippon and Fontaine (2002), Patricola and Cook (2007),* and others.

The total atmospheric energy (E_v) is calculated from the sum of the potential energy ($\Phi = gZ$), internal energy (C_vT) and latent energy (L_vq) are the respective sensible and latent heat flux energy components, and kinetic energy $[\frac{1}{2}(u^2 + v^2)]$.

(16) $E_v = \Phi + C_vT + L_vq + \frac{1}{2}(u^2 + v^2)$

C_v correspond to the latent heat of vaporization and T is temperature, g is gravitational acceleration, Z is geopotential height, q specific humidity and L correspond to the latent heat of vaporization and u, v are wind velocity fields. In order to work in a pressure coordinate system, the internal energy (E_p) calculating by substituting C_v with C_p the specific heat capacity of air at constant pressure. If we neglect the kinetic energy, which is a very small fraction of the total energy in the atmosphere, the MSE equation takes the following form:

(17) $m = gZ + C_pT + Lq$

All the components related to the energy content per unit mass [KJ Kg^{-1}]. To illustrate the changes of MSE we consider $\tilde{\omega}$ (omega the vertical velocity in pressure coordinate in [Pa s^{-}]) that was calculate using the equation of the continuity in flux term for pressure coordinate to calculate the horizontal divergence, assuming the vertical velocity at the surface is zero:

(18) $\frac{\partial w}{\partial p} = -\left(\frac{\partial u}{\partial x} + \frac{\partial u}{\partial x}\right) = -D_h\ [s^{-}]$

(19) $\omega(p_2) = \omega(p_1) - \int_{p_1}^{p_2} D_h dp$

Were u, v and w represent the three dimensional wind components, D_h is the horizontal divergence, and ω is omega at different pressure levels p. Negative (positive) values of $\tilde{\omega}$ correspond to upward (downward) motion.

In the CON-2d scenario simulated MSE budget averaged over 10^0-15^0 N (Fig. 38a), the temperature term is the largest contributor to the MSE throughout the troposphere, and the geopotential energy term becomes increasingly large above 700mb. The latent heat term is relatively small (near zero above 500mb).

When dividing the footprint area into two regions, one over the afforested 10^0 -15^0 N and the other is at south Sahara desert 15^0-20^0 N, it can be observed that over 10^0 -15^0 N there is negative low-level MSE anomalies, which stabilize the column, mainly as a results of lower temperature term C_pT, despite positive humidity term Lq anomalies (Fig. 38b). On the other hand, positive low-level MSE anomalies are simulated over 15^0-20^0 N. The anomalies

in C_pT and Lq are higher than over the Sahel, were at the same time, the pattern of negative temperature and positive humidity anomalies occurs. This analysis indicates that although there is a negative low-level temperature anomalies, MSE increases as a result of the higher positive moisture anomalies at the low-level. In both cases the geopotential energy anomalies are negligible (not shown).

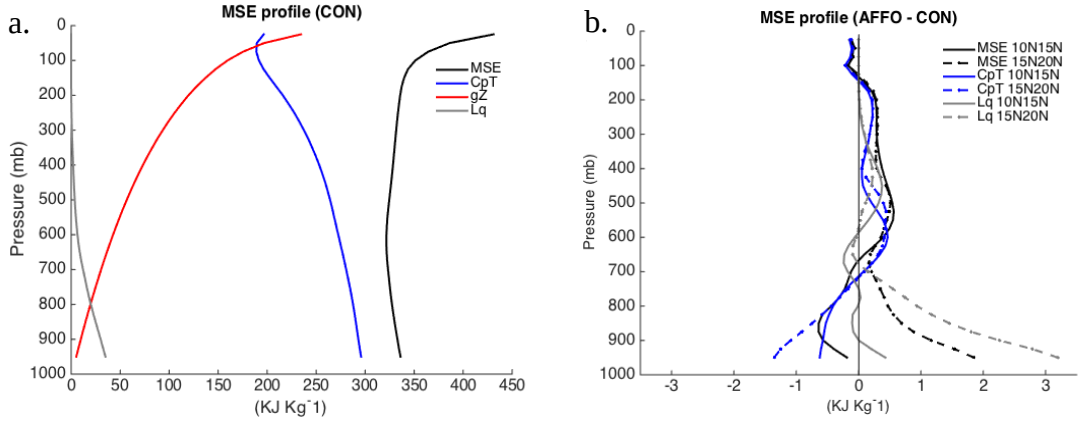

Figure 38. The average MSE analysis for JAS months: a. total MSE (black line), temperature (blue line), geopotential energy (green line), and moisture term (gray line) for the (a) CON-2d simulation over 10^0-15^0W, 10^0-15^0N and (b) AFFO-2d-S – CON-2d anomaly of total MSE (back line), temperature term (blue line) and moisture term (gray line) over 10^0-15^0N (solid line) and 15^0-20^0N (dash line).

To illustrate this latter point, MSE and $\widetilde{\omega}$ (*10^4) were used (Fig. 39), presenting the mean JAS values of the upward and downward motion corresponds to atmosphere energetic state. In CON simulation, strong vertical ascents take place primarily over the south Sahara (15^0- 20^0N), accompanied with positive gradient of MSE (Fig. 39c). At AFFO simulation the results show the displacement and increasing positive MSE to the north, which pulls the maximum upward motion with it (Fig. 39e). From the result we can deduce that increasing MFC over the north edge of the footprint area (section 5.2.2.2.), relates to an increasing atmospheric energy on the local scale, resulting by increasing humidity and to atmosphere dynamic changes in the form of weakened AEJ at lower level (Fig. 15c). The increasing of MFC over the south edge (Fig. 16c,f) of the footprint area, doesn't relate to atmosphere energy state, but only to the weakened AEJ, which reduce the divergence of moister out from the region.

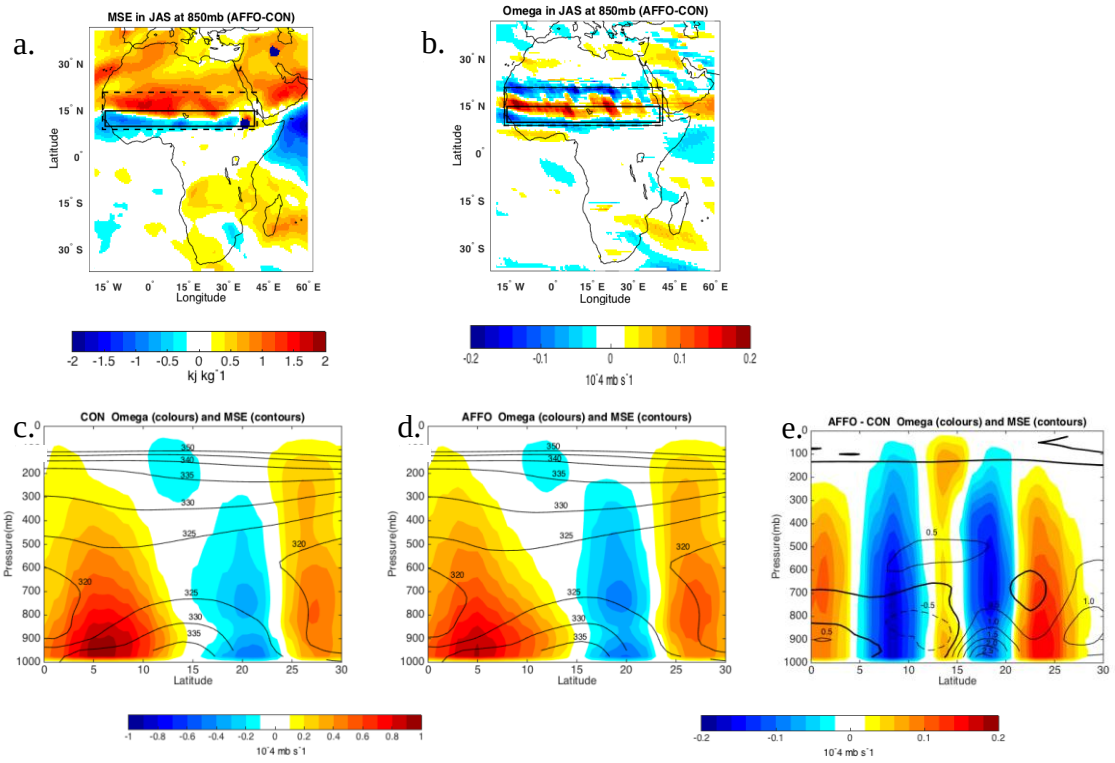

Figure 39. Model simulated seasonal mean (JAS) for the period 1998-2012, of (a) MSE [KJ/Kg^{-1}] anomalies at 850mb, (b) Omega [10^{-4} mb s^{-1}] at 850mb. Solid lines represent the afforested area [10^0-15^0 N, 16^0 W-40^0 E], and the dash lines cover the footprint area [10^0-20^0 N, 16^0 W-40^0 E]. Zonal cross-section (10^0-15^0W) averaged meridional MSE and Omega and the zonally averaged vertical motion as represented by Omega, Negative (positive) values correspond to upward (downward) motion. (c) CON-2d, (d) AFFO-2d-S and (e) AFFO-2d-S – CON-2d.

8.2.3. Ocean influence on precipitation due to Sahel afforestation

During the second half of the twentieth century, the semiarid African Sahel zone was influenced by wide climate variation, irregular rainfall between 200-600 mm with succession of wet (1950 - 1968) dry (1968 - 1993) and irregular (1993 - 2013) year-to-year rainfall anomalies (*Ackermann et al. 2014*) as shown in (Fig. 40, from *NOAA NCDC Global Historical Climatology Network data*).

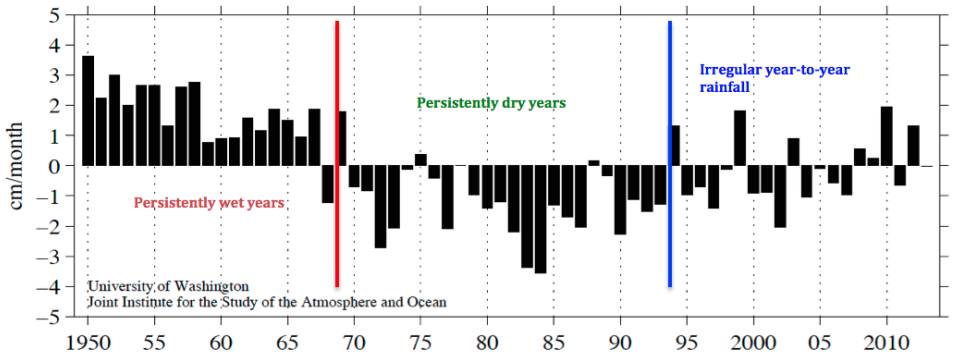

Figure 40. Rainfall variation in the Sahel: June through October averages over 20^0-10^0 N, 20^0 W-10^0 E. Positive values indicate years with rainfall levels exceeding the average of the period 1950-2013, and negative values indicate years with rainfall levels lower than the average for that period.

Several theories on this phenomenon were studied, suggesting two main hypotheses; a. Anthropogenic related reasons, can affect the environment and climate through changing the land cover such as land use change (e.g.- over-grazing, increase in agriculture use), which leads to increase the surface albedo, cools the surface, leading to suppression of convective clouds, and decrease in vegetation cover which in turn increase the albedo again (*Charney, 1975*; *Xue, Y. and J. Shukla, 1993*) and b. Global Sea surface temperature (SST) variation, suggesting that a higher water temperature around West Africa, are enhancing the formation of deep convection clouds over the ocean, rather than over the inland (*Giannini et al. 2003*). The influence of SST from different ocean basins founds affect the interannual and interdecadel Sahel's time scale precipitation (*Folland et al. 1986, Giannini et al. 2003*). Combining both hypotheses, *Zeng, 2003* suggested that the SST change, natural vegetation processes, and land use change act in synergy, to produce the drought in the Sahel (Fig. 41, from *Zeng, N. 2003*).

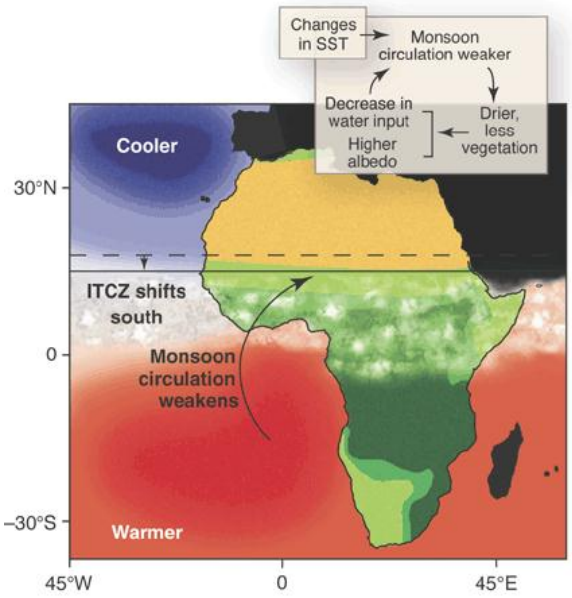

Figure 41. Diagram of the positive feedback causing the Sahel drought: warmer ocean aside of West Africa, reduced the strength of African monsoon, drive the positive feedback over the land due to vegetation and cover land change.

Although land surface process might play a role, studies over West Africa Monsoon (WAM) showed that the oceanic forcing is the dominant driver of the decadal monsoon variability (*Zeng et al, 1999; Biasutti et al, 2008*). The El Nino-Southern Oscillation (ENSO) phenomena (*Janicot et al, 2001*), the Atlantic Nino (*Giannini et al, 2003*) and the Mediterranean Sea *(Rodriguez-Fonseca et al, 2011)* have been identified to have an important impact on the WAM system. *Rodriguez-Fonseca et al (2011), Lu, J. and T. L. Delworth (2005)* and others, studies the decadal Sahelian rainfall variability changes, founds that the Atlantic and Pacific multidecadal oscillation effect the background state of the ocean, which can alert the teleconnection between the different interannual SST patterns and WAM. With this context we would like to examine the SST forced signals on the Sahel region, under afforestation scenario. Simulation results already suggested a consistence with the increasing precipitation (Fig. 12c); therefore the next step is to understand what is the ocean's teleconnection role in this result? Does the increasing precipitation is a self sustained only through the land-atmosphere interaction or there are major teleconnection influences on the increasing/decreasing rainfall over the Sahel during summertime?

The Maximum Covariance Analysis (MCA) procedure (also refer as Singular Value Decomposition - SVD) were used to derive a statistical atmosphere relating the precipitation

over the Sahel to the SST (*Rodriguez-Fonseca and Manuel. 2002; Rodriguez-Fonseca et al. 2011*; *Giannini et al. 2003)*. The MCA is well discussed in Bretherton et al. (1992) and Wallace et al. (1992), it can be considered as a generalization of the Principal Component Analysis (PCA), and indeed reduces to it when two fields are identical. The MCA is usually applied to two data fields, in order to identify the pairs of coupled spatial patterns that explain the largest covariance between the two variables. The technique yields two sets of singular vectors and a set of one singular value associated with each pair of vectors. Each pair of singular vectors described a fraction of the square covariance between the two variables, and the Square Covariance Fraction (SCF) accounted for by the k^{th} pair of singular vectors is proportional to the square of the k^{th} singular value. The expansion coefficient for each variable is computed by projecting the respective data field onto the k^{th} singular vector. Expansion coefficient also refers as the Principal Component (PC), which represents the time series of the pattern. The correlation value (r^2) between the k^{th} PC's of the two variables indicates how strong related the coupled patterns are. Using the PC's from the MCA, we generated a regression map between the grid point anomalies of a given field and its k^{th} PC. The map indicates the geographical location of the co-varying part between the field and its k^{th} PC.

The MCA procedure was applied for 17 years (1998-2012) mean Jun to September (JJAS) of bias the AFFO – CON. Precipitation was calculated for the area of North Africa (12^0 W, 42^0 E – 32^0 S, 62^0 N), and the prescribed SST was prepared for global scale (50^0 S, 50^0 N), using a prescribed NCEP reanalysis database, which was the same in both simulations.

The Math behind the MCA: consider the two data matrices SST *(S)* and precipitation *(P)*, which constructed by the bias of AFFO – CON simulations. Sizes matrices of *S* and *P* is $M \times N$ and $L \times N$ respectively, were M and L are structure of space dimensions and N is the shared sampling dimension. The time mean (average over sample *N*) from *S* and *P* is removing and the $M \times L$ covariance matrix is produce:

(20) $\frac{1}{N} SP^T = C_{SP}$

The cross-covariance matrix C_{SP} can be decompose with SVD procedure into:

(21) $C_{SP} = ULV^T$

Were *U* is singular vector (eigenvector) of one filed (*S*), *V* is singular vector of the seconded field (*P*) and *L* is singular value of the cross-covariance matrix C_{SP}. The fraction of covariance explained by each mode, is given by the percentage format of Square Covariance Fraction (SFC):

(22) $SFC(i) = L_i^2 / \sum_{j=1}^{q} L_j^2 * 100$

The construction of the expansion coefficient that refers as PC, of the SST field (PC_S) and precipitation field (PC_P) are:

(23) $PC_S = SU^T$

(24) $PC_P = PV^T$

Then, the fraction of the variance (Var) of a given *P* mode, explained by the ratio of the variance of the appropriate $PC_{P(\square)}$ to the total variance of the P vector, obtained by summing over all principal components,

(25) $Var(P_i) = var(PC_{P(i)}) / \sum_{j=1}^{q} var\ (PC_{P(j)})$

The same was done for $Var(SST_i)$,

(26) $Var(SST_i) = var(PC_{S(i)}) / \sum_{j=1}^{q} var\ (PC_{S(j)})$

The first few SST singular vector contain most of the variance, therefore the first few SST mode patterns will be analysis.

The result show a leading mode (33.6 % explained covariance, see Table 8) coincides with the region in which the variability of summer monsoon precipitation is heavily influences by the insolation that increases as month forward from Jun to September. This anomalies associated with SST changes between the hemispheres, creates the "Inter-hemispheric gradient" mode *(Folland et al, 1986)*. This pattern implies that the increases precipitation over footprint area of the afforestation is associated with the summertime where sun Insolation is increases over the north hemisphere (positive correlation) and decrease at the south hemisphere (negative correlation) (Fig. 42). The second leading mode (16.1% explain covariance), represent the "Pacific Mode" were the Sahelian and Guinean Coast rainfall are contrast with each other. Previous work showed that the Sahelian rainfall reduction with a warming over the tropical Pacific *(Joly et al, 2007; Giannini et al, 2003; among others)*. In the monsoon pre-onset, a warming over the equatorial Pacific influences the rainfall of the Gulf of Guinea through anomalous subsidence over the equatorial Atlantic.

In the peak and withdrawal of the monsoon, reduces the Sahel rainfall through equatorial Rossby waves from the maritime continent *(Mohino et al, 2011)* by inducing anomalous subsidence over the Sahel. During ENSO event, the development phase of an El Nino/L Nina event were warmer/cooler equatorial Pacific its influence on the decreasing/increasing rainfall over the Sahel. The observed timing of the ENSO Sahelian relationship is not simulate well in OLAM as well with the Coupled-Ocean General Circulation Model (IPCC-AR4) *(Joly and Voldoire, 2009).*

The third leading mode (8.0 % explain covariance), represent the "Atlantic Mode", were warmer tropical Atlantic, decreases the land-ocean temperature, shifts the maximum convection to the south, led to the decrease of Sahelian convergence. This in turn decreases Sahelian precipitation while increase of rainfall in the Golf of Guinean coast (*Giannini et al, 2003; Rodriguez-Fonseca et al, 2011; Zeng et al, 1999).*

Regarding the statistics of the leading MCA modes (Table 8, Fig. 43), all the modes are with good correlation (r^2) between PC's, the Var(P) increase with higher modes while the opposite occur with Vap(SST). The result of high correlation (r^2 0.5) and small variance of the precipitation (Var(P) 7.5%) at the first mode, supports the persistence of the increasing precipitation in the simulations results, over the Sahel domain (Fig. 12) during the monsoon. Therefore it can be argued that there is a stronger effect of afforestation on the regional atmospheric circulation, which led to the increasing rainfall over the region but it can be moderate due to different SST mode of ocean's basins such as Atlantic, Pacific and other.

Table. 8 The results of the first three SVD's vector are given in the columns, and refer as mode. The entries are all multiplied by 100, expect for correlation (r^2). The SFC raw contains the percentage of the covariance between SST and precipitation parameters explained by each SVD vector [using the singular values, Eq, (21)]. The row marked Var (P) and Var (SST), is the percentage of the variance of the SST and precipitation fields respectively vector explained by each SVD vector [using Eq. (24 - 25)].

AFFO - CON	Mode 1	Mode 2	Mode 3
SFC	33.6%	16.1%	8.0%
r^2	0.5	0.6	0.62
Var (P)	7.5%	17.2%	23.1%
Var (SST)	21%	12.5%	15.3%

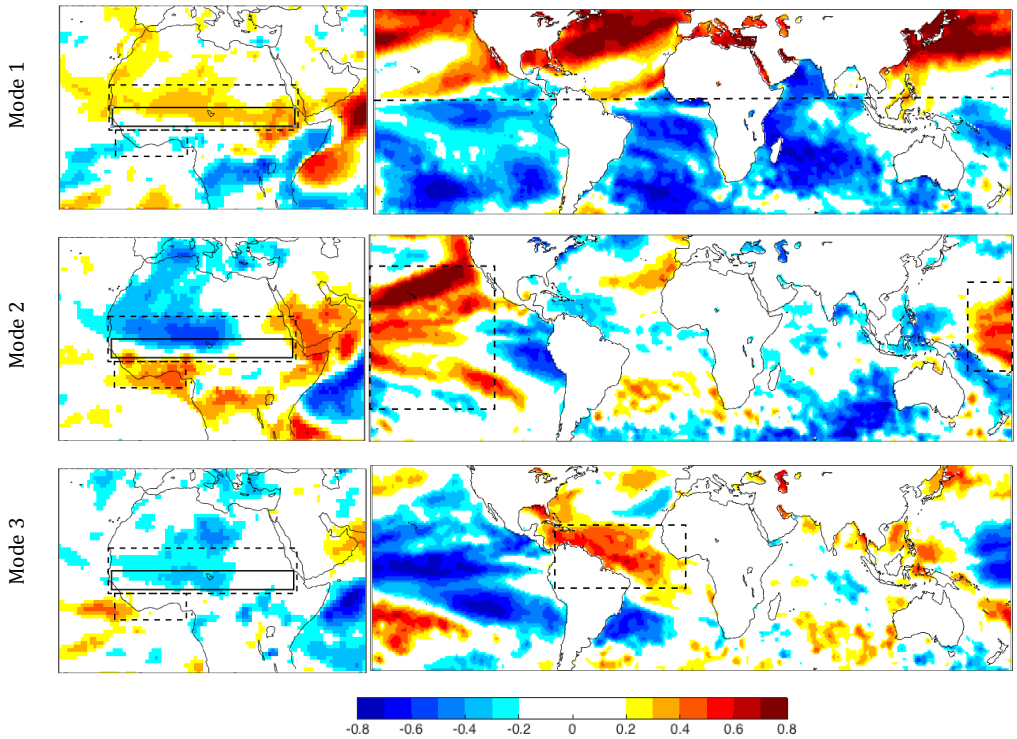

Figure 42. Leading mode derived from MCA analysis of monthly Jun to September (JJAS) precipitation and SSTs anomalies of AFFO-2d-S – CON-2d simulations, during 1998-2012: Mode 1, first mode of precipitation (left) of SST (right), the same for the second mode and the third mode. In the precipitation modes the dash line represents the areas of footprint (south Sahara) and the Gulf of Guinean coast, solid lines represent the afforested area (Sahel). In the SST modes dash lines represent the associated ocean basin area to the precipitation pattern over North Africa.

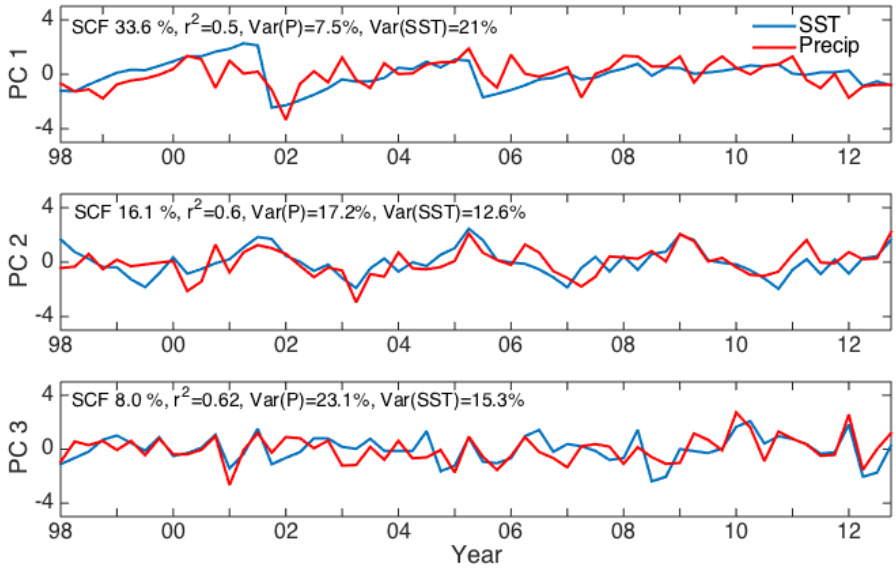

Figure 43. The nondimentional normalized SST and precipitation principal component for the first three SST and precipitation modes corresponding to Figure 42.

8.3. Summary

Afforestation over the Sahel led to colder surface, which reduced the atmospheric instability (MSE) and as result, reduced the vertical motions (Omega). Nevertheless weakening of the AEJ enabled the evolution of the convergence over the afforested area. The increase in moisture extended over the drier north edge of the forest band, which increased the MSE and the vertical motion that led to the enhancement of MFC and WR, beyond the afforested band. Additional analysis of MCA with global ocean SST data showed that the main contribution to increasing precipitation over the afforestation region was the penetration of monsoon rain toward the Sahel (SFC 33.6%), overcoming weaker effects of warmer pacific and equatorial Atlantic oceans regions that have a reduction effect on the Sahel precipitation.

9. General Discussions and Summary

9.1. Main findings and central conclusions

The 17 years simulation of Afforestation in the semi-arid Sahel (a) and North Australia (N-Aust; b) for July-August-September and January-February-March respectively, showed increase of the surface net radiation (a. $9.9 \pm 1.2\ W\ m^{-2}$; b. $2.6 \pm 1.3\ W\ m^{-2}$), due to both albedo effect and the changes in the longwave radiation balance: Increase in downward (a. $2.4 \pm 0.8\ W\ m^{-2}$; b. $\sim 0 \pm 0.6\ W\ m^{-2}$) and decrease upward (a. $8 \pm 0.9\ W\ m^{-2}$; b. $4.9 \pm 0.5\ W\ m^{-2}$) longwave radiation fluxes, associated with the lower surface temperature. Changes in short-wave radiation were due to decrease in surface albedo (a. $14.8 \pm 1.1\ W\ m^{-2}$; b. $1.2 \pm 0.5\ W\ m^{-2}$), and in incoming short wave radiation (a. $-15.2 \pm 1.9\ W\ m^{-2}$; b. $3.4 \pm 2.3\ W\ m^{-2}$), which essentially balanced out. Increasing soil moisture was expressed in large increase in latent heat (LE) flux ($16.9 \pm 2.5\ W\ m^{-2}$; b. $8.7 \pm 1.9\ W\ m^{-2}$), and a small decrease in the sensible heat (H) flux (a. $5.6 \pm 0.9\ W\ m^{-2}$; b. $6.1 \pm 0.8\ W\ m^{-2}$), leading to lower surface temperature (a. 1.3 ± 0.14 ℃; b. 0.9 ± 0.1 ℃). The primary changes in surface energy budget were associated with a sequence of changes in the local atmospheric dynamics: Decreasing the meridional surface temperature gradient over the forested area, and increasing it over the drier area north of the forestation band; weakening the local low-level jet core (a. $1\ m\ s^{-1}$, b. $2\ m\ s^{-1}$) and its displacement toward the drier edge of the forested band; deeper penetration and increasing convergence of westerlies winds inland; displacement of the maximum summer precipitation over the forested area and its drier edge (a. $0.8 \pm 0.2\ mm\ d^{-2}$ ($\sim 75\ mm \pm 18mm$), b. $0.4 \pm 0.2\ mm\ d^{-2}$ ($\sim 20\ mm \pm 18mm$). In the Sahel, the forest led to colder surface, which reduced the atmospheric instability (MSE) and as result, reduced the vertical motions (Omega). Nevertheless weakening of the AEJ enabled the evolution of the convergence over the afforested area. The increase in moisture extended over the drier north edge of the forest band, which increased the MSE and the vertical motion that led to the enhancement of MFC and WR, beyond the afforested band. Additional analysis of Maximum Covariance Analysis (MCA) with global ocean SST data showed that the main contribution to increasing precipitation over the forestation region was the penetration of monsoon rain toward the Sahel (SFC 33.6%), overcoming weaker effects of warmer pacific and equatorial Atlantic

oceans regions that have a reduction effect on the Sahel precipitation. The higher resolution 6-years simulations were consistent with the above results, generally showing enhancement of some of the effects, with lower surface temperature over the afforested area core, compared with the lower resolution simulations (a. 1.5 ℃, b. ~0 $m\,s^{-1}$) that led to further decrease in easterly low level jet intensity (a. 3 $m\,s^{-1}$, b. 2 $m\,s^{-1}$) and its displacement (a. 3^0N, b. 3^0S), and further increase in precipitation (a. 5 $mm\,d^{-2}$, b. 5 $mm\,d^{-2}$). Sensitivity tests of the different vegetation parameters (e.g., albedo, roughness, root-depth) showed that the dominant parameter was the increase in root-depth, allowing the increased net radiation to enhanced evaporation and surface cooling. Roughness also enhanced surface cooling by increasing surface-atmosphere aerodynamic conductivity.

The results of this study showed that large-scale forestation in some semi-arid regions can result in significant increase in local/regional precipitation and surface cooling, associated with changes in atmospheric dynamics. Such changes can help sustain and enhance the original changes in vegetation cover and provide useful climate change mitigation tool.

9.2. A Positive feedback from large-scale forestation

Large-scale forestation in the SAM as well as over the Sahel and N-Aust, has the potential to provide a carbon sink of ca. 2.2 tons carbon per hectare for several decades (*Rotenberg, E., and Yakir, D, 2009*) over areas of million of hectares. But, it will also affect the surface energy budget, the regional atmospheric circulation and regional hydrology. Based on our numerical simulation we suggest that these changes involve a possible positive feedback mechanism (Fig. 44): 1) Changing land cover from shrubland to forest increases the root depth. 2) This leads to increase in the ratio of ET/runoff. 3) Increases soil water content and ET results in lower surface temperature over the forest and decrease in the meridional temperature gradient. 4) Changes in temperature gradient leads to increased precipitation due to weakening and displacement of the low level thermal wind, responsible for the generation the easterly jet. 5) Increased cloudiness also play important role by lowering the shortwave downward radiation, which moderates the increase of surface net radiation due to lower forest albedo. 6) Ocean contribution to the precipitation over the Sahel showed relatively

small negative contribution of the Pacific and Atlantic oceans compared with the positive feedback of the dominant higher SST of the Northern hemisphere during summertime monsoon season in the Sahel.

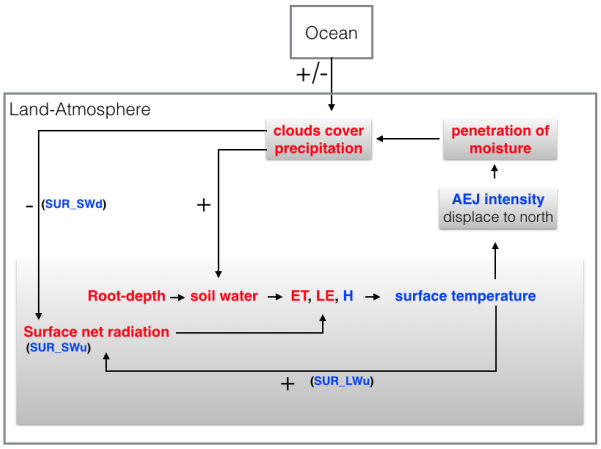

Figure 44. Schematic diagram for the mechanism driving the increased precipitation over the Sahel/N-Aust, as a consequence of land cover change from low-level vegetation to forest. Red and blue color indicates increasing and decreasing effects, respectively.

9.3. Implications for afforestation over semi-arid monsoon regions

Vegetation impacts the atmosphere by modifying major parameters, such as the partitioning of the precipitation input, the surface roughness length, the atmosphere stability (Bowen ratio), the surface albedo, surface emissivity, and the carbon fluxes. The sign and strength of vegetation feedbacks depend on the geographical region and background climatology. Future predictions of environmental changes in the semi-arid regions, according to the Climate Model Intercomparison Project (CMIP), indicate higher heat stress, which could reduce vegetation cover and further enhance the surface warming. Continued agricultural practices in China and India and grazing in North America and northern Australia are likely to reduce the total leaf area and could lead to surface heating and a dampened the hydrological cycle. Drought events can trigger vegetation loss, which through positive vegetation-precipitation feedbacks could amplify the drought intensity *(Notaro et al, 2011)*. In this context, our study propose a potential climate change mitigation approach to deal with such climate changes over SAM regions such as North Africa, North America,

South America, India and North Australia, all of which are influenced by low-level Jets (Fig. 45). Afforestation and forestation proposes is shown to have direct effects on surface temperature that can lead, indirectly, to increase the local and regional precipitation, as a result of changes in the atmospheric low level Jet steams that limit moisture penetration to these land areas. Increasing precipitation over those areas will help maintain the forest and moderate the facing climate change.

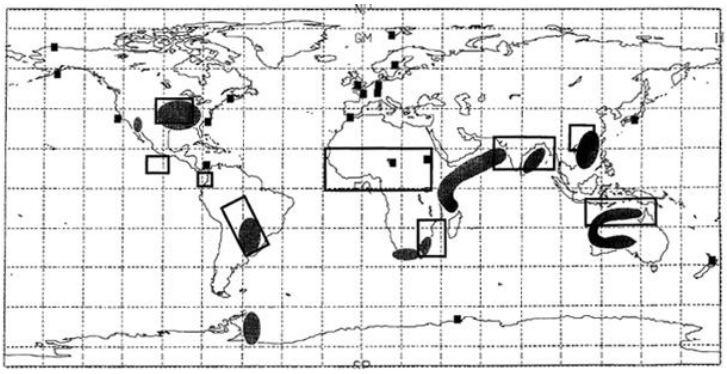

Figure 45. Regional where low-level Jets are known or suspected to occur with some regularity (shaded) and were mesoscale convective complex are known to occur frequently during the summer (open boxes). Squares denote locations where low-level jets have been observed, From Stensrud (1996).

Appendix

Appendix A: Model Evaluation

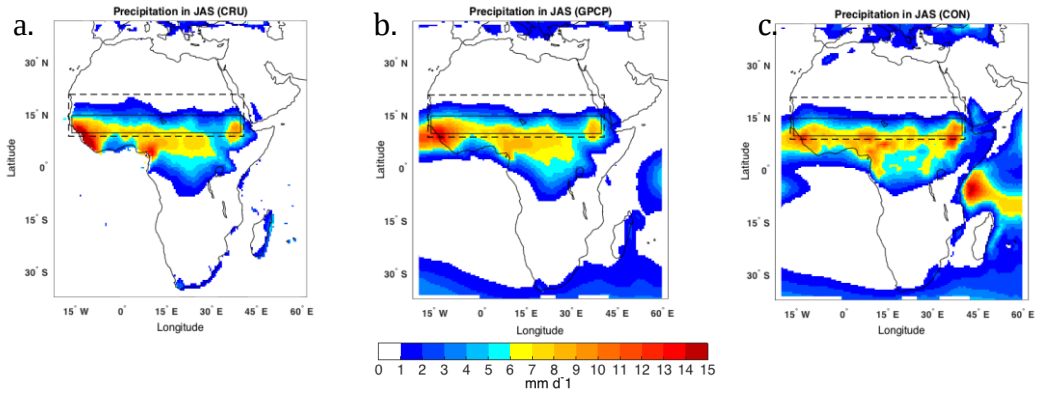

Figure A.1: Observation and model simulated of Precipitation over Africa for July-September (JAS) mean between the years 1998-2012: (a) CRU, (b) GPCP, (c) CON-2d. The Afforested area [10^0-15^0 N, 16^0 W-40^0 E] indicates as solid line and the dash lines cover the footprint area [10^0-20^0 N, 16^0 W-40^0 E].

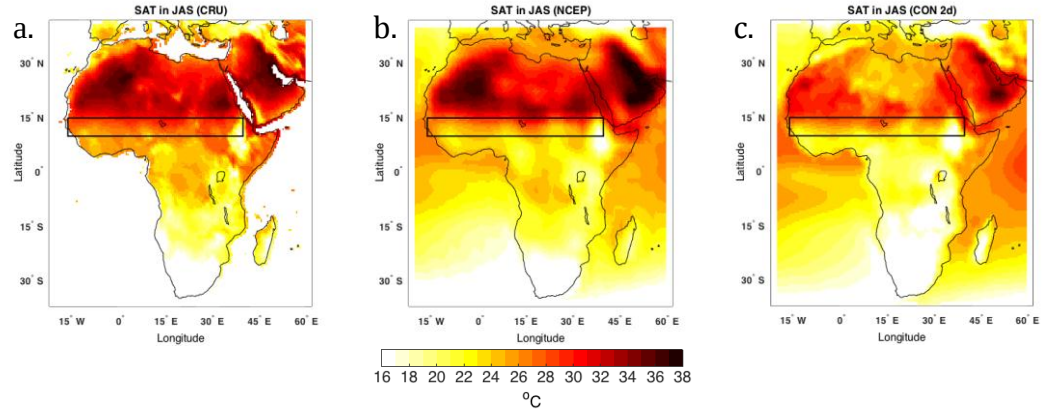

Figure A.2: Observation and model simulated of SAT over Africa for July-September (JAS) mean between the years 1998-2012: (a) CRU, (b) NCEP (c) CON-2d. The Afforested area [10^0-15^0 N, 16^0 W-40^0 E] indicates as solid line and the dash.

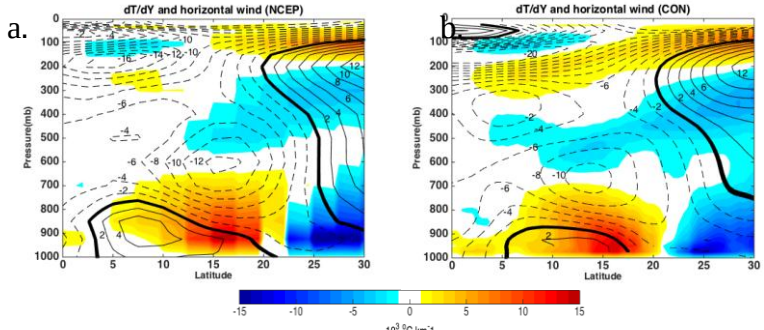

Figure A.3: Observed and model simulated seasonal mean (JAS) over Africa, of zonally (10^0W-15^0W) averaged meridional temperature gradient dT/dy (^{0}C per 1000 km) and zonal wind (m s^{-1}) for the period 1998-2012. (a) NCEP and (b) CON-2d-S

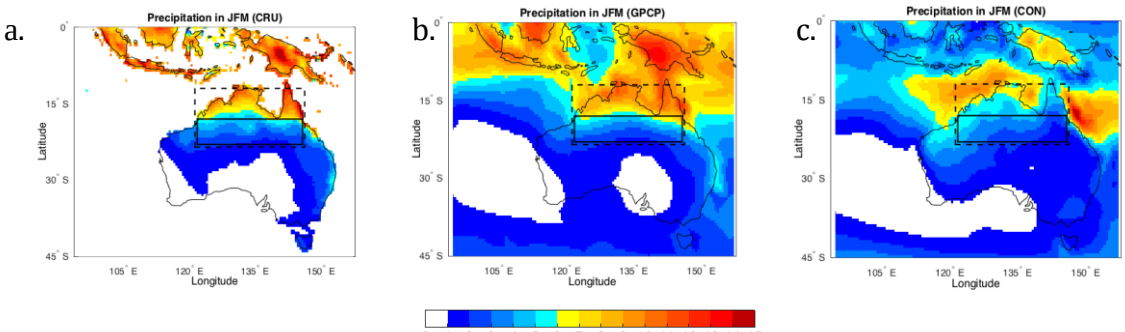

Figure A.4: Observation and ion over N-Aust for Jan-March (JFM) mean between the years 1998-2012: (a) CRU, (b) GPCP, (c) CON-2d. The Afforested area [10^0-15^0 N, 16^0 W-40^0 E] indicates as solid line and the dash lines cover the footprint area [10^0-20^0 N, 16^0 W-40^0 E].

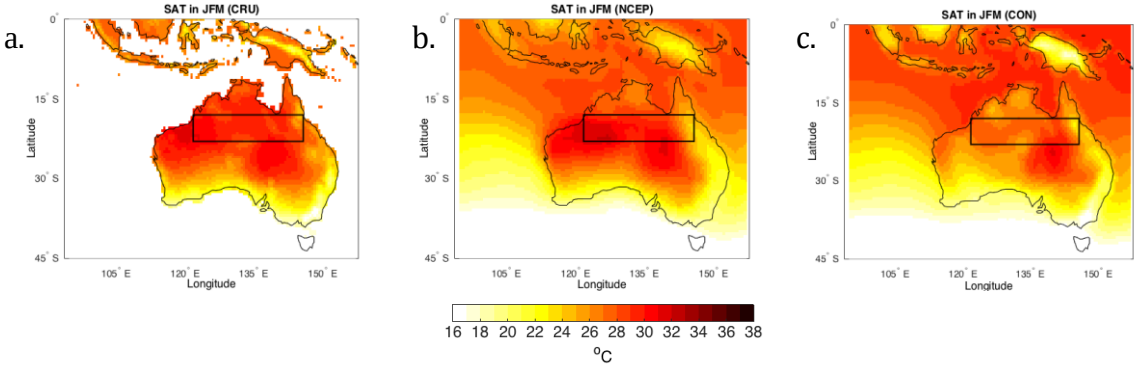

Figure A.5: Observation and model simulated of SAT over N-Aust for Jan-March (JFM) mean between the years 1998-2012: (a) CRU, (b) NCEP (c) CON-2d. The Afforested area [17^0-22^0 S, 122^0 - 146^0 E] indicates as solid line.

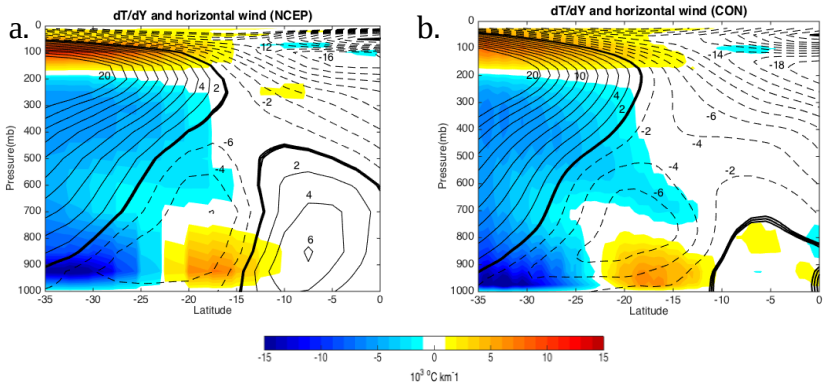

Figure A.6: Observed and model simulated seasonal mean (JFM) over Australia, of zonally (130^0-135^0E) averaged meridional temperature gradient dT/dy (^{0}C per 1000 km) and zonal wind (m s^{-1}) for the period 1998-2012. (a) NCEP and (b) CON-2d.

Appendix B: Temperature and moister atmosphere profile over the Sahel

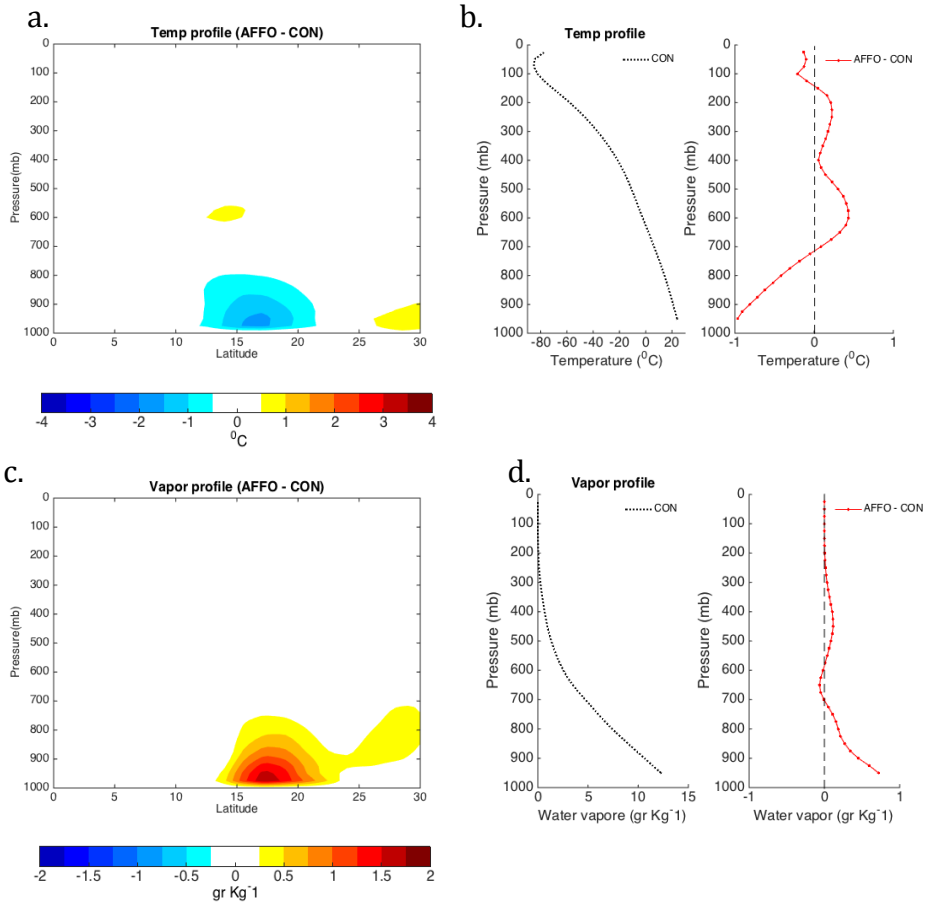

Figure B.1: Model simulated CON and bias (AFFO – CON) seasonal mean (JAS) for the period 1998 -2012, of (a) zonally (10^0W- 15^0W) averaged meridional temperature (^{0}C) and (c) water vapor specific density (Kg Kg^{-1}), (b) zonally (10^0W- 15^0W) and meridional (10^0N-20^0N) average temperature (^{0}C) and (d) water vapor specific density (Kg Kg^{-1}).

Appendix C: Sensitivity analysis, Biosphere-atmosphere feedback

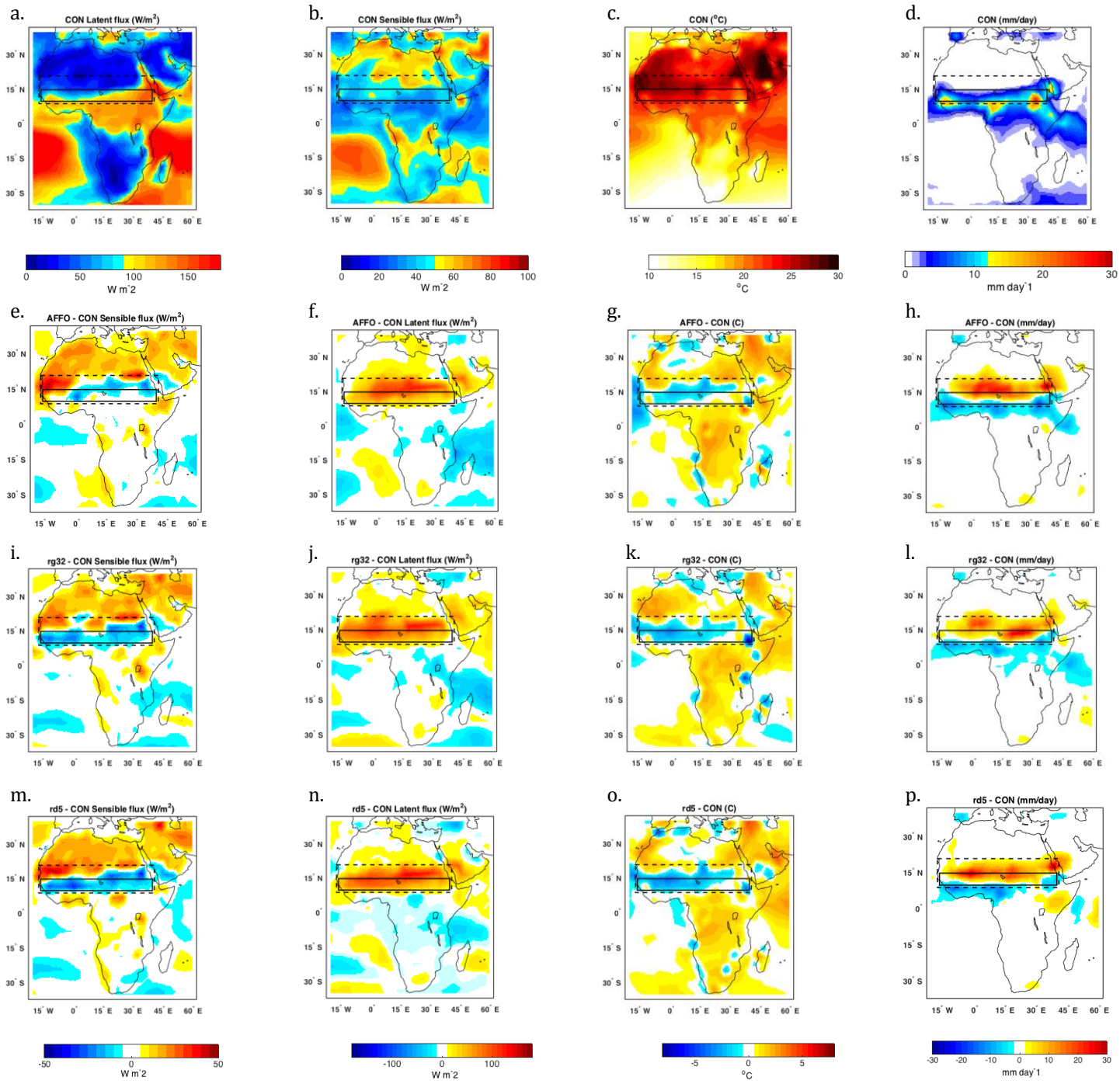

Figure. C.1 Sahel regions (black dash line rectangular) examined in table 5 for the SIM1 (CON) results of (a) sensible heat (H), (b) latent heat (LE), (c) surface temperature (^{0}C) and (d) precipitation (mm/month). The bias of SIM1 (CON) to: SIM2 (AFFO) at (e) to (h), SIM6 (h-ev) at (i) to (l), SIM8 (rd-ev) (m) to (p) Contour in unit of [W m-2], Solid lines represent the afforested area [10^0-15^0 N, 16^0 W-40^0 E], and the dash lines cover the footprint area [10^0-20^0 N, 16^0 W-40^0 E].

Appendix D: Energy budget over North Australia

Table D.1 Energy budget over N-Aust

Surface (SUR) and Top of Atmosphere (TOA) energy budget components over N-Aust [17^0-22^0 S, 122^0 -146^0 E], in JFM for the period 1998-2012, of CON-2d and AFFO-2d-NA: radiative components: Up (u) and Down (d), Short and Long wave (SW and LW), and total net radiation (Rnet), Surface non-radiative components: sensible (H) and latent (LE) heat flux, Evapotranspiration (ET) and Surface Air Temperature (SAT). Cloud forcing also calculate with subtracting the full sky from the clear sky. Spatial standard deviation (std) was calculated for the given region. Units: Energy components [W m-2], ET [mm day^{-1}] and SAT with [^{0}C].

	CON				AFFO				AFFO-CON				cloud forcing
	full sky	std	clear sky	std	full sky	std	clear sky	std	full sky	std	clear sky	std	
SUR-SWd	261.1	12.0	297.3	2.3	257.8	11.3	297.0	2.2	-3.4	2.3	-0.3	0.1	-3.0
SUR-SWu	54.4	10.0	61.0	9.9	53.2	10.0	59.6	9.9	-1.2	0.5	-1.4	0.6	0.2
SUR-LWd	355.0	12.4	346.4	10.6	354.8	12.4	345.5	10.7	-0.2	0.6	-0.9	0.4	0.7
SUR-LWu	443.2	14.5	443.1	14.5	438.3	14.5	438.2	14.5	-4.9	0.5	-4.9	0.5	0.0
SUR-Rnet	118.5	4.7	139.7	9.8	121.1	4.8	144.8	9.6	2.6	1.3	5.1	0.6	-2.5
TOA-SWd	385.0	0.0	385.0	0.0	385.0	0.0	385.0	0.0	0.0	0.0	0.0	0.0	0.0
TOA-SWu	105.1	6.7	77.3	8.7	106.8	6.5	76.1	8.7	1.7	2.0	-1.2	0.5	3.0
TOA-LWu	274.4	7.6	285.6	8.4	271.5	7.5	283.9	8.4	-2.9	0.9	-1.7	0.2	-1.1
TOA-Rnet	5.5	5.9	22.0	8.4	6.7	6.2	25.0	8.4	1.1	1.6	3.0	0.5	-1.8
H	64.0	5.2			57.9	5.1			-6.1	0.8			
LE	66.2	13.9			74.9	13.7			8.7	1.9			
ET (mm/day)	2.3	0.5			2.6	0.5			0.3	0.1			
SAT [C]	27.1	0.5			26.2	0.5			-0.9	0.1			

Reference

1. Ackermann, K. et al. 2014: Water and soil conservation practices in the Sahel: an analysis of their potential to increase resilience of rural livelihoods. *In:Pla @Risk*, 2(1), Special Issue on Desertification: 14-2-, Davos: Global Risk Forum GRF Davos.
2. Anthes, R. A. Enhancement of convective precipitation by mesoscale variations in vegetative covering in semi-arid regions, *J. Climate Appl. Meteorol*. **2**, 541-554 (1984).
3. Avissar, R. and Pielke .R. A. A parameterization on heterogeneous land surface for atmosphere numerical models and its impact on regional meteorology, *Mon. Wea. Rev*. **117**, 2113-2136 (1989).
4. Benjamin, S. G, et al. Mesoscal weather prediction with RUC hybrid isentropic-terrain-following coordinate model. *Mon. Wea. Rev*. **132**, 473-494 (2004a).
5. Banacos, C. P, and D. M. David. The Use of Moisture Flux Convergence in Forecasting Convective Initiation: Historical and Operational Perspectives. *Forecasters Forum*, 351-366 (2005).
6. Bonan, G. B. Forests and climate change; Forcing, feedbacks and the climate benefits of forests. *Science*, **320**,1444-1449 (2008).
7. Bretherton CS, SmithC, Wallace J. An intercomparison of methods for finding coupled patterns in climate data. *J. Climate*. **5**, 541-560 (1992).
8. Biasutti M, Held IM, Sobel AH, Giannini A. SST forcing and Sahel rainfall variability in simulations of the twentieth and twenty-first centuries. *J. Climate*. **21**, 3471-3486 (2008).
9. --. Forced Sahel rainfall trends in the CMIP5 archive. *J. Geophys. Res*. **118**, 1612-1623 (2013).
10. Charney, J. G. Dynamics of deserts and drought in the Sahel. *Quart. J. R. Meteorol. Soc.* **101**, 193-202 (1975).
11. Chadwick, R., et al. Large rainfall changes consistently projected over substantial areas of tropical land. *Nature*.*Cliamte* (2015). doi:10.1038/nclimate2805
12. Chou, C. Land-sea heating contrast in idealized Asian summer monsoon. *J. Clim. Dynam*. **21**, 11-25 (2003).

13. Claussen, M., V. Brovkin, et al. Biogeophysical versus biogeochemical feedbacks of large-scale land cover change. *Geophysical Research Letters*, **28**, 1011-1014 (2001).
14. Cook, K. H. Generation of the African Easterly Jet and Its Role in Determining West African Precipitation, *J. Climate*, **12**, 1165-1184 (1999).
15. Cowling. S. A., Jones C. D., and Cox P. M. Greening the terrestrial biogeoshpere: simulated feedbacks on atmospheric heat and energy circulation, *J. Climate Dynamics.* **32**, 287-299 (2009).
16. Cornforth, R. J., B. J. Hoskins, C. D. Thorncroft. Impact of moist processes on the African Easterly Jet-African Easterly Waves system. *Quart. J. R. Meteorol. Soc*.**135**, 894-913 (2009).
17. DeFries, R.S., et al. Carbon emissions from tropical deforestation and regrowth based on satellite observations for the 1980s and 1990s. *Proc. Natl. Acad. Sci. USA*, **99**, 14256-14261 (2002).
18. deMenocal, P. et al. Abrupt onset and termination of the African Humid Period: Rapid climate responses to gradual insolation forcing, *Quat. Sci. Rev*., **19**, 347-361 (2000).
19. De Ridder, K., and H. Galle. Land surface-induced regional climate change in southern Israel. *J. App. Meteor*, 37, 1470-1485 (1998).
20. Drosdowsky, W. Variability of the Australian summer monsoon at Darwin: 1957-1992. *J. Climate*, **9**, 85-96 (1996).
21. Emanuel KA, Rothman MZ. Development and evaluation of a convective scheme for use in climate models. *J. Atmos. Sci*. **56**, 1756-1782 (1999).
22. Field, C. B., D. B. Lobell, H. A. Peters, and N. R. Chiariello. 2007. Feedbacks of Terrestrial Ecosystems to Climate Change. *Annual Review of Environment and Resources,* **32**, (2007).
23. Flohn, H., Hening, D. and Korff. H. C. Possibilities and limitations of a large-scale water budget modification in the Sudan-Sahel belt of Africa. *Meteor Rundsch*. **27**, 100-109 (1974).
24. Foley, Jonathan A., Samuel Levis, Marcos Heil Costa, Wolfgang Cramer, and David Pollard. Incorporating dynamic vegetation cover within global climate models, *J. Ecological Applications,* **10**,1620–163 (2000).
25. Folland, C. K., Palmer, T. N. E. Sahel rainfall and worldwide sea temperature, 1901-85.

Nature. **320**, 620-607 (1986).

26. Freedman, J.M. et al. Boundary Layer Clouds and Vegetation– Atmosphere Feedbacks. *J. Climate*. 14, 180– 197 (2001).
27. Giannini, A, Saravanan, R, and Chang, P. Oceanic forcing of Sahel rainfall on Interannual to interdecadel time scales. *Science*, **302**,1027-1030 (2003).
28. Giannini, A. et al. A unifying view of climate change in the Sahel linking intra-seasonal, international and longer time scales. *Environ. Res. Lett*. **8**, 024010 (2013).
29. Goodin, R and Northington, K. Plant Resources of Arid and Semi-Arid Lands. A Global Perspective. *Academic Press. New York* (1985).
30. Hagos S.M, Cook K.H. Dynamics of the West African monsoon jump. *J. Climate*, **20**, 5264-5284 (2007).
31. Harris, I., et al. Updated high-resolution grids of monthly climate observations – the CRU TS3.10 Dataset. *Int. J. Climatol*. **34**, 623-642 (2014).
32. Hendon, H, Thompson, D and Wheeler, M. Australian rainfall and surface variations associated with the southern annular mode, *J. Climate*, **20**, 2452-67 (2007).
33. Houghton, R.A. Revised estimates of annual net flux of carbon to the atmosphere from changes in land use and land management 1850-200. *Tellus*, 55B(2), 378-390 (2003).
34. Hung, C.-W. and M. Yanai. Factors contributing to the onset of the Australian summer monsoon. *Quart. J. R. Meteorol. Soc.* **130**, 739-758 (2004).
35. Hsieh J. S. and Cook K. H. Generation of African easterly wave disturbances: relationship to the African easterly jet, *Monthly Weather Review*. **133**, 1311-1327 (2005).
36. Huffman, G.J. and Bolvin. D.T. TRMM and Other Dat Precipitation Data Set Documentation. NASA/GSFC (2014). ftp://precip.gsfc.nasa.gov/pub/trmmdocs/3B42_3B43_doc.pdf , 42 pp. - See more at: https://climatedataguide.ucar.edu/climate-data/trmm-tropical-rainfall-measuring-mission#sthash.GD2rBJ2e.dpuf
37. IPCC Summary for Policymakers in Climate Change 2014: Impacts, Adaptation, and Vulnerability (eds Field, C. B et al.) (Cambridge Univ. Press, 2014).
38. Jackson, R. B. et al. A global analysis of root distributions for terrestrial biomes. *Oecologia*, 108, 389-411 (1996).

39. Janicot S, Trzaska S, Poccard I. Summer Sahel-ENSO teleconnection and decadal time scale SST variation. *J. Clim. Dynam*. **18**, 303-320 (2001).
40. Joly M, Voldoire A. Influence of ENSO on the West African monsoon: temporal aspects and atmospheric process. *J. Climate*. **22**, 3193-3210 (2009).
41. Joly M, et al. African monsoon teleconnection with tropical SSTs: validation and evolution in a set of IPCC4 simulations. *J. Clim. Dynam*. **29**, 1-20 (2007).
42. Kanamitsu, M. et al. NCEP-DOE AMIP-II Reanalysis (R-2). *Bull. Am. Meteorol. Soc.* **83**. 1631-1643 (2002).
43. Kalnay, E. et al. The NCEP.NCAR 40-year Reanalysis Project. *Bull. Amer. Meteor. Soc.* **77**, 437-471 (1996).
44. Koppen-Geiger. Climate-zones, Central for International Development at Harvard University (1999).
45. Koster, R. D., et al. Regions of strong coupling between soil moisture and precipitation. *Science*, **305**, 1138-1140 (2004).
46. Koster, R.D., et al. GLACE: The Global Land-Atmosphere Coupling Experiment. 1. Overview. J. Hydrometeorol., 7, 590-610 (2006).
47. Land Processes Distributed Active Archive Center (LP DAAC), 2003, - Land Cover Type Yearly L3 Global 0.05Deg CMG MCD12C1, USGS Earth Resources Observation and Science (EROS) Center, Sioux Falls, South Dakota (https://lpdaac.usgs.gov), accessed January 1, 2012.
48. Land Processes Distributed Active Archive Center (LP DAAC), 2003, - NDVI NDVI.FM.c004.v2.0.WS.2003, USGS Earth Resources Observation and Science (EROS) Center, Sioux Falls, South Dakota (https://lpdaac.usgs.gov), accessed January 1, 2012.
49. Lebel .T, Diedhiou, and Laurent, H. Seasonal cycle and interannual variability of the Sahelian rainfall at hydrological scales, *J. Geophysical Research*, **108**, 11-14 (2003).
50. Lee, T. J. The impact of vegetation on the atmospheric boundary layer and convective storms. Atmospheric Science Paper No. 509, Colorado State University, Fort Collins, CO, 137 pp (1992). [Available from Dept. of Atmospheric Science, Colorado State University, Fort Collins, CO 80523.]

51. Li, W., and R. Fu. Transpiration of the large-scale atmospheric and land surface from the dry to wet season over Amazonia as diagnosed by the ECMWF re-analysis. J. Climate, **17**, 2637-2651 (2004).
52. Li, C. F. and Yanai, M. The onset and interannual variability of the Asian summer monsoon in relation to land sea thermal contrast. *J. Climate*. **9**, 358-375 (1996).
53. Lu, J, and Delworth, R. Oceanic forcing of the late 20th century Sahel drought. *Geophysical Research Letter*. **32**, L22706 (2005).
54. Martin, E.R., Thorncroft, C. and Booth, B. B. B. The Multidecadal Atlantic SST-Shale rainfall teleconnection in CMIP5 simulation. *J. Clim*. **27**, 784-806 (2014).
55. McBride, J and Nicholls, N. Seasonal relationship between Australian rainfall and Southern Oscillation. *Mon. Wea. Rev,* **111**, 1998-2004 (1983).
56. -- and W. M. Frank. Relationships between stability and monsoon convection. *J. Atmos. Sci.* **56**, 24-36 (1999).
57. McGregor JL, et al. Fine resolution simulations of climate change for Southeast Asia. Final report for a Research Project commissioned by Southeast Asian Regional Committee for START (SARCS), Aspendale, Vic., CSIRO Atmospheric Research VI, pp 15-35.
58. Medvigy, D., Walko, R. L., and Avissar. R. Modeling Interannual Variability of the Amazon Hydroclimate. *Geophys. Res. Let.* **35**, L15817 (2008).
59. Medvigy, D., Walko, R. L., M.J. Otte and Avissar. R.The Ocaen-Land-Atmosphere Model (OLAM): Optimization and Evaluation of Simulated Radiative Fluxes and Precipitation. *Mon. Wea. Rev*., **138**, 1923-1939 (2010).
60. Medvigy, D., Walko, R. L., and Avissar. R. Effects of Deforestation on Spatiotemporal Distributions of Precipitation in South America. *J. Climate*. **24**, 2147-2163 (2011).
61. Miller G. H, et al. Sensitivity of Australian Monsoon to insolation and vegetation: Implications for human impact on continental moisture balance. *Geology*, **33**, 65-68 (2005).
62. Mohino EB, et al. Sahelian rainfall and decadal to multidecadal SST variability. *J. Clim. Dynam*. **37**, 419-440 (2011).
63. Narisma G. T and A. J. Pitman. The Impact of 200 Years of Land Cover Change on the Australian Near-Surface. *Climate. J. Hydrometeorology*, **4**, 424-436 (2003).

64. Neelin, J. D., and I. M. Held. Modeling tropical convergence based on the moist static energy budget. *Mon. Wea. Rev*. **115**, 3–12 (1987).
65. Nicholls, N., J.L. McBride, and R.J. Ormerod. On predicting the onset of the Australian wet season at Darwin. *Mon. Wea. Rev*, **110**, 14-17 (1982).
66. Nicholson, S.E. Land surface process and Sahel climate. *Reviews of Geophysics*. **38**, 117-139 (2000).
67. -- and Grist, J. P. A. Conceptual model for understanding rainfall variability in the West African Sahel on interannual and interdecadel timescales, *International Journal of Climatology*. 21, 1733-1757 (2001).
68. --. A revised picture of the structure of the "monsoon" and land ITCZ over West Africa. *J. Clim. Dynam*, **32**, 115-1171 (2009).
69. --. The West African Sahel: A Review of Recent Studies on the Rainfall Regime and Its Interannual Variability. *ISRN Meteorology*, 2013, 32 (2013).
70. Notaro M., Chen, G. & Liu, Z. Vegetation Feedbacks to Climate in the Global Monsoon Regions. *J. Climate*. **24**, 5740-5753 (2011).
71. Ornstein, L., Aleinov, I. and Rind, D. Irrigated afforestation of Sahara and Australian Outback to end global warming, *J. Climate Change*. **97**, 409-437 (2009).
72. Otterman, J., et al. An increase of early rains in Southern Israel following land-use change, *Bound-Layer Meteor* ., **53**, 333-351 (1990).
73. Palmen, E., and E. O. Holopainen. Divergence, vertical velocity and conversion between potential and kinetic energy in an extratropical disturbance. *J. Geophysical*, **8**, 89-113 (1962).
74. Pal JS, et al. The ITCP RegCM3 and RegCNET: regional climate modeling for the developing world. *Bull. Am. Meteorol. Soc*, **88**, 1395-1409 (2007).
75. Patricola, C. M. & Cook, K. H. Dynamics of West African Monsoon under Mid-Holocene precessional forcing: regional climate model simulation. *J. Climate*. **20**, 649-716 (2007).
76. Peixoto, J. P. and Oort, A. H. The atmospheric branch of the hydrological cycle and climate. *Variations in the Global Water Budget*, 5-56 (1983).
77. Pielke, R A., et al. Copeland. A comprehensive meteorological modeling system RAMS. *Meteorol. Atmos. Phys*., **49**, 69-91 (1992).

78. Philippon, N., and B. Fontaine. The relationship between the Sahelian and previous 2nd Guinean rainy seasons: A monsoon regulation by soil wetness?, *Ann. Geophys.*, **20**(4), 575–582 (2002).
79. Roberts, R.G, et al. The human colonization of Australia: Optical dates of 53,000 and 60,000 years brackets human arrival at Deaf Adder Gorge, Northern Territory. *Quaternary Geochronology*, **13**, 575-583 (1994).
80. Rodriguez-Forseca, B, and Manuel de Castro. On the connection between winter anomalous precipitation in the Iberian Peninsula and North West Africa and summer subtropical Atlantic sea surface temperature. *Geophys. Res. Lett.* **29(18),** 1863, (2002).
81. Rodriguez-Forseca, B, et al. Interannual and decadal SST-forced responses of the West African monsoon. *Quart. J. R. Meteorol. Soc.* **12**, 67-74 (2011).
82. Rotenberg, E., and Yakir, D. Contribution of Semi-Arid Forests to the Climate System, *Science*, **327**, 451 (2009).
83. Salih, M.A. and Ahamed, A.G. The Impact of Indigenous Knowledge and Traditional Coping Strategies on Desertification process. A research report presented to the IDRC, Nairobi, Kenya (1993).
84. Schar, C., et al. The soil-precipitation feedback: A process study with a regional climate model. *J. Climate*, **12**, 722-741 (1999).
85. Sellers, P. J. Biophysical models of land surface processes. *Climate System Modeling*. K.E. Trenberth, ED., Cambridge University Press, 451-490 (1992).
86. Stebbing, E.P. The man-made desert in Africa. *J. Roy. African Soc* ., **37 (**1938).
87. Segal, M., Arritt R. W., Clark, C., Rabin, R. & Brown. J. M. Scaling evaluation of the effect of surface characteristics on potential for deep convection over uniform terrain, *Mon. Wea. Rev* . **123**, 383-400 (1995).
88. Stensrud, D. J. Importance of low-level jets to climate: A review. *J. Climate*, **9**, 1698-1711 (1996).
89. Steiner AL, et al. Land surface coupling in regional climate simulations of the West African monsoon. *J. Clim. Dynam*, **33**, 869-892 (2009).
90. Sylla MB, et al. High-resolution simulations of West Africa climate using Regional Climate Model (RegCM3) with different lateral boundary conditions. *Theory Appl Climatol*. **98**, 293-314 (2009).

91. Sylla MB, et al. Multiyear simulation of the African climate using a regional climate model (RegCM3) with the high resolution ERA-interim reanalysis. *J. Clim. Dynam*. 35, 231-247 (2010).
92. Thorncroft CD, Blackburn M. Maintenance of the African easterly jet. *Quart. J. R. Meteorol. Soc.* **125**, 763-786 (1999)
93. ---, et al. Annual cycle of the West African monsoon: regional circulations and associated water vapour transport, *Quart. J. R. Meteorol. Soc.* **137**, 129-147 (2011).
94. ---, et al. The JET2000 Project: aircraft observations of the African Easterly Jet and African Easterly Waves. *Bull Am Meteorol Soc*. **84**(3), 337-351 (2003).
95. Trenberth, K. E. Atmospheric moisture recycling: Role of advection and local evaporation. *J. Climate,* **12**, 1368-1381 (1999).
96. Turner, A. G. and Annamalai, H. Climate change and the South Asian summer monsoon. *Nature Climate Change*, 2. 587-595 (2012).
97. Wheeler, M. C. and H. Hendon. An all-season real-time multivariate MJO index: Development of an index for monitoring and predilection. *Mon. Wea. Rev.* **132**, 1917-1932 (2004).
98. Wang, G. Eltahir EAB. Ecosystem dynamics and the Sahel drought. *Geophysical Research Letter*. **27**, 6, 795-798 (2000).
99. Wallace JM, Smith C, Bretherton CS. Singular Value Decomposition of wintertime Sea Surface Temperature and 500-mb height anomalies. *J. Climate*. **5**, 561-576 (1992).
100. Walko, R. L, and Avissar. R. The Ocean-Land-Atmosphere Model (OLAM). Part 1: Shallow-water tests. *Mon. Wea. Rev*. **136**, 4033-4044 (2008)
101. Walko, R. L, and Avissar. R. The Ocean-Land-Atmosphere Model (OLAM). Part 2: Formulation and tests of the nonhydrostatic dynamic core. *Mon. Wea. Rev.* **136**, 4045-4062 (2008).
102. --. The Ocean-Land-Atmosphere Model (OLAM). Part 2: Formulation and tests of the nonhydrostatic dynamic core. *Mon. Wea. Rev.* **136**, 4045-4062 (2008).
103. -- et al. Coupled atmosphere-biophysics-hydrology models for environmental modeling. *J. App. Meteor*. **39**, 931-944 (2000).
104. Wu, M.-L., et al. African easterly jet, structure and maintenance. *J. Climate*. **22**, 4459-4480 (2009).

105. Xue, Y and Shukla, J. The influence of land surface properties on Sahel climate. Part 1: Deforestation. *J. Climate*. **6**, 2232-2245 (1994).

106. --. and Shukla, J. The influence of land surface properties on Sahel climate. Part 2: Afforestation. *J. Climate*. **9**, 3260-3274 (1996).

107. Zeng, N., et al. Enhancement of Interdecadel Climate Variability in the Sahel by Vegetation Interaction. *Science*. **286**, pp. 1537-1540 (1999).

108. --, and Neelin. J. D. The role of vegetation-climate interaction and interannual variability in shaping the African savanna. *J. Climate*, **13**, 2665-2670 (2000).

109. --, et al. Drought in the Sahel. *Science*. **302**, 999-1000 (2003).

110. Zhang, C., Nolan D. S., Thorncroft, C. D, and Nguyen, H. Sahel low meridional circulations in the tropical atmosphere, *J. Climate*, **21**, 3453-3470 (2008).

111. Zhao, M., and A. J. Pitman. The impact of land cover change and increasing carbon dioxide on the extreme and frequency of maximum temperature and convective precipitation. *Geophys. Res. Lett*., 29, 1078 (2002).